Measuring glutamate transients at Schaffer collateral synapses

Dissertation

with the aim of achieving a doctoral degree (Dr. rer. nat.) at the Faculty of Mathematics, Informatics and Natural Sciences of the University of Hamburg

Center for Molecular Neurobiology, Institute for Synaptic Physiology

Submitted by

Céline Dürst

Lausanne

July 2018, Hamburg

The following evaluators recommend the admission of the dissertation:

Supervisor
Prof. Dr. Thomas G. Oertner
Institut für Synaptische Physiologie
Zentrum für Molekulare Neurobiologie (ZMNH)
am Universitätsklinikum Hamburg-Eppendorf
Co-Supervisor
Prof. Dr. Christian Lohr
Abteilung Neurophysiologie
Zoologisches Institut an der Universität Hamburg

Oral defense: December 7th, 2018

Table of Contents

Table of Figures

Summary

In the mammalian cortex, glutamatergic excitatory synapses convert presynaptic action potentials into chemical signals that are sensed by postsynaptic glutamate receptors. The smallest unit or 'quantum' of information transmission at chemical synapses is the release of a single transmitter-filled vesicle. Typical presynaptic terminals contain only a small number of docked vesicles. It is therefore difficult to determine how many vesicles are released in response to a single action potential and whether they all contain the same amount of glutamate. Here, I introduce a new strategy to investigate presynaptic release, using the genetically encoded glutamate sensor iGluSnFR to measure glutamate release in the synaptic cleft directly and independently of postsynaptic receptors. I expressed the genetically encoded glutamate sensor iGluSnFR in CA3 pyramidal cells and performed two-photon glutamate imaging on individual Schaffer collateral boutons in CA1. I showed that this probe is sufficiently sensitive to detect fusion of single vesicles at Schaffer collateral boutons in organotypic hippocampal cultures and that I can localize the fusion site on the bouton with high precision. Statistical analysis of response amplitude distributions allowed me to extract the synaptic parameters n, p_{ves}, and q. At some boutons, the amplitude distribution of glutamate transients showed distinct quantal peaks, suggesting a very constant number of glutamate molecules per vesicle. During multivesicular release, glutamate concentrations in the synaptic cleft reached very high values, leading to partial saturation of iGluSnFR responses. I showed that the saturation curves of iGluSnFR and endogenous AMPA receptors are very similar, making iGluSnFR an excellent tool to study the release machinery at individual synapses in intact tissue. Under near physiological conditions, Schaffer collateral synapses typically released only a single vesicle (univesicular events). However, almost all synapses increased their release probability and shifted to multivesicular release in high extracellular Ca^{2+} concentrations. Using dual patch-clamp

recordings and Monte Carlo simulations of glutamate diffusion, I showed that the dynamic range of iGluSnFR responses is similar to postsynaptic AMPA receptor currents while the kinetics of the underlying glutamate transients is an order of magnitude faster.

The genetically encoded glutamate sensor iGluSnFR enables visualization of glutamate release from presynaptic terminals at frequencies up to ~10 Hz. However, to resolve glutamate dynamics during high-frequency bursts, faster indicators are required. Here I report the development of fast ($iGlu_f$) and ultrafast ($iGlu_u$) variants with comparable brightness, but lower affinities for glutamate. Compared to iGluSnFR, $iGlu_u$ has 5-fold faster kinetics in synapses. I found that $iGlu_u$ is sufficiently fast to resolve individual glutamate release events, revealing that glutamate is rapidly cleared from the synaptic cleft. Depression of $iGlu_u$ responses during 100 Hz trains correlates with depression of postsynaptic EPSPs, indicating that depression during high-frequency stimulation is purely presynaptic in origin. Furthermore, I found that at individual boutons, the recovery from depression could be predicted from the amount of glutamate released on the second pulse (paired-pulse facilitation/depression), demonstrating differential frequency-dependent filtering of spike trains at Schaffer collateral boutons.

Zusammenfassung

Exzitatorische Synapsen wandeln präsynaptische Aktionspotentiale in chemische Signale um, die von postsynaptischen Glutamat-Rezeptoren wahrgenommen werden. Die kleinste Einheit oder "Quantum" der Informationsübertragung an chemischen Synapsen ist die Freisetzung eines einzelnen Transmitter-gefüllten Vesikels. Im Kortex der Säugetiere enthalten typische präsynaptische Boutons nur eine kleine Anzahl angedockter Vesikel. Es ist schwierig zu bestimmen, wie viele Vesikel als Reaktion auf ein einzelnes Aktionspotential freigesetzt werden und ob sie alle die gleiche Menge an Glutamat enthalten. In dieser Arbeit stelle ich eine neue Methode zur Untersuchung der präsynaptischen Funktion vor, die den genetisch kodierten Glutamat-Sensor iGluSnFR verwendet, um Glutamat im synaptischen Spalt unabhängig von postsynaptischen Rezeptoren zu messen. Der genetisch kodierte Glutamat-Sensor iGluSnFR wird in CA3 Pyramidalzellen exprimiert und Zwei-Photonen-Glutamat-Bildgebung an einzelnen Schaffer-Kollateral-Boutons in CA1 durchgeführt. Ich zeige, dass der Sensor empfindlich genug ist, um die Fusion einzelner Vesikel an Schaffer-Kollateral-Boutons in organotypischen hippokampalen Schnittkulturen zu detektieren und dass ich die Fusionsstelle auf dem Bouton mit hoher Präzision lokalisieren kann. Die statistische Analyse der Antwortamplitudenverteilungen erlaubte mich, die synaptischen Parameter *n*, *p* und *q* zu extrahieren. Bei einigen Boutons zeigte die Amplitudenverteilung von Glutamat-Transienten quantale *Peaks*, was auf eine sehr gleichmäßige Anzahl von Glutamat-Molekülen pro Vesikel schließen lässt. Während der multivesikulären Freisetzung erreichten die Glutamatkonzentrationen im synaptischen Spalt sehr hohe Werte, was zu einer teilweisen Sättigung der iGluSnFR-Antworten führte. Ich zeige, dass die Sättigungskurven von iGluSnFR und endogenen AMPA-Rezeptoren sehr ähnlich sind, was iGluSnFR zu einem exzellenten Werkzeug macht, um die Freisetzungsmaschinerie an einzelnen Synapsen in intaktem Gewebe zu untersuchen. Unter nahezu physiologischen

Bedingungen haben Schaffer Kollateral Synapsen in der Regel nur einen einzigen Vesikel (univesikuläre Ereignisse) freigesetzt. Jedoch erhöhten fast alle Synapsen ihre Freisetzungswahrscheinlichkeit und verlagerten sich auf eine multivesikuläre Freisetzung bei hohen extrazellulären Ca^{2+} Konzentrationen. Anhand von dualen Patch-Clamp-Aufnahmen und Monte-Carlo-Simulationen der Glutamat Diffusion zeige ich, dass der dynamische Bereich der iGluSnFR-Reaktionen den postsynaptischen AMPA-Rezeptor-Strömen ähnelt, während die Kinetik der zugrunde liegenden Glutamat-Transienten um eine Größenordnung schneller ist. Der genetisch kodierte Glutamat-Sensor iGluSnFR ermöglicht die Visualisierung der Glutamatfreisetzung aus präsynaptischen Terminals bei Frequenzen bis zu ~ 10 Hz. Um jedoch die Glutamatdynamik während eines Hochfrequenzbursts aufzulösen, sind schnellere Indikatoren erforderlich. Aus diesem Grund, wurden die schnellere Variante ($iGlu_f$) und die ultraschnelle Variante ($iGlu_u$), mit vergleichbarer Helligkeit, aber geringere Affinität für Glutamat entwickelt. Im Vergleich zu iGluSnFR hat $iGlu_u$ eine 5-fach schnellere Kinetik in Synapsen. Ich fand heraus, dass $iGlu_u$ ausreichend schnell ist, um einzelne Glutamat-Freisetzungsereignisse aufzulösen, was zeigt, dass Glutamat schnell aus dem synaptischen Spalt entfernt wird. Die Depression von $iGlu_u$-Reaktionen während 100 Hz-Zügen korreliert mit einer Depression von postsynaptischen EPSPs, was darauf hinweist, dass eine Depression während einer Hochfrequenzstimulation rein präsynaptischen Ursprungs ist. Außerdem kann ich an einzelnen Boutons feststellen, dass die Erholung von der Depression anhand der Menge an freigesetztem Glutamat im zweiten Puls vorhergesagt werden kann (gepaarte Pulserleichterung /-depression), was eine differenzielle frequenzabhängige Filterung von *Spike-Trains* an Schaffer-Kollateralboutons zeigt.

1 Introduction

1.1 Connections of the trisynaptic excitatory hippocampal circuitry

The model used for the studies presented in this thesis is a well-characterized connection, the Schaffer collateral synapse, part of the unidirectional trisynaptic excitatory hippocampal circuitry. The hippocampus is known to be essential for learning and declarative memory, a type of memory including facts and events that can be consciously remembered (Andersen et al., 2006). Furthermore, the hippocampus, more specifically the dentate gyrus, is one of the few brain regions where adult neurogenesis takes place (van Praag et al., 2002).

In this trisynaptic excitatory circuit, the entorhinal cortex layer II (EC) sends perforant pathway fibers (PP) to the dentate gyrus (DG). The PP fibers make synapses onto the spines of the granule cells (GC). The output of the dentate gyrus is formed by the axonal terminals of the GC, the mossy fibers, which form synapses in a narrow band called *stratum lucidum* onto the CA3 pyramidal cells. The latter in turn, send axons to the *Cornu Ammoni* layer 1 (CA1) via the Schaffer collaterals in a region called *stratum radiatum* which forms the third synapse of this circuit. The CA1 pyramidal cells form projections outside of the hippocampus to the layer V and VI of the EC. There are also other players, cells (different types of interneurons) and connections (like EC to CA3 as has been discovered later) in the hippocampal formation which make the wiring much more complicated than this simplified view of the unidirectional circuit (Andersen et al., 2006).

1.2 Discovery of synaptic transmission

Bernard Katz and colleagues discovered the fundamental physiological mechanism of transmitter release in the 1950's, published in two groundbreaking papers (Fatt and Katz, 1951; Del Castillo and Katz, 1954). Based on analysis of intracellular microelectrode recordings made from frog neuromuscular junctions (NMJ) at rest or under stimulation, they recorded postsynaptic currents in the muscle in response to the release of acetylcholine, termed end-plate potentials (EPPs). They showed that neurotransmitters (NTs) are released in multi-molecular packets termed 'quanta'. The size of those quanta seemed to be unaffected by any modification of external medium neither by the rapidly changing membrane property. By statistical analysis, they observed that those quanta appear very uniform and therefore proposed that they must be stored in discrete multimolecular packets. Fatt and Katz in 1952, named those events 'miniature end-plate potentials' (mEPPs). They occur spontaneously in the absence of action potentials. Along with this discovery, they also established many properties of spontaneous synaptic transmission. For example, they showed that the frequency of the mEPPs is very sensitive to osmotic concentration. This property is nowadays still widely used for chemical induction of transmitter release with the use of a hypertonic solution. Del Castillo and Katz made an even more important discovery in 1954 (Del Castillo and Katz, 1954) when they showed that the EPPs measured in response to muscle fiber stimulation in a solution containing a very low calcium concentration lead to small EPP amplitudes and trial to trial fluctuations. They observed that each EPP was an integral multiple of the mEPP amplitude: this was the beginning of the quantal release hypothesis. Katz and colleagues showed that the distribution of the EPP follows Poisson statistics with the different maxima of the multipeak histogram occurring at multiples of the mean amplitude of the mEPPs (Fig 1). The number of those simultaneously released quanta depends on the calcium concentration that ultimately determines the probability that such a

quantum will be released. Synaptic vesicles being the morphological correlate to quanta were discovered around the same time from electron micrographs of synapses from frog and earthworm (Fatt and Katz, 1951) and later from rat tissue (De Robertis and Bennett, 1955).

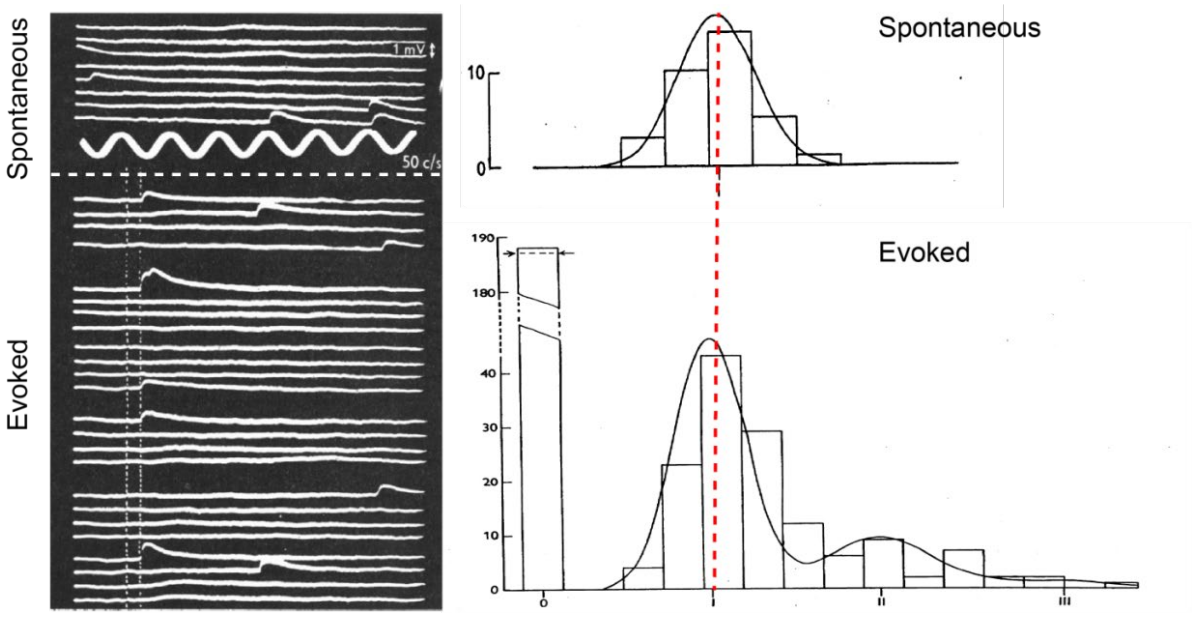

Figure 1: The quantal nature of synaptic transmission

Amplitudes of evoked responses are multiple integers of the amplitude of the spontaneous events. Intracellular recordings of spontaneous and evoked responses at the frog NMJ in very low external Ca^{2+} concentration (0.9 mM) and their corresponding amplitude distribution counts. Figure adapted from (Del Castillo and Katz, 1954).

1.3 Information transmission

Neuronal transmission takes place in a highly specialized structure termed the synapse. There is abundant evidence that synaptic transmission and plasticity have a crucial role in learning and memory. Neurons transmit the information they receive through two primary mechanisms: by the release of NTs - chemical neurotransmission - as discovered by Bernard Katz and colleagues or by direct electrical coupling - electrical neurotransmission - via gap junctions to the postsynaptic cell. In vertebrates, neuronal output mostly occurs via the

chemical transmission. The so-called ‘’classical’’ NTs are amino acid transmitters like glutamate, γ-aminobutyric acid (GABA), and glycine, catecholamines like acetylcholine, and purinergic transmitters like adenosine and adenosine-triphosphate (ATP). Long range diffusing NTs with slow signaling dynamics are the monoaminergic molecules like dopamine, noradrenaline, adrenaline, histamine and serotonin. Furthermore, neuropeptides, which are small amino acids, made of 3 to 26 residues also diffuse over even longer distances than monoaminergic NTs and contribute to neuronal modulation. Even though not considered as a primary source for synaptic transmission, membrane permeable mediators, such as nitric oxide or endocannabinoids diffuse over very long distances and permit a bidirectional information transmission from the presynapse to the postsynapse and vice versa. The classical NTs are packed into vesicles located in highly specialized structures, the presynaptic terminals. These vesicles are rapidly released through a process known as exocytosis. Once a synaptic vesicle released its content into the synaptic cleft, a space of 20 to 40 nm separating the presynaptic side from the postsynaptic side, NTs diffuse and quickly bind to receptors located on the postsynapse. Those receptors can be either ionotropic (mediate fast synaptic transmission) or metabotropic (mediate slow synaptic transmission). Ionotropic receptors are ion-permeable pores that open upon binding of their ligand causing a depolarization or a hyperpolarization in the membrane potential depending on the ion selectivity and the direction of ion flux of the receptor. The resulting deflections in the potential of the membrane are excitatory or inhibitory postsynaptic potential (EPSP or IPSP). On the other hand, the binding of a ligand to a metabotropic receptor such as G-protein coupled receptors (GPCRs), triggers a biochemical signaling cascade with multiple downstream effectors.

In this study, I focus exclusively on the amino acid transmitter glutamate which is the primary excitatory NT in the mammalian neocortex. It binds to three ionotropic receptors, AMPA, NMDA and kainate receptors and to metabotropic glutamate receptors (mGluRs).

1.4 The CNS presynaptic terminal

A typical chemical CNS synapse is made of a presynaptic terminal and postsynaptic compartment and the synaptic cleft separating them (De Robertis and Bennett, 1955). Upon propagation of an action potential, the presynaptic terminal depolarizes because of sodium channels opening and this, in turn, leads to the opening of voltage-gated Ca^{2+} channels (VGCCs). Driven by an electrochemical gradient, Ca^{2+} ions flow into the presynaptic terminal via VGCCs. Through a complex and highly regulated molecular machinery, synaptic vesicles (SVs) fuse at the active zone (AZ) of the presynaptic terminal and release their NTs in the synaptic cleft. The different players of the molecular machinery at the active zone regulating vesicle exocytosis have been extensively studied and a clearer picture has emerged (Südhof, 2004; Rizo and Xu, 2015). The released NTs diffuse and bind to postsynaptic receptors and then get actively taken up by excitatory amino acid transporters (EAATs) expressed on neurons and astrocytes. Due to these multiple steps, a delay of ~1ms exists for the information to be transferred from the pre- to the postsynapse (Figure 2). Here, the term active zone is used to describe the part of the synapse where the molecular machinery mediating fusion at the membrane is assembled. One active zone may contain several release sites for exocytosis of synaptic vesicles.

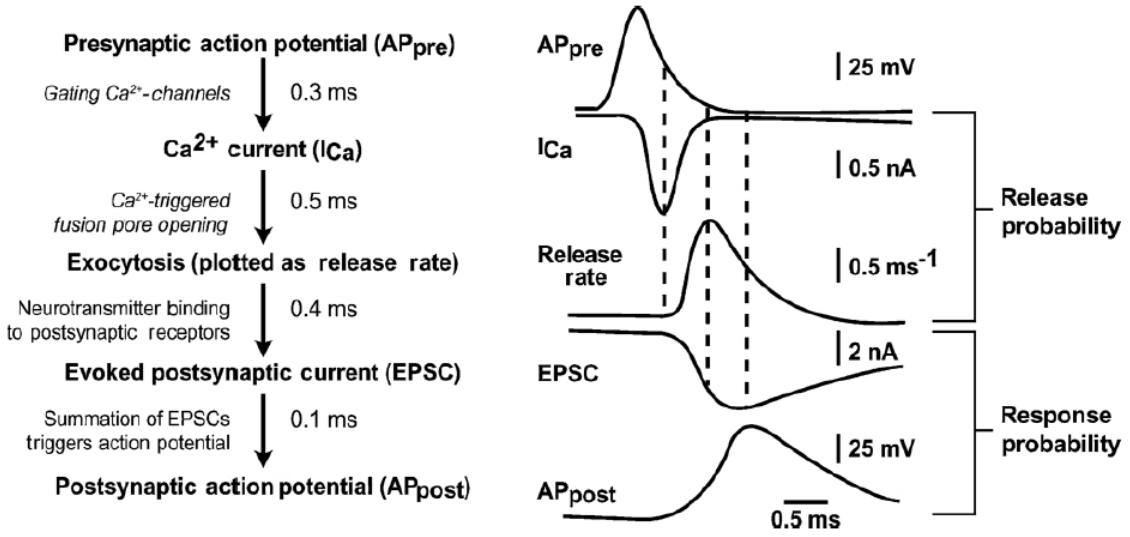

Figure 2: synaptic delay of information transmission

Multiple steps and synaptic delay occurring from the generation of a presynaptic action potential to the postsynaptic response. Figure from Südhof, 2004.

1.4.1 Synaptic vesicle exocytosis and fusion mode

Numerous steps and proteins are involved in the complex mechanisms of vesicle exocytosis. First, SVs are recruited and docked to release sites located on the AZ where they undergo exocytosis in a Ca^{2+} dependent manner. RIM, RIM-binding proteins and Munc13 recruit SVs to the release sites (Figure 3b). RIM also recruits N- and P/Q-type Ca^{2+} channels to the AZ and is, therefore, a major organizer of the AZ by coupling SVs to VGCCs. Docking of the vesicles allows them to be ready for release upon Ca^{2+} influx. Soluble *N*-ethylmaleimide-sensitive factor (NSF) attachment receptor proteins (SNAREs) and Sec1/Munc18-like proteins (SM proteins) form the main component of the molecular machinery mediating exocytosis at the AZ (Figure 3a) (Südhof, 2013). Upon depolarization, VGCCs open and Ca^{2+} flows in and binds to synaptotagmin, which stimulates its binding to a core fusion SNARE and SM proteins (Figure 3c). For the synaptic vesicle (SV) to fuse with the membrane, an α-helical trans-SNARE complex is formed between the SV SNARE

protein, synaptobrevin/VAMP and plasma membrane SNAREs, syntaxin 1 and SNAP-25 (Synaptosomal-associated protein 25) (Figure 3d). This tightening of the SNAREs brings the membrane of the vesicle and plasma membrane very close to each other and eventually to their fusion and release of their content (Figure 3e) (Südhof, 2013; Rizo and Xu, 2015; Kaeser and Regehr, 2017).

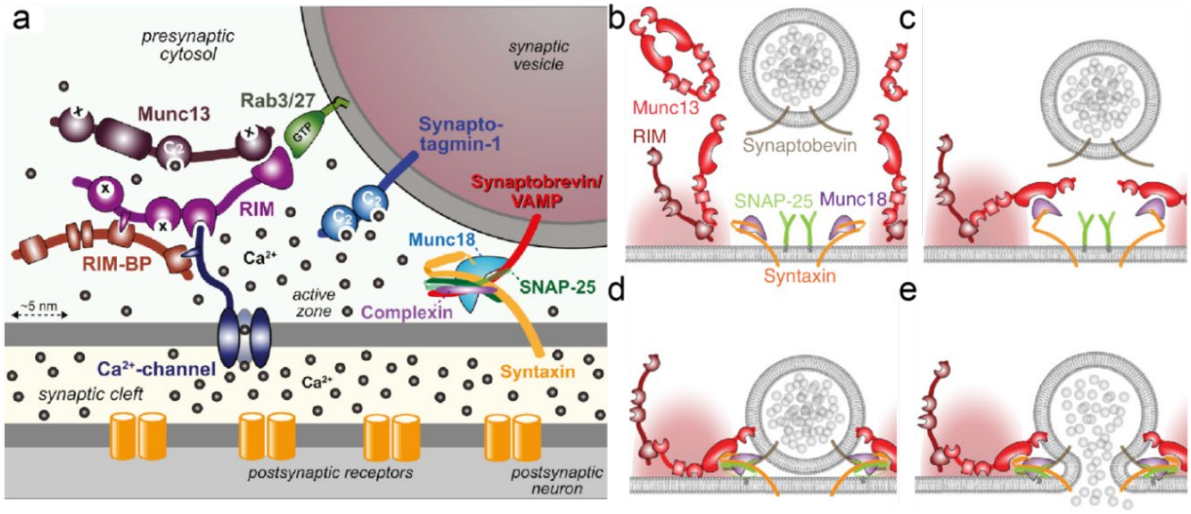

Figure 3: Simplified view of the principal players involved in SV exocytosis

a) Main players involved in SV priming, docking and molecular machinery mediating Ca^{2+} triggered exocytosis. Figure adapted from Südhof, 2013 **b)** RIM and Munc13 recruit SVs to release sites. **c)** Munc13 and Munc 18 mediate the opening of syntaxin **d)** SNARE complex assembles **e)** SNARE zippering leads to membrane fusion. Figure and legend adapted from Kaeser and Regehr, 2017.

1.4.1.1 Fusion mode

Exactly how SVs fuse with the plasma membrane is very controversial and still is a matter of debate mainly because of conflicting results and interpretation. Some studies show evidence for different fusion modes leading ultimately to varying amounts of glutamate released in the cleft and therefore to analog vs quantized synaptic signaling. The mode of vesicular release is hotly debated since Katz described his quantal theory of

neurotransmission. An alternative kiss-and-run (KR) process has been suggested: SVs release their content partially or entirely through a short-lived fusion pore that opens transiently without the SV entirely collapsing with the plasma membrane (Figure 4b) (Ceccarelli et al., 1973). During this process, the SV keeps its shape and molecular identity and can rapidly be retrieved from the plasma membrane and be reused within seconds. A KR type of SV fusion has mainly implications for the speed of vesicle retrieval from the plasma membrane. The role of KR at CNS synapses has been hypothesized to either save energy for the presynaptic terminal by allowing multiple rounds of KR or to serve as a differential way of signaling like in the case of large dense core vesicles secreted by chromaffin cells (Alabi and Tsien, 2013). Evidence and speculation of KR at CNS synapses are the result of the use of several optical readout methods like lipophilic FM dye destaining, pHluorin-based pH responses (for more detailed explanations see section 1.6.2.1 and 1.6.2.2), quantum dot unquenching and escape. pHluorin expression in the lumen of SVs represents the most common approach for optical monitoring of vesicle fusion and retrieval. Briefly, when a SV is exocytosed, protons get diluted which unquenches the pHluorin leading to an increase in the signal. After being retrieved from the membrane, the SV is re-acidified, and the fluorescence of the pHluorin is quenched. A rapid decrease of the fluorescence to baseline is interpreted as a KR event (Figure 4a). The occurrence of KR versus full-fusion has been shown to be highly variable and depends on several factors. The location of the vesicle fusion relative to the center of the AZ influences the fusion mode with centrally fusing vesicles undergoing KR and AZ outer-edge located vesicles mainly undergoing full fusion (Park et al., 2012). A study has shown that an increase in stimulation frequency at hippocampal synapses leads to a gradual increase of full-fusion as opposed to KR (Harata et al., 2006). An increased presynaptic Ca^{2+} influx, longer stimulus duration, and high p_r have also been shown to increase the fraction of vesicles undergoing full-fusion at the expense of KR (Alabi and Tsien, 2013). All those parameters influencing the type of fusion mode lead to

conflicting findings even in experiments done in comparable systems. Alternatively, a study investigating the mechanisms of endocytosis could explain how hippocampal synapses can sustain high-frequency stimulation without the need of a KR fusion mode (Watanabe et al., 2013b). By combining optogenetic stimulation and high pressure freezing for subsequent EM, Watanabe et al., showed that bulk endocytosis of multiple released SVs occurs at the edges of the AZ between 50 and 100 ms and is therefore 200-fold faster than the traditionally accepted view of clathrin-mediated endocytosis (Heuser and Reese, 1973). This major finding provided an alternative explanation on how the excess membrane of SVs fusion is rapidly retrieved to sustain high-frequency stimulation.

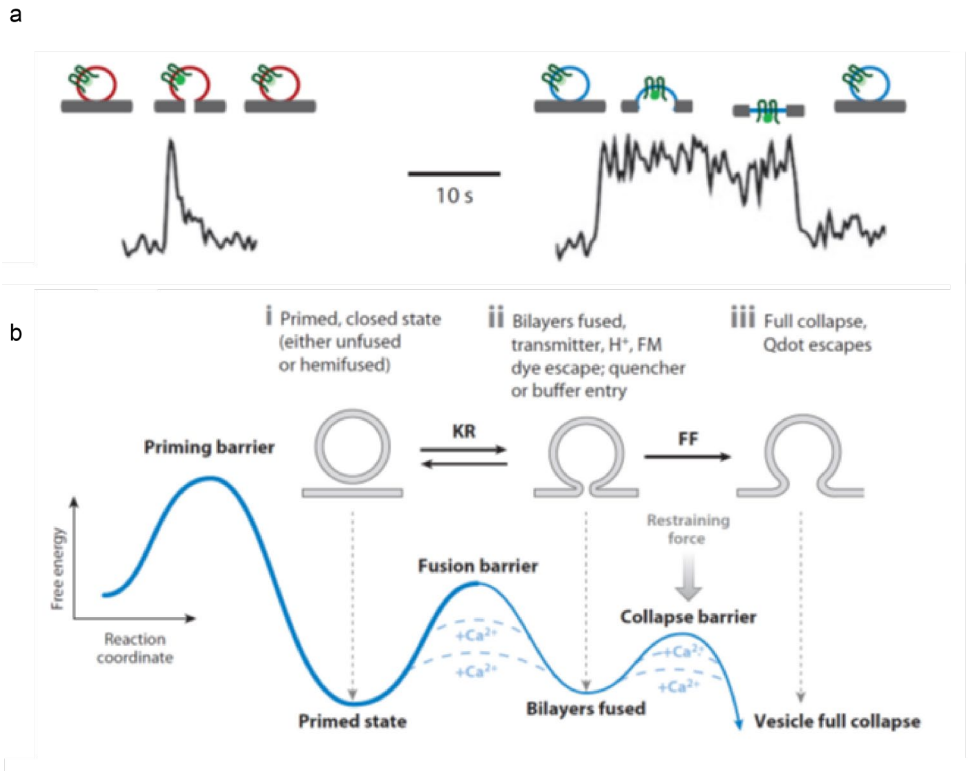

Figure 4: Detection and mechanism of kiss-and-run

pHluorin-based pH responses as a functional readout to clathrin-mediated endocytosis vs. KR and the putative mechanism driving a vesicle to release its content through KR partially or to undergo full-fusion. Figure adapted from Alabi and Tsien, 2013.

1.4.2 Synaptic vesicles endocytosis

Once a SV has fused to the membrane, the excess membrane in the presynaptic terminal has to be retrieved to prevent swelling of the terminal and to recycle SVs for another round. This mechanism is mediated by endocytosis. Several endocytotic models have been suggested. The first endocytotic model was suggested by Heuser and Reese in 1973 (Heuser and Reese, 1973) through functional and EM evidence of synaptic vesicle recycling at the frog NMJ, to be clathrin-mediated endocytosis model (Figure 5a). Later, studies refined the model describing the sequence and proteins involved from the recruitment of the clathrin coat to the site of endocytosis and the fission and formation of new SVs (Kaksonen and Roux, 2018). According to this mode of operation, SV recycling had a time constant of approximately 14-20 seconds for completing the whole cycle from exocytosis to refilling of NTs to be ready for a new round of release (Balaji and Ryan, 2007; Granseth et al., 2006). Recruitment and assembly of the building blocks of the clathrin coat (clathrin triskelia) limit the kinetics of this mode of endocytosis. Large variability in kinetics has been observed depending on the preparation and the conditions of the measurements. Ceccarelli and colleagues introduced in 1973 (Ceccarelli et al., 1973) the clathrin-independent mechanism of recycling discussed in the previous section 1.4.1.1. In this kiss-and-run fusion mode, SVs maintain their molecular identity and is thought to be again release ready within seconds (Figure 5b) (Alabi and Tsien, 2013).

Clathrin-mediated endocytosis has long been considered as the main mechanism when only a few SVs fuse with the membrane, while activity-dependent bulk endocytosis has been provided as the main model of SV retrieval during strong neuronal activity (Figure 5c). Miller and Heuser first reported this mode of endocytosis at the frog NMJ in the 80s (Miller and Heuser, 1984). Later, other studies have shown evidence for activity-dependent bulk endocytosis in typical small CNS synapses during elevated neuronal activity (Clayton and

Cousin, 2009). This mode of endocytosis allows retrieving SVs within seconds to a minute, hence, more likely to sustain SV recycling during high-frequency activity.

An electron microscopy (EM) technique termed ‘flash-and-freeze’ allows optogenetically stimulating cells expressing a light-sensitive opsin and subsequently capturing the membrane dynamics by high-pressure freezing at different intervals after the stimulation. This technique allowed identifying a new mode of vesicle endocytosis called ultrafast endocytosis (Figure 5d), in motor neurons of *Caenorhabditis elegans* and pyramidal neurons of mouse hippocampus (Watanabe et al., 2013b; Watanabe et al., 2013a). Briefly, after a single stimulus, the excess membrane is recovered on the sides of the AZ (as opposed to KR where the SVs are up taken at the AZ directly). This process is clathrin-independent and thus, happens within 100 ms. However, for SV budding from the endosome, clathrin is required.

Altogether, discrepancies between studies concerning the main mode of endocytosis might be a consequence of different experimental conditions such as temperature, preparation, state of maturity of the cells and stimulation protocol. For instance, ultrafast endocytosis has only been observed at physiological temperatures but not at room temperature.

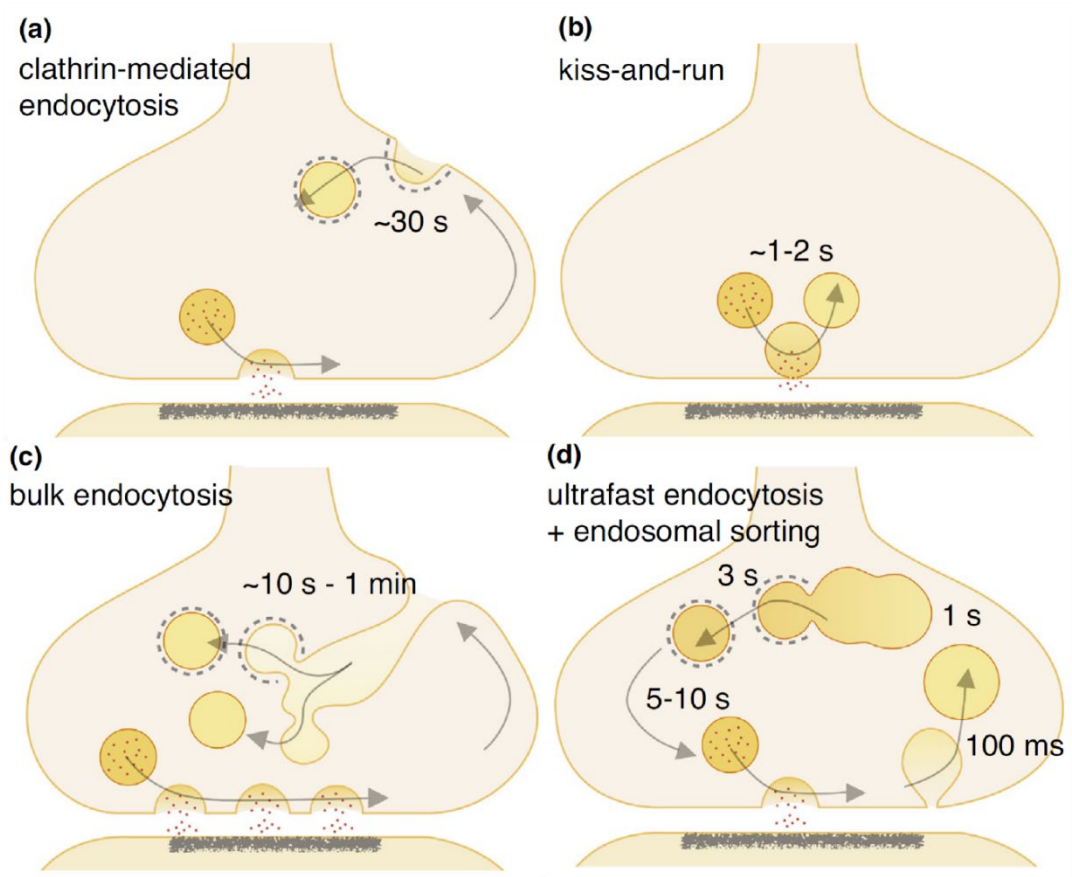

Figure 5: Models of synaptic vesicle recycling

Four endocytotic mechanisms described at CNS synapses. Figure modified from Watanabe and Boucrot, 2017.

1.4.2.1 The 'presynaptic quantum'

After a SV is endocytosed, it gets refilled with glutamate before becoming fusion ready for a new vesicular cycle. First, the lumen is acidified by a proton influx mediated by an H^+ ATPase. By rapid quenching approaches in primary rat hippocampal neurons, different studies estimated the SV re-acidification to take approximately 4 s (Granseth et al., 2006; Atluri, 2006). This proton gradient is then used to exchange a proton for a molecule of glutamate via the proton-glutamate exchangers VGLUT1-3. Cl^- has been recently shown to also play a role in the kinetic of SV reacidification and glutamate exchange with a proton

(Martineau et al., 2017). The influence of glutamate filling into individual SVs and their variability in size on the amount of glutamate released upon vesicle fusion is still under debate.

In rat hippocampal neurons, the average outer-diameter of SVs was estimated to be 35–45 nm which corresponds to an average volume of vesicle lumen (considered as a physiologically more relevant measure) of 11'500 nm^3 (Schikorski and Stevens, 1997; Harata et al., 2001; Harris and Sultan, 1995). The mean SV volume varies up to five-fold (5000 nm^3 to 25000 nm^3) among neighboring excitatory rat hippocampal neurons both *in vitro and in vivo* (Qu et al., 2009; Hu et al., 2008). As the SV volume scales with the third power of its radius, a small change in vesicle diameter leads to a substantial change in glutamate storage capacity. It is not possible to directly investigate whether there is a correlation between SV size and quantal amplitude at small CNS synapses as somatic recordings do not allow identifying a quantum due to the different electrotonic distances of different synapses.

Nevertheless, some studies investigating the level of VGLUT1 in mice hippocampal cultures have shown that quantal size and size of SV is upregulated when VGLUT1 is overexpressed, whereas it was decreased in VGLUT1 KO neurons (Wojcik et al., 2004; Daniels et al., 2006). Furthermore, the expression level of VGLUTs has a strong influence on the release probability (Herman et al., 2014). SVs are not filled to their maximum capacity leaving room for regulation as demonstrated by optogenetic manipulation of SV filling state (Rost et al., 2015). The same study showed that 'fuller' vesicles undergo exocytosis more easily.

Whether there is a correlation between the SV size and their proximity to the plasma membrane in the presynaptic terminal is unclear and controversial. On the one hand, a study has shown that docked synaptic vesicles were found to have a smaller diameter (23-49 nm) than the non-docked vesicles (20-60 nm) (Harris and Sultan, 1995). On the other hand, a more recent study done in organotypic hippocampal preparation using high-pressure

freezing as a fixation method, found a tendency for vesicles close to the active zone to have a larger diameter (Fernández-Busnadiego et al., 2010).

1.5 Release probability

The release probability (p_r) is the measure of the likelihood that at least a vesicle gets released upon arrival of an action potential (AP) and is a consequence of the stochastic nature of the molecular machinery driving SV exocytosis. The vesicular release probability (p_{ves}) is the probability that the Ca^{2+} influx in the presynaptic terminal triggers exocytosis of an individual SV. Therefore, in a binomial model of NT release, p_r is determined by both p_{ves} and n the number of vesicles, so that $p_r = 1-(1-p_{ves})^n$.

The correlation between the structure of synapses and their function - the synaptic strength - has been extensively characterized. Several studies looked at the correlation between the p_r of presynaptic terminals and other parameters. Using a correlative transmission electron microscopy approach, a study investigating the relationship between the function and the anatomy of hippocampal synapses found that p_r of a single synapse (p_{syn}) correlated with the number of docked vesicles at the AZ (Branco et al., 2010). Functional measurement of p_r before correlative EM has shown evidence for a correlation between p_{syn} with the number of docked vesicles and the AZ area (Holderith et al., 2012). In summary, larger presynaptic terminals have a larger AZ with more docked SVs and a higher p_{syn}. Furthermore, postsynaptic density s ize has been shown to correlate with the size of the AZ and number of docked SVs (Schikorski and Stevens, 1997). Nevertheless, p_r is not a fixed value but is modulated by patterns of activity due to intrinsic and extrinsic factors. The p_r not only defines the reliability of the synapses but gets also modulated during ongoing synaptic activity to adjust for the requirements of the pattern of activity. When an AP reaches

nerve terminals, it leads to opening of voltage-gated calcium channels (VGCCs) located close to the release machinery of docked SVs. This increase of local Ca^{2+} concentration is necessary for triggering vesicular fusion and release of NTs (Katz and Miledi, 1967). The open probability, duration of Ca^{2+} channels opening, intracellular Ca^{2+} stores and Ca^{2+} buffers located in proximity to VGCCs account for the natural variability among presynaptic terminals. The [Ca^{2+}] at the nanodomain and the sensitivity of the Ca^{2+} sensor of the release machinery mediating SV exocytosis determine the likelihood that a given SV undergoes exocytosis upon AP invasion and thus directly modulate p_{ves} of individual docked vesicles. SV exocytosis rate scales with a 3rd–5th power- law relationship between Ca^{2+} influx and exocytosis (Dodge and Rahamimoff, 1967). Thus, modest changes in Ca^{2+} have a significant influence on synaptic release.

1.5.1 P_{ves} regulation

Ca^{2+} imaging in presynaptic terminals of hippocampal neuronal cultures using the synthetic Ca^{2+} sensor Fluo-4 and a variety of different Ca^{2+} channels blockers, showed that P/Q-type and N-type VGCCs are the main sources of spike-evoked Ca^{2+} entry (Ermolyuk et al., 2013). Nearby to VGCCs, the concentration of Ca^{2+} is high enough to trigger the release of a SV. The number and proximity of VGCCs to SVs affect the amount of Ca^{2+} available to trigger SV exocytosis. SVs have been reported to be located from 10 nm (Schmidt et al., 2013) to 100 nm (Vyleta and Jonas, 2014) away from the VGCCs depending on the type of synapse. The main protein responsible for coupling SVs to VGCCs is RIM as it binds to SVs via Rab3 and directly to calcium channels of the Cav2.1 (Wang et al., 1997) and Cav 2.2 (Kaeser et al., 2012) family. VGCCs have been found to form clusters at the AZ (Holderith et al., 2012). In their study, Holderith et al., performed optical quantal analysis in *stratum oriens*

using two-photon imaging of [Ca^{2+}] transient influx through *N*-methyl-D-aspartate (NMDA) receptors. By evoking presynaptic release of glutamate in response to extracellular stimulation, they were able to distinguish release successes from failures to assess the p_r at individual synapses. A post hoc ultrastructural analysis of those same synapses by 3D electron microscopy reconstruction and gold particle labeling of VGCCs P/Q type Cav2.1 showed that the number of Cav2.1 channels linearly correlates with the p_r at individual synapses. Hoppa et al., in 2012 showed that the $\alpha 2\partial$ subunit of those VGCCs directly controls their abundance at the AZ. Consequently, this subunit directly influences p_{ves} upon AP propagation. The local Ca^{2+} concentration depends not only on the number of VGCCs opening upon arrival of an AP but also on the amount of Ca^{2+} flowing in upon opening of a channel. State, subtype and alternative splicing modulate the amount of Ca^{2+} flux through the VGCCs (Nanou and Catterall, 2018). Furthermore, the AP width determines the duration of VGCCs open state. Taking advantage of a fast genetically-encoded voltage indicator to optically monitor the AP width along the axonal arbor, Hoppa et al., 2014 identified the potassium channels Kv3.1 and Kv1 to modulate the AP waveform at small nerve terminals in dissociated primary neurons. A larger AP width increases the Ca^{2+} influx upon AP propagation and vice versa: The AP width very efficiently controls the Ca^{2+} influx and thus the release properties of the synapse. Other mechanisms involved in intracellular Ca^{2+} handling such as mitochondria-dependent Ca^{2+} buffering, ER Ca^{2+} induced Ca^{2+} released (CICR), pumps for extrusion mechanisms and endogenous buffer contribute to shaping the Ca^{2+} influx upon AP invasion (Devine and Kittler, 2018). Altering cytosolic Ca^{2+} buffer capacities by exogeneous application of chelators strongly influences p_r (Awatramani et al., 2005). Depletion of the endoplasmic reticulum (ER) Ca^{2+} stores also decreases the p_r at physiological temperature (de Juan-Sanz et al., 2017). Numerous regulators have been shown to modulate VGCCs and subsequent Ca^{2+} influx modulation. For instance, activation

of $GABA_BRs$, α2-noradrenergic receptors, cannabinoid receptors and mGluRs have all been shown to inhibit VGCCs and therefore decrease p_r (Körber and Kuner, 2016).

1.5.2 Number of vesicles (n)

Hippocampal synapses contain on average 100-200 SVs (Schikorski and Stevens, 1997) but only a small fraction are in close apposition to the plasma membrane as revealed by EM (Denker and Rizzoli, 2010). Those vesicles are called docked vesicles and are believed to be ready for exocytosis. An increase in the number of docked vesicles or release sites leads to an increase in p_{syn} as the number of available vesicles upon Ca^{2+} influx is increased. In fact, p_r has been shown to be also modulated through an increase in the size of the total vesicular pool, for example through modulation of vesicle trafficking (Darcy et al., 2006). Therefore, modulation of the number of docked SVs can further shape the presynaptic efficacy. Statistical analysis of amplitude fluctuation provides the maximum number of vesicles that can be released. At a single synapse, this number of SVs is thought to correspond to the number of docked SVs. Besides quantal analysis, other methods have been developed to obtain a functional readout of the number of release sites. A widely used approach is to measure the so-called readily releasable pool (RRP). The RRP is the pool of SVs that is released upon application of high osmolarity solutions (Rosenmund and Stevens, 1996). Whether the functional measurement of the RRP corresponds to the morphological correlate of the number of release sites is still not entirely clear.

1.5.3 Modulation of p_r and short-term plasticity

The efficacy of synaptic transmission is not constant but changes dynamically during high-frequency activity. Concerning information processing, different forms of short-term

plasticity that last for at most a few minutes, act as specific frequency filters: facilitating synapses are most effective during high-frequency bursts, while depressing synapses preferentially transmit isolated spikes preceded by silent periods (Markram et al., 1998). A well-described phenomenon termed facilitation of transmission is the accumulation of Ca^{2+} in the presynaptic terminal during high-frequency trains of action potentials, which as a consequence of a Ca^{2+} build-up, leads to a higher p_r (von Gersdorff and Borst, 2002). Mechanistically, many pre- and postsynaptic parameters change dynamically during high-frequency activity. The 'residual Ca^{2+} hypothesis' is well accepted as a model for presynaptic facilitation. The facilitation upon propagation of the 2nd consecutive AP is caused by the accumulation of Ca^{2+} fluxing into the terminal and the remaining intracellular [Ca^{2+}] from the 1st AP leading to a higher [Ca^{2+}] in the presynaptic terminal and thus to a more substantial p_r. The residual Ca^{2+} hypothesis is assumed to be the primary mechanism for different time scales of facilitation, short-term facilitation (lasts up to 100 ms), augmentation (~5-10s) and post-tetanic potentiation (PTP) (~30s). Evidence that elevating presynaptic Ca^{2+} enhances AP-evoked release and buffering presynaptic Ca^{2+} reduces short-term enhancement have actively supported this hypothesis (Zucker and Regehr, 2002). A study has recently shown that there is a specific calcium sensor, synaptotagmin-7, whose identity has been extensively debated over the last decades, that is responsible for this short-term enhancement in the p_r (Jackman et al., 2016). Synaptotagmin-7 is a distinct Ca^{2+} sensor than the fast sensors responsible for SVs exocytosis. As opposed to facilitation, a train of APs can also temporarily deplete the pool of available readily releasable vesicles, thus, leading to a transient decrease in p_r termed short-term depression. The most common mechanism thought to mediate short-term depression is through depletion of the RRPs leading to a transient decrease in NT release upon several consecutive APs.

However, numerous studies have also shown the locus of short-term plasticity expression to be postsynaptic. Desensitization of postsynaptic receptors (a state in which a

receptor is bound to the ligand but is in a non-conducting state) leads to a use-dependent decrease in synaptic strength (Colquhoun et al., 1992). Desensitization of AMPARs can lead to a decrease in quantal size at hippocampal glutamatergic synapses (Larkman et al., 1997). In the range of seconds to minutes, postsynaptic receptors can undergo several other alterations induced by Ca^{2+}-activated enzymes. As many different mechanisms are involved in mediated short-term plasticity, it is not straightforward to distinguish between pre- and postsynaptic plasticity mechanisms. Furthermore, electrophysiological analysis of short-term plasticity, by monitoring postsynaptic responses, is complicated by the fact that more than one synapse often connects two neurons.

1.6 Monitoring presynaptic function

1.6.1 Electrophysiological approaches for assessing changes in p_r

One of the fundamental parameter setting synaptic strength is the release probability p_r. Several electrophysiological methods based on electrophysiological recordings of the postsynaptic target cells have been developed to monitor p_r. However, those methods only provide estimates of relative changes since there is an intermingled contribution of pre- and postsynaptic components contributing to the variability in synaptic transmission. The quantal analysis described and discussed in detail in section 1.7 represents the classic method for quantal parameter extraction including p_r.

Synapses with a low initial p_r exhibit use-dependent facilitation whereas synapses with a high p_r exhibit use-dependent depression as a consequence of a finite number of RRP (Debanne et al., 1996). The dependency of the paired-pulse ratio (PPR, ratio of the second EPSC to the first EPSC after stimulation a connection with two consecutive action potentials) on the p_r of the first AP has been shown to be a ubiquitous mechanism. This relationship

lead the PPR to become a commonly used mean of assessing presynaptic changes in the p_r. The PPR is the ratio of the second EPSC to the first EPSC (Zucker and Regehr, 2002). In long-term plasticity experiments, an equal PPR before and after plasticity induction is used as an indicator of a purely postsynaptic mechanism of plasticity (Costa et al., 2017). Even if this method has been used extensively, it remains a very indirect and relative estimate of p_r.

The progressive block of postsynaptic NMDAR-mediated currents with the irreversible open-channel blocker MK-801 applied intracellularly in the postsynaptic cell has allowed to assess changes in p_r (Rosenmund et al., 1993). The response amplitude is gradually reduced as open NMDARs are getting irreversibly blocked. The NMDAR current block is thereby proportional to the frequency of glutamate released and fitting the NMDARs blocking rate with a kinetic model enables extraction of the p_r.

The coefficient of variation (CV=standard deviation/mean) of the amplitude distribution of the postsynaptic currents has been used as a proxy for changes in presynaptic glutamate release. Briefly, if more postsynaptic receptors are occupied (due to more NT in the cleft), the variation in amplitude of the synaptic currents due to the stochastic properties of the receptors is lower. Therefore, a reduced CV of synaptic current implies an increase in NT release and vice versa. The methods mentioned above remain indirect ways of monitoring p_r and lack any spatial information. Besides, none of those electrophysiological measures allows assessing whether it is an increase in p_{ves} or an increase RRP responsible for an increase in p_r. To this end, in this study I took advantage of genetically encoded glutamate sensor to directly measure the release of glutamate at the cleft.

1.6.2 Indicators of synaptic release

Synaptic transmission plays an essential role in information processing and memory formation. For optical monitoring of synaptic transmission, two main strategies have been

used so far, direct detection of NTs or measurement of pH change during vesicle exocytosis/recycling.

1.6.2.1 FM dyes

FM dyes are fluorescent lipophilic dyes initially developed to study vesicle recycling at the NMJ (Betz and Bewick, 1992). Briefly, when vesicles are released from the presynaptic terminal, the dye is trapped into the vesicular membranes and become fluorescent upon light excitation. A major drawback of those dyes is the need to apply strong stimulation protocols to load the dye into the vesicles, which can by itself induce plasticity. Furthermore, as the dye gets released once vesicles undergo exocytosis, several rounds of loading are necessary for repeated measurements. Nevertheless, this technique has still been widely applied to decipher release properties. A study at Schaffer collateral synapses in rat acute slices used FM dyes to demonstrate that induction of an NMDAR-dependent form of LTD leads to a decreased release probability (Zhang et al., 2006).

1.6.2.2 pHluorins

pHluorins are fluorescent probes reporting changes in pH. When exposed to the inside of vesicles where the lumen of the vesicle is maintained at an acidic pH of ~ 5.6, the fluorescence is quenched, whereas, during exocytosis, the lumen of the vesicle is exposed to the extracellular space (pH ~ 7.4) leading to an increased fluorescence. As at each recycling cycle of the vesicles, protons are pumped back into the lumen of the vesicles it is possible to track the changes in vesicular pH to report neurotransmission. SynaptopHluorin was the first genetically encoded pH indicator (Miesenböck et al., 1998). The sensor is based on pH-sensitive GFP variant fused to the C-terminus of synaptobrevin/VAMP2 (vesicular

associated membrane protein-2) permitting localization of the sensor to the inner surface of synaptic vesicles. Some other vesicular targeting strategies of the pHluorin have been used, notably fusion of the pH-sensitive GFP to synaptophysin (Granseth et al., 2006), synaptotagmin (Fernández-Alfonso et al., 2006) and the vesicular glutamate transporter VGLUT (Voglmaier et al., 2006). Spectrally red-shifted sensors with a red fluorescent pH-sensitive protein like VGLUT-mOrange2 (Li, 2011) and sypHTomato (Li and Tsien, 2012), present the advantage that they can be used in combination with green Ca^{2+} indicators. Compared to FM dyes, pHluorins do not need multiple loadings into vesicles throughout the experiments. Still, for p_r assessment in intact tissue, trains of action potentials are necessary as the low intrinsic signal to noise ratio (SNR) of the dye is insufficient to detect the release of single SVs in response to single APs. This approach was refined in our lab with the two-color sensor Ratio-sypHy (Rose et al., 2013). The pH-sensitive green fluorescent protein synapto-pHluorin allows monitoring vesicle fusion events, and development of a ratiometric version of synaptophysin-pHluorin enables investigation of recycling pool size in Schaffer collateral boutons.

pHluorins have been used successfully to measure the fluorescence change at presynaptic terminals corresponding to single vesicle events in dissociated neuronal cultures (Balaji and Ryan, 2007*;* Gandhi and Stevens, 2003; Zhu et al., 2009*).* Recently, a study showed that individual fusion events of vesicles monitored with VGLUT 1-pHluorin can be localized (Maschi and Klyachko, 2017). However, their low SNR prevents their use for detecting individual fusion events in intact tissue. In addition, due to their pH-based fusion, there is no information about the filling state with NTs.

1.6.2.3 Optical glutamate sensors

Currently, the best way to measure the release of NTs at the level of individual synapses in living tissue is through a combination of fluorescent microscopy with optical sensors. Many glutamate sensors, genetically encoded or synthetic dyes, based on different mechanisms have been developed in the last decade but without gaining much popularity among neuroscientists.

EOS glutamate (E) Optical Sensor is a hybrid protein based on the ligand-binding domain of AMPA subunit conjugated with a small fluorescent molecule dye near the glutamate-binding pocket (Namiki et al., 2007). Later, improved variants displaying a broader dynamic range and lower affinity have been developed (Okubo et al., 2010). Unfortunately, due to the low dynamic range of the sensor ($\Delta F/F_0$ 0.2 - 0.48), its use stays limited in imaging synaptically released glutamate of dissociated hippocampal neurons or in monitoring extrasynaptic glutamate dynamics in intact tissue.

Another strategy was the generation of a semi-synthetic ratiometric fluorescent sensor called Snifit-iGluR5 for glutamate by fusion of a donor-fluorophore linked to an acceptor fluorophore and the glutamate binding protein iGluR5-S1S2 (Brun et al., 2012). This FRET sensor (Förster resonance energy transfer) showed an improved change in fluorescence yet insufficient for use in intact tissue (ΔRatio: 1.56). Semi-synthetic indicators present several disadvantages: cell-specific, sparse expression and long-term repetitive imaging are not possible.

1.6.2.4 Genetically encoded glutamate indicators (GEGI)

Before the membrane-bound glutamate sensor iGluSnFR (Marvin et al., 2013) used for my experiments became available, several other glutamate sensors based on the same principle had already been developed. The very first genetically encoded glutamate indicator

called FLIPE (Okumoto et al., 2005) is the result of the insertion of GltI sequence between and N-terminal enhanced cyan fluorescent protein (ECFP) and a C-terminal yellow fluorescent protein called Venus. The sensor could be expressed on the surface of cells and reported glutamate transients as a concentration-dependent decrease in FRET efficiency. GluSnFR (Tsien, 2005), another FRET-based glutamate indicator, is the result of GltI insertion between ECFP and another yellow fluorescent protein termed Citrine. Site-directed mutagenesis allowed to obtain a FRET sensor, GluSnFR, displaying a lower affinity to report glutamate dynamics at the surface of neurons and a larger dynamic range by adjusting the linker between ECFP and Citrine. The resulting most suitable sensor for monitoring glutamate at the surface of neurons was named SuperGluSnFR (Hires et al., 2008) with a ΔR max 44 % and a K_d of 2.5 μM. This SuperGluSnFR allowed measurements of the time course of synaptic glutamate release and spillover in hippocampal dissociated cultures. Nevertheless, the SNR of the sensor is low and ~ 30 single APs stimulation have to be average to measure a synaptic glutamate transient. Those sensors were eventually modified to reach sufficient SNR in intact tissue and adequate affinity for monitoring cleft glutamate dynamics.

The genetically encoded sensor for glutamate termed iGluSnFR (Marvin et al., 2013) made a breakthrough in the field of glutamate imaging and is now by far the most used and popular glutamate sensor. iGluSnFR is a single-wavelength membrane bound sensor based on the binding site GltI of *E.Coli* and a circularly permutated (cp) EGFP. Its brightness (4.5 $\Delta F/F_{max}$) and K_d of ~4 μM make it a suitable tool for investigating cleft glutamate dynamics. A more detailed description of iGluSnFR and its structure is provided in section 3.8.2. While this present study was conducted, iGluSnFR became a widely used tool to report glutamate dynamics in various systems, notably the retina (Borghuis et al., 2014), visual cortex (O'Herron et al., 2016), olfactory bulb (Brunert et al., 2016). Very recently, the group of Robert

E. Campbell (Wu et al., 2018) developed a red intensity-based glutamate sensing variant of the original iGluSnFR that they named R-iGluSnFR1. In brief, they replaced the GFP protein of the iGluSnFR with a yellow-light excitable red fluorescent protein (Shaner et al., 2008) and show that their sensor is sensitive enough for resolving single AP-evoked glutamate transients by field stimulation in dissociated hippocampal neurons. A common limitation with red-shifted sensors like red Ca^{2+} sensors is their low fluorescent brightness and dynamic range. Campbell's lab introduced numerous point mutations in the GItI-derived domain and the red fluorescent protein to finally develop a new glutamate sensor displaying a dynamic range of 4.9 and a K_d of 11 µM a single-photon excitation peak at 562 nm and an emission peak at 588 nm. Furthermore, others and our lab together with our collaborators (see publication inf section 3.8) worked on the development of iGluSnFR variants displaying different kinetics (faster and slower on- and off-rates) with consequently different affinities for glutamate binding (section 3.8). Meanwhile the group of Loren L. Looger who initially engineered the original iGluSnFR developed a range of iGluSnFR variants (different affinities and kinetics with blue, green and yellow emission profiles) with improved stability and brightness. The improved brightness of their sensors was achieved by substituting the circularly permuted enhanced green fluorescent protein (cpeGFP) with a cp 'superfolder' GFP which leads to a stronger expression level at the membrane (Marvin et al., 2017). Those different variants serve different purposes and depending on the area of study (brain region vs. single synapse) and also the imaging system available (camera, galvanometer scanners or resonant scanners), different sensor kinetics can be used.

1.7 Quantal analysis at CNS synapses

The synaptic efficacy or synaptic strength depends on three parameters: the total number of vesicles ready to be released *n*, the release probability of a single vesicle (p_{ves}), and the

quantal content (q) or postsynaptic current in response to the release of a single presynaptic vesicle. Mathematically the synaptic efficacy can be described by the product of three parameters (synaptic efficacy = $n*p_{ves}*q$) (Redman, 1990). Quantal analysis aims at extrapolating the three quantal parameters defining the synaptic strength, namely, n, p_{ves}, q as defined by Bernard Katz in 1954 at the frog neuromuscular junction (discussed in section 1.2). The idea is to use a binomial model to predict the amplitude distribution of n, p_{ves}, q and standard deviation of q (σ_q). This prediction is then compared with the actual distribution. Katz's theory of quantal release by statistical analysis of postsynaptic current amplitude fluctuations is based almost exclusively on measurements obtained at the NMJ, which is a long ribbon-like giant structure with many available vesicles for release. At this synapse, an electrode is placed directly into the postsynaptic density for recordings. However, this is not as straightforward as in a typical pyramidal neuron contacted by several thousands of axons over the entire dendritic arborization where the responses are recorded at the soma. As the basis of quantal analysis relies on the measurement of a single quantal synaptic contact, applying the quantal model like at the frog NMJ represents a challenge to CNS synapses as excitatory postsynaptic currents are not directly measured at synapses like for NMJ. The unknown number of synaptic contacts renders the interpretation of the variability in the amplitude of EPSCs much more complex. Regardless of the number of connections between to pre- to the postsynaptic cell, there is a whole range of further variables that should be considered. Depending on the location of the synaptic contacts, the EPSCs appear very small at the soma and the noise from spontaneous synaptic activity precludes their detection. Furthermore, a single vesicle released at a distal dendritic synapse creates smaller EPSCs than a vesicle released at a perisomatic synapse due to stronger electrotonic attenuation. Hence, viewed from the soma, there is no unitary response precluding the identification of EPSC quantal increments.

According to the degree of occupancy of postsynaptic receptors, the release of two vesicles (i.e., two quanta) does not necessarily lead to postsynaptic current amplitude twice as large. Furthermore, synapses have different numbers of receptors, thus, they are electrically different leading to different quantal amplitudes. For this reason, quantal analysis as at the frog NMJ is not directly applicable at small CNS synapses. Considerable effort has gone into the development of different analytical and methodological approaches for adapting quantal analysis at CNS synapses. It is the only means for discriminating the loci of alteration of synaptic efficacy (pre- or postsynaptic) and is of paramount importance for understanding and characterizing the type of plasticity occurring at a specific synapse. As many difficulties accompany analysis and binomial-model fitting to the recorded EPSC fluctuation for estimating the quantal parameters, different experimental approaches have been established to determine how many vesicles are released at CNS synapses. With electrophysiology alone, however, it is difficult to distinguish between stimulation of multiple synapses and stimulation of a single synapse that is capable of multivesicular release leaving room for result interpretation.

1.7.1.1 The one site-one vesicle hypothesis

A step forward has been made in the field of quantal analysis at CNS synapses when analysis of amplitude fluctuations of synaptic potentials was combined with morphological reconstruction of the connection(s) of the pre- and postsynaptic cells. Postsynaptic recordings in the Mauthner cell of evoked inhibitory PSC through stimulation of a presynaptic interneuron followed by correlative EM to reconstruct the morphology and site of contacts between the pre- and postsynaptic cell allowed direct comparison of functionally and morphologically defined release sites (Korn et al., 1981). In this study, Henri Korn observed a one-to-one relationship between the maximal number of quantal peaks in responses

amplitude distributions and the number of presynaptic boutons. The resulting interpretation was that at most one vesicle can be released per release site in a probabilistic manner in response to a single AP. This conclusion built the foundation for the all-or-none or 'uniquantal' hypothesis for small CNS synapses (Redman, 1990). Other studies using different methodological or analytical approaches to quantify vesicle number, further supported this hypothesis. Another early study attempting quantal analysis in the CNS used postsynaptic motorneurons recordings of the mammalian spinal cord (Jack et al., 1981). Several studies based on statistical analysis of postsynaptic responses amplitude fluctuations found that the time course of the different EPSPs is associated with the amplitude. Jack and colleagues used this principle to compensate for different synaptic weights. They combined focal stimulation and classical quantal analysis through distribution deconvolution with a Gaussian template, together with the morphological reconstruction for proper dendritic filtering compensation according to the location of the connections. They provided evidence for a one-to-one correlation between the number of quanta in the histogram count and the number of terminals connecting the recorded neuron. However, univesicular release model and an equal quantal size are assumed for dendritic filtering corrections. Thus, different amplitudes are interpreted as postsynaptic responses arising from different synaptic contacts with different electrotonic distances.

Several methodologies have been used for recordings at small CNS synapses, to ensure unitary EPSPs. For instance, recording of minimal focal stimulation has been widely used to analyze presumably single-synapse responses (Raastad et al., 1992; Dobrunz and Stevens, 1997) but those experiments must be interpreted carefully. The selection of stimulation conditions which yield all-or-none responses may introduce a bias towards weak synapses, discarding synapses with a multi-quantal profile. Besides, this method depends on a faithful translation of the synaptic glutamate concentration into an AMPAR-mediated current that is measured at the soma of the postsynaptic cell. Furthermore, for unequivocally ensuring a

recording from a single synaptic connection, a morphological reconstruction with ultrastructural confirmation would be required. Nevertheless, the one site-one vesicle became a widely accepted principle of synaptic transmission (Redman, 1990; Stevens, 2003). However, this dogma has not remain unchallenged. EM studies at CNS synapses showed heterogeneity among synapse size and their number of postsynaptic receptors that positively correlates with the size of mPSCs amplitude (Nusser et al., 1997). Thus, variability among synaptic contacts is not only a consequence of dendritic filtering, but quantal size variability arises from the number of postsynaptic receptors. Consequently, histogram count deconvolution cannot be analyzed anymore assuming equal quantal size. EM studies also revealed the existence of boutons containing multiple AZs, termed multisynaptic boutons (Redman, 1990; Stevens, 2003) therefore the one site-one vesicle rather became one active zone-one vesicle. Later, EM data showed evidence for several vesicles being docked on a single AZ, leading to speculation about a molecular mechanism ('lateral inhibition' (Stevens, 2003)) inhibiting the simultaneous release of several docked vesicles. But not only are large fluctuations of evoked synaptic responses and a large amount of glutamate in the cleft challenging to explain through the one vesicle-one site hypothesis, but also potential saturation of postsynaptic receptors could mask the detection of multiple vesicles released simultaneously (Auger and Marty, 2000). Later, evidence of simultaneous release of multiple vesicles accumulated at many synapses and different preparation (Rudolph et al., 2015).

1.7.1.2 Multivesicular vs. univesicular release at CA3-CA1 synapses

Whether the well-studied CA3-CA1 synapses are capable of multivesicular release (MVR) is especially controversial due to numerous studies drawing different conclusions. Notably, studies using minimal stimulation in hippocampal slices saw no correlation between

the p_r and amplitude of responses when modulating the p_r. This suggests that maximally one vesicle per AZ is released (Dobrunz and Stevens, 1997; Stevens and Wang, 1995). Studies using different and innovative approaches later challenged the univesicular release (UVR) concept. An indirect approach to estimate changes in the cleft glutamate relies on monitoring postsynaptic currents in response to single AP under various p_r conditions in the presence of a low-affinity antagonist of AMPARs (Foster et al., 2005; Tong and Jahr, 1994; Christie and Jahr, 2006). The principle is as follows: in the presence of more glutamate AMPARs are blocked less efficiently by the antagonist, hence when the amount of glutamate is increased in a high p_r condition (i.e., multivesicular release), AMPAR-mediated currents present a lower sensitivity to the antagonist. Inversely, if a condition of high p_r increases the number of active synapses but not the number of vesicles per synapse (i.e., univesicular release), the sensitivity of the AMPAR-mediated currents to the antagonist remains unchanged. Several pioneering studies used this strategy to highlight the ability of small CNS synapses to release multiple vesicles. The interpretation may be complicated by the fact that the voltage-gated conductance ultimately determining the amplitude of the postsynaptic response might not scale linearly with the number of NTs notably due to saturation of those receptors. In addition, distinction between multivesicular release and increased spillover from neighboring synapses is ambiguous. Optical methods based on fluorescent Ca^{2+} indicators measure the amount of calcium influx through NMDARs termed excitatory postsynaptic Ca^{2+} transients (EPSCaTs) at individual synapses. NMDARs are less likely to saturate during synaptic transmission than AMPARs, which makes this method more suitable to detect potential changes for glutamate released. Compared to purely electrophysiological recordings, this technique allows discriminating accurately between responses and failures and to infer the p_r at individual presynaptic terminals (p_{syn}). EPSCaT measurements at CA3-CA1 synapses in acute slices estimated that more than 5 vesicles could be released simultaneously in response to a single AP (Oertner et al., 2002).

1.8 Hippocampal organotypic slice cultures

In 1954, the term ‘’organotypic ‘’ was first used for chick embryo cultures (Reinbold, D.) and since then many organs and brain regions such as the hippocampus have been cultured. Stoppini et al., 1991 improved the viability of the hippocampal slice cultures by cultivating them on semipermeable membranes separating the slice from the medium mimicking a sort of blood-brain barrier. Hippocampal organotypic slice cultures form a three-dimensional system in which the underlying connectivity of DG, CA3, and CA1 remains intact (Stoppini et al., 1991). Furthermore, development, cellular electrical properties, density and shape of spines and dendrites is very similar to the development of the *in vivo* situation at least until three weeks *in vitro* (De Simoni et al., 2003). Even capillaries have been shown to still express and secrete several factors influencing surrounding cell types despite not fulfilling anymore their role of blood transport (Moser et al., 2003; Kovács et al., 2011). The cut connections reorganize within organotypic slices to reestablish lost connections through the cutting procedure, but this leads to a slightly over-wired system, which in some cases can lead to recurrent activity. Acute slices, on the other hand, suffer from the opposite problem, as the majority of the connections are lost from the cutting procedure and not reformed.

1.9 Two-photon laser scanning microscopy

The principle of two-photon laser scanning microscopy is similar to that in conventional confocal laser scanning systems where a fluorophore is excited through a single photon absorption process. Maria Goeppert Mayer first proposed two-photon excitation in 1931. Now, this physical property is used for exciting fluorophores. In 2PLSM, a fluorophore molecule is thus excited with much longer wavelengths leading to higher tissue penetration as less light is scattered. Still, the excited state of the fluorophores is the same in single

photon and two-photon excitation, but because of the Planck relation equation (E = hv), the energy required to excite a fluorophore at a longer wavelength is nearly halved. As the probability of having a two-photon event is low, a temporal compression of the emission of the photons is necessary. A femtosecond pulsed laser and an objective for beam focusing ensure a high temporal and spatial compression, respectively. Thus, the excited volume is restricted to a 1 μm^3 and leads to a photon density approximately one million times higher than that required to generate the same number of one-photon excitation. Due to the physical properties of pulsed lasers and near-infrared wavelengths, 2PLSM (Denk et al., 1990) offers several advantages. The use of longer wavelengths reduces light scattering in the biological tissue resulting in reduced photodamage and phototoxicity in general. The inevitable damages produced when using a laser scanning technique stay confined to the excited volume where two-photon events take place while the focal planes above and below stay protected from photobleaching. Minimizing photobleaching and phototoxicity is especially vital for dynamic imaging. Indeed, each excitable molecule has its proper number of absorption-emission cycles. Once the limit of cycles is reached (10'000-40'000 cycles depending on the dye), the molecule cannot be further excited which leads to loss of fluorescence. Furthermore, scanning a biological sample means that the tissue is 'bombarded' with photons, which might lead to heating or unfavorable production of free radicals, which has a cost regarding tissue health. This phototoxicity depends mainly on the energy level of the excitation light, the duration of light exposure as well as the concentration of the fluorescent dye. Overall, 2PLSM allows for imaging five-fold deeper (up to 1 mm in the cortex of the mouse) into the tissue than single photon microscopy. All these advantages make 2PLSM the technique of choice for functional studies in living brain tissue.

1.10 Aims of the thesis

The question I set out to answer is: Are small CNS synapses capable of releasing multiple vesicles simultaneously upon single AP propagation? To answer it, I needed a tool to directly monitor synaptic release at single synapses. To do so, I introduced a new strategy to investigate presynaptic function, using the genetically encoded glutamate sensor iGluSnFR (Hires et al., 2008; Marvin et al., 2013) to measure glutamate transients in the synaptic cleft. As iGluSnFR is a novel tool, I first had to optimize imaging conditions and tools for data analysis. I successfully could show that under high p_r conditions the amount of glutamate release in response to a single AP is increased. Next, I aimed at a direct way to quantify the quantal parameters defining synaptic efficacy namely n, the number of readily releasable vesicles, p_{ves}, the vesicular release probability and the presynaptic quantum, q, corresponding to the filling of a single vesicle. To this end, I had to ensure that I was monitoring vesicular release from a single AZ and that the probe is sensitive enough to detect the release of a SV.

In a second part, I wanted to investigate how AMPARs report the release of glutamate during conditions of short-term plasticity such as high-frequency activity. Therefore, I used an ultrafast genetically encoded glutamate sensor, $iGlu_u$, which allowed me to image glutamate clearance and synaptic depression during 100 Hz spike trains. By combining cleft glutamate imaging and postsynaptic recording, I could separate pre- and postsynaptic sites of plasticity during a stimulation train.

2 Experimental Methods

In this section are the methods for all experimental procedures complementing the methods in the publication.

All experiments were in done in accordance with local regulations in Germany.

2.1 Organotypic hippocampal slice cultures

Organotypic hippocampal slices were prepared from Wistar rats at P4-5 as described previously (Gee et al., 2017). Briefly, newborn rats were anesthesized with CO_2 and decapitated. Brains were removed and kept in the ice cold dissection medium containing 1 mM $CaCl_2$, 5 mM $MgCl_2$, 10 mM D-Glucose, 4 mM KCl, 26 mM $NaHCO_3$, 0.001% Phenol red and 2 mM kynurenic acid. Dissected hippocampi were cut into 400 µm slices under a stereomicroscope with a tissue chopper and placed on a porous membrane (Millicell CM, Millipore). Cultures were maintained at 37°C, in a 95% O_2 and 5% CO_2 atmosphere in a medium containing 80% MEM (Sigma M7278), 20% heat-inactivated horse serum (Sigma H1138) supplemented with 1 mM L-glutamine, 0.00125% ascorbic acid, 0.01 mg/ml insulin, 1.44 mM $CaCl_2$, 2 mM $MgSO_4$, 13 mM D-glucose. No antibiotics were added to the culture medium. The fresh and pre-warmed medium was replaced twice per week.

2.2 Plasmids and single-cell electroporation

iGluSnFR, a gift from Loren Looger (Addgene plasmid #41732), and tdimer2, a gift from Roger Y. Tsien were each subcloned into an expression vector (pCI) under the control of the human synapsin1 promoter. Plasmids were diluted to 20 ng/µl and 40 ng/µl for tdimer2 and iGluSnFR, respectively, in K-gluconate-based solution consisting of (in mM): 135 K-gluconate, 4 $MgCl_2$, 4 Na_2-ATP, 0.4 Na-GTP, 10 Na_2-phosphocreatine, 3 ascorbate and 10

Hepes (pH 7.2). Thin-wall glass pipettes with a resistance of 12-14 MΩ were filled with a K-gluconate based solution (see Solution and electrophysiology) containing the mixture of the two plasmids. For DNA electroporation into individual cells, a train of negative voltage steps was applied once the pipette containing the plasmid mix was touching the membrane of the target cell. For the electroporation procedure, slice cultures were transferred to a microscope placed under a sterile air flow fan. Slice cultures were kept in (mM): 145 NaCl, 10 HEPES, 25 D-glucose, 1 $MgCl_2$ and 2 $CaCl_2$ (pH 7.4, sterile filtered). An Axoporator 800A (Molecular Devices) was used to deliver 50 voltage pulses (-12 V, 0.5 ms) at 50 Hz (Wiegert et al., 2017).

2.3 Solution and electrophysiology

Experiments were performed between DIV 22-27 (2-4 days after electroporation). Hippocampal slice cultures were placed in the recording chamber of the microscope and superfused with artificial cerebrospinal fluid (ACSF) containing (in mM): 127 NaCl, 25 $NaHCO_3$, 25 D-glucose, 1.25 NaH_2PO_4, 2.5 KCl, 2 $CaCl_2$, 1 $MgCl_2$. ACSF was saturated with 95% O_2 and 5% CO_2. In the experiments where $[Ca^{2+}]_e$ was changed, I switched from 1 mM Ca^{2+}, 4 mM Mg^{2+} to 4 mM Ca^{2+}, 1 mM Mg^{2+} to keep the divalent ion concentration constant. Patch pipettes with a tip resistance of 3.5 to 4.5 MΩ were filled with (in mM): 135 K-gluconate, 4 MgCl, 4 Na_2-ATP, 0.4 Na-GTP, 10 Na_2-phosphocreatine, 3 ascorbate and 10 HEPES (pH 7.2). Experiments were performed at 33 ± 1°C by controlling the temperature of the ACSF with an in-line heating system and of the oil immersion condenser with a Peltier element. Whole-cell recordings from a transfected CA3 pyramidal neurons were made with a Multiclamp 700B amplifier (Molecular Devices) under the control of Ephus software written in Matlab (Suter et al., 2010). To induce glutamate release, CA3 neurons were held in current clamp and stimulated through the patch pipette by brief electrical pulses (2-3 ms, 1.5-3.5 nA)

to induce single action potentials. Individual trials (single pulse or paired-pulse) were delivered at a frequency of 0.1 Hz. The analog signals were filtered at 6 kHz and digitized at 10 kHz. For dual patch experiments, CA1 neurons were recorded in voltage clamp. Access resistance (R_{acc}) was monitored continuously throughout the experiment and recordings with R_{acc} > 20 MΩ were discarded. To isolate AMPA receptor responses, CPP-ene (10 μM) was added to the ACSF.

2.4 Two-photon microscopy

The custom-built two-photon imaging setup was based on an Olympus BX51WI microscope controlled by a customized version of the open-source software package ScanImage (Pologruto et al., 2003) written in MATLAB (MathWorks). I used a pulsed Ti:Sapphire laser (MaiTai DeepSee, Spectra Physics) tuned to 980 nm to simultaneously excite both the cytoplasmic tdimer2 and the membrane bound iGluSnFR. Red and green fluorescence was detected through the objective (LUMPLFLN 60XW, 60x, 1.0 NA, Olympus) and through the oil immersion condenser (1.4 NA, Olympus) using 2 pairs of photomultiplier tubes (PMTs, H7422P-40SEL, Hamamatsu). 560 DXCR dichroic mirrors and 525/50 and 607/70 emission filters (Chroma Technology) were used to separate green and red fluorescence. Excitation light was blocked by short-pass filters (ET700SP-2P, Chroma). ScanImage was modified to allow arbitrary line scanning. To measure iGluSnFR signals with a high signal-to-noise ratio, spiral scans (see section 2.6 and Figure 6g) were acquired to sample the surface of individual boutons while electrically stimulating glutamate release. For single pulse stimulation, I acquired 44 spiral lines at 500 Hz. For paired-pulse pulse stimulation (48 ms ISI), I acquired 64 spiral lines at 500 Hz. Photomultiplier dark noise was measured before shutter opening and subtracted for every trial.

For frame scans (see section 2.7 and Figure 9a) I acquired frame scans of 32 by 32 pixels at a frame rate of 62.5 Hz (16 ms per frame) imaging a total of 14 frames per trial.

2.5 Drift Correction

To compensate for movements of the tissue during long imaging sessions, Christian Schulze developed an automated drift correction procedure to re-center the synapse of interest. As spatial reference, I obtained a series of optical sections (z-step size: 0.5 µm) that were interpolated to 0.25 µm. For drift correction, I acquired a single frame-scan (test image) and performed subpixel image registration against the stack of reference images to extract lateral drift. In a second step, the overlapping regions from both the test image and reference images were compared via cross correlation to reveal axial drift. Drift was compensated by adding offsets to the xy-scanner command voltages and by moving the objective to the correct z-position. Drift correction was typically completed within 0.3 s and performed before each stimulation trial.

2.6 Analysis of fluorescence transients

In case of a release event (‘success’), a spiral scan covering the entire bouton may hit the iGluSnFR molecules activated by the diffusing cloud of glutamate just once or several times per line. I had no prior knowledge about the precise location of fusion events on the bouton surface. To maximize the signal-to-noise ratio in every trial, I assigned a dynamic region of interest (ROI): Pixel columns (i.e. spatial positions) were sorted according to the change in fluorescence (ΔF) in each column. In ‘success’ trials (average $\Delta F > 2\sigma$ above baseline noise), only columns which displayed a clear change in fluorescence ($\Delta F >$ ½ max

(Δ*F*)) were evaluated. In 'failure' trials (when ∆F of each column of the ROI was 5%> than ∆F of the corresponding columns in the baseline), the columns selected in the last 'success' trial were evaluated. I would like to point out that the classification used for ROI positioning (success vs. failure) was preliminary. Indeed, some 'failure' trials did show small fluorescent transients in the more sensitive ROI-based analysis. Boutons with a full width at half maximum (FWHM) of the amplitude distribution of the baseline (i.e. non-stimulated trials) larger than 0.4 were rejected as the imaging conditions were considered non optimal and not considered for further analysis. To correct for bleaching, I fit an exponential decay to F_0 in 'failure' trials. I corrected all data for bleaching by subtracting monoexponential fits acquired from the average fluorescence time course of failures. This bleach time constant was used to establish a photobleaching correction for each trial. To measure the amplitude iGluSnFR changes in fluorescence and to distinguish successful release of glutamate from failures, I used a template-based fitting algorithm. For each bouton I extracted a characteristic decay time constant by fitting a mono-exponential function to the average bleach-corrected iGluSnFR signals. To estimate the glutamate transient amplitude for every trial I kept the amplitude as the only free parameter and thereby extracted the peak amplitude of individual iGluSnFR signals (Figure 21). Occasionally very bright structures traveling through the cytoplasm passed through the bouton during a trial. I therefore measured the mean G_0 (Baseline iGluSnFR signal) and calculated G_0/R_0 (ratio between baseline iGluSnFR signal and the baseline tdimer2 signal) in each trial. If $G_0 > 2\sigma$ above mean G_0 of all trials and $G_0/R_0 > 2\sigma$ above mean G_0/R_0 of all trials from that single bouton, then that trial was removed from the analysis.

2.7 Localization of center of release

To map the position of fusion events on a bouton, I acquired 15 images (16×16 pixel) at a rate of 62.5 Hz (16 ms per frame). Analysis of data consisted of four steps: de-noising, image alignment, estimating the amplitude of fluorescence transients, and localization of the release site. Raw images were first treated by a wavelet method to reduce photon shot noise (Luisier et al., 2010). The method has been shown to improve signal/noise ratio in two-photon experiments (Tigaret et al., 2013). Next, a cross talk correction was applied and the images were smoothed using a low pass filter (Gaussian kernel, 5×5 field size, σ = 1 pixel). Images were then up-sampled to 128×128 pixels (Lanczos3 kernel). For image alignment, a Fast Fourier transform (FFT) was performed on the red fluorescence signal (tdimer2). In addition, the red channel was used to define a continuous area encompassing bouton and axon (pixel intensity ≥ 10% to 30% maximal intensity) as a morphology mask. The relative change in iGluSnFR fluorescence ($\Delta F/F_0$) was calculated pixel by pixel where F_0 is the mean of 5 baseline frames. The top 3% pixel values within the bouton mask were averaged to obtain the peak amplitude. Trials where baseline fluorescence was very uneven (cross correlation ≤ 0.9), such as when a green fluorescent particle passed through the bouton of interest were excluded from further analysis.

To localize the fusion site, a template (2-D anisotropic Gaussian kernel) was constructed from the average of 5 ‘success’ trials. In the first round of analysis, I fit the template to every single frame by adapting only the amplitude, keeping the location and shape of the kernel fixed at the template values. In trials where the release site is not exactly at the template position, the amplitude will be underestimated in this step. The goal of this first pass analysis was a preliminary classification of ‘successes’ ($\Delta F/F_0 > 2\sigma$ of baseline noise) and ‘failures’ ($\Delta F/F_0 < 2\sigma$ of baseline noise). To localize the fusion site in each individual trial, the fitting procedure was repeated, this time allowing for variable location. The location of the best fit

corresponded to the most likely fusion site. This analysis was applied to all success trials, and a probability density function (2D Gaussian) was fitted to estimate the size of the active zone on the bouton. The same localization procedure was applied to the failure trials and, as a control, to the frame before stimulation. In most experiments, the failure trials and pre-stimulation frames produced random localizations, suggesting that the 2σ criterion was suitable to distinguish successes from failures. In cases where the positions of apparent 'failures' clustered in a second area of the bouton, I classified this bouton as a 'multi-synapse bouton' (Figure 10) and excluded it from further analysis.

To estimate the precision of the localization procedure, I imaged carboxylate-modified yellow-green fluorescent microbeads (0.17 μm diameter) positioned next to red fluorescent boutons and used the localization procedure described above to determine bead position relative to the bouton. As expected, localization precision was a function of the number of photons detected from the bead. At low laser power, I matched the bead intensity to the typical signal amplitude of iGluSnFR during the release of a single vesicle. Under these conditions, bead localization precision was 0.05 ± 0.01 μm.

2.8 Synapse modeling and glutamate release simulation

Release of glutamate and the time profile of iGluSnFR fluorescence were simulated using a Monte Carlo method (MCell) that takes into account the stochastic nature of molecule diffusion as well as that of reaction between molecules (Stiles et al., 1996; Franks et al., 2003). The model consisted of an axon (diameter 0.2 μm, length 3 μm) with a varicosity representing the bouton (diameter 0.5 μm, length 0.5 μm), a hemispheric structure representing the spine (diameter 0.4 μm) attached to a cylindrical spine neck (diameter 0.2 μm). Active zone and postsynaptic density were defined as circular areas (diameter 300 nm) separated by the synaptic cleft (20 nm) (Mishchenko et al., 2010). Axon and spine were

enclosed by an astrocytic compartment (width of extracellular space: 20 nm). Boundary conditions for the entire system were reflective. Glutamate transporters (GluT) were placed on astrocytic membranes at a density of 10,000 μm^{-2}. AMPA receptors were restricted to the PSD at a density of 1,200 μm^{-2} (resulting in ~85 receptors for a PSD diameter of 300 nm). Vesicle fusion was modeled by an instantaneous injection of glutamate at a fixed position (center of the active zone). The glutamate content of a single vesicle was estimated to be in the range of 2,000-3,000 (Rusakov et al., 2011). In order to study the consequences of univesicular and multivesicular release, the number of released glutamate molecules was varied between 3000 and 30000 (1-10 vesicles). The kinetic model for activation of AMPARs by glutamate was based on a well-established model (Jonas et al., 1993). Originally, the model from Jonas et al., 1993 was developed to narrow the amount of quantal variability due to channel gating. The model was supposed to predict the current responses of outside-out patches for fast glutamate application. Those current responses of fast glutamate application have been measured in excised patches from granule cells of dentate gyrus and pyramidal cells of CA3 and CA1 regions of P14 to P22 rats at room temperature (20-24°C) (Colquhoun et al., 1992; Jonas and Sakmann, 2012). The open probability of AMPARs has been measured by application of 3 mM glutamate in (Jonas et al., 1993). Fast desensitization kinetics (~ 1 ms) of the channel are assumed as measured in the Crayfish muscle (Dudel et al., 1990). This model is representative of AMPARs containing GluA1 and GluA2 subunits consistent with the structure of AMPARs at CA3-CA1 synapses (Lu et al., 2009). Kinetics of glutamate transporters and glutamate diffusion were adopted from (Bartol et al., 2015). For the simulation, the rates were adjusted to 34°C to match the temperature used in my two-photon microscopy experiments. The model of iGluSnFR is based on a two-step reaction where rapid binding of glutamate to iGluSnFR is followed by a slower conformational change with concomitant increase in fluorescence. The kinetics for step 2 is different for purified protein vs. cell-based measurements (Marvin et al., 2013). iGluSnFR fluorescence time

profiles following vesicle release at a functional bouton were therefore measured by parking the imaging laser beam at a fixed position. The rise time of the $\Delta F/F_0$ profile was fitted to a model in which two consecutive first-order reactions are linked:

$$\text{glu-iGluSnFR}_{dim} \rightarrow \text{glu-iGluSnFR*}_{dim} \leftrightarrow \text{glu-iGluSnFR'}_{bright}$$

The high diffusion constant of glutamate has led to a drop of glutamate concentration at the release site and no new glu-iGluSnFR*$_{dim}$ can be formed: the first reaction is therefore irreversible. Hereby, values obtained are k_{+2} of 2.48 x 10^3 $M^{-1}s^{-1}$ and k_{-2} of 111 s^{-1} for the second step of this reaction corresponding to the conformational change of the glutamate bound iGluSnFR from dim to bright state and vice versa. Dissociation constants 85 µM and 13 µM have been determined from measurements using isolated protein and in cells, respectively. The difference may be attributable to a slightly altered steric situation for iGluSnFR when attached to a cell membrane.

2.9 Quantal analysis

I performed quantal analysis on single boutons using the iGluSnFR signals to determine the number of vesicles (n), the vesicular release probability (p_{ves}) and the size of a quantum (q).

A binomial model was used to find combinations of n and p_{ves} that provided a good fit to the experimental data. An important source of noise is the collection of photons (green fluorescence) which follows Poisson statistics ('shot noise'). For each bouton, I analyzed the standard deviation in frames without stimulation ('no stim frames'). The width of the success distribution was determined by the expected photon shot noise (calculated from the baseline noise) additional broadening due to variable glutamate content in individual vesicles. As the iGluSnFR saturates at a $\Delta F/F_0$ of 440%, the data was first uncompressed (linearization of

the hyperbolic dependence Langmuir isotherm r = [A]/(K_d +[A]) where r corresponds to the fractional occupancy (mole of ligand/mole of macromolecule) and [A] stands for the concentration of free ligand and K_d of iGluSnFR is being used. With a custom code written in Matlab I then find through an exhaustive search the probability density function. For the exhaustive search, I allowed searching for different combination of the number of vesicles ranging from 1-20, a vesicular release probability (p_{ves}) ranging from 0.01 to 1, a quantal size from 20% to 140% $\Delta F/F_0$. For fitting the dataset under the UVR assumption, n was fixed to 1 but the variability of vesicle size or glutamate content was allowed, CV ranging from 0.2 to 2. The two fitting procedures, namely UVR and MVR assumption were the result of an exhaustive search through 3 free parameters. The amplitude and location of the success distribution were free parameters. The quality of the model was assessed by calculating the root-mean-square (RMS) between the histogram and the corresponding positions of the best fitting probability density function.

The prediction with the smallest number of vesicles that was within 1% of the minimum mean square error was selected. This resulting fitting probability function was compressed to compensate for the iGluSnFR saturation.

2.10 Statistical Analysis

Data are reported as mean ± SEM unless indicated otherwise. Normality was tested using the D'Agostino-Pearson omnibus normality test. To test for significant differences between population means, Paired t test or the nonparametric Wilcoxon-Signed rank test were used. For independent population I used unpaired t-test or the nonparametric Mann–Whitney test as appropriate. Statistical significance was assumed when $p<0.05$. Symbols used for assigning significance in figures: not significant (n.s.), $p>0.05$; significant, $p <$

0.05(*), $p < 0.01$(**), and $p < 0.001$(***). All statistics were generated with Graph Pad Prism software.

3 Results

3.1 Expression of the glutamate sensor

I performed single-cell electroporation under sterile conditions to transfect individual CA3 pyramidal neurons in organotypic slices of rat hippocampus with iGluSnFR and the red fluorescent protein tdimer2 (Figure 6a). Two to four days after transfection, I transferred the cultures to the recording chamber of a two-photon microscope (Figure 6b). As iGluSnFR is very dim in the absence of glutamate, I used the red cytoplasmic fluorescence to visualize soma, axons and boutons of transfected CA3 pyramidal cells. Transfected cells (Figure 6c) were patch-clamped under visual control, switching between epifluorescence and Dodt contrast. Maintaining whole-cell access, the stage was moved to position CA1 under the 60x 1.0 NA objective (Figure 6d). While imaging boutons in *stratum radiatum*, I triggered propagating action potentials (APs) by brief somatic current injections (Figure 6e). Boutons belonging to the patched CA3 neuron were easily identified by a rapid increase in iGluSnFR green fluorescence 4.5 ± 1.6 ms (mean ± SD) after somatic current injection (Figure 6f). Recording temperature was maintained at 34 ± 1°C by Peltier-heating the oil immersion condenser that was used to collect trans-fluorescence and heating the perfusion in flow. The fast rise and decay kinetics of iGluSnFR (Marvin et al., 2013) made it rare to capture the peak of iGluSnFR fluorescence transients using the relatively slow frame scanning mode. Straight line scans across an individual bouton provide much better temporal resolution (500 – 1000 Hz), but are extremely sensitive to mechanical drift of the tissue: If the scan line misses the center of the rapidly diffusing cloud of glutamate, the true amplitude of individual release events will be underestimated. To capture the peak of the iGluSnFR signal, which is extremely confined in space and time, Christian Schulze modified the ScanImage software (Pologruto et al., 2003) to allow user-defined spiral scans

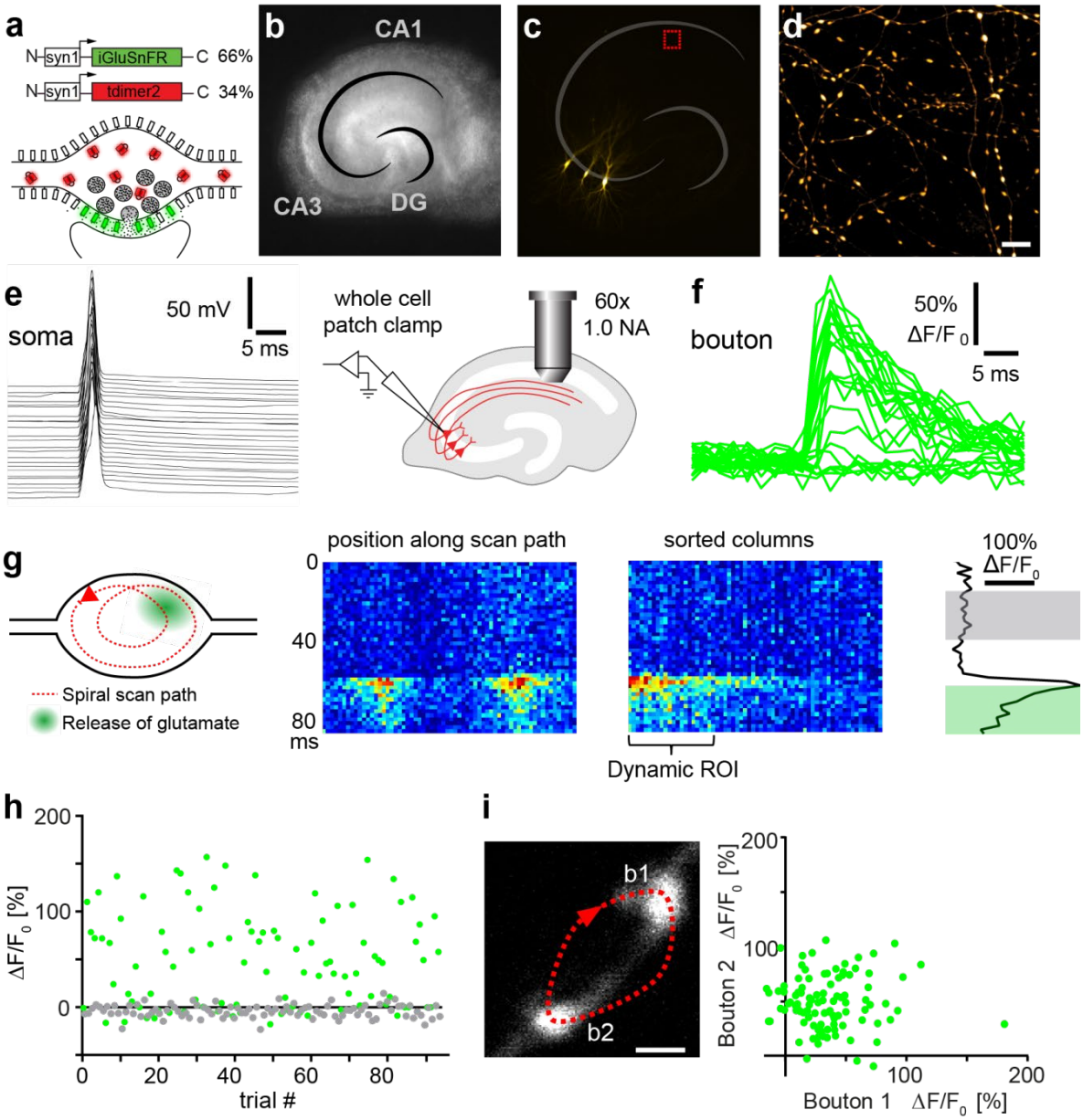

Figure 6: iGluSnFR expression in CA3 pyramidal cells in organotypic slice culture of rat hippocampus

Co-expression of two plasmids in individual CA3 pyramidal cells. The red fluorescent protein tdimer2 labels the axoplasm while membrane-anchored iGluSnFR is exposed to the extracellular space. **b)** Transmitted light image of transfected organotypic culture. **c)** Fluorescence image shows three transfected CA3 neurons. Area for synaptic imaging is indicated (dotted box). **d)** Two-photon image stack (maximum intensity projection) of CA3 axons in CA1 stratum radiatum. **e)** Action potentials were elicited in a transfected neuron by somatic current injections. **f)** Simultaneous optical recording (iGluSnFR fluorescence) from a single Schaffer collateral bouton in CA1, showing a broad distribution of amplitudes and occasional failures. **g)** For optimal glutamate detection regardless of the location of a fusion event, a 500 Hz spiral scan pattern was employed to sample the entire surface of a

bouton. Fluorescence intensity (single trial) coded in pseudocolors. At t=58 ms, a glutamate release event occured and was sampled twice during every spiral scan. To compensate for minor drift between trials, only columns with ΔF > ½ max (ΔF) were analyzed (dynamic region-of-interest). If no response was detected, the columns selected in the last success trial were analyzed. Response amplitude was estimated by exponential fit (green area, response) normalized by the resting fluorescence of the bouton (gray area, baseline). **h)** Response amplitude (green markers) was constant over time. A time window before stimulation was analyzed to estimate imaging noise (gray markers). **i)** Fluorescence transients in neighboring boutons were not correlated, excluding action potential propagation failure as a cause for variable iGluSnFR signals. Scale bar represents 1 µm.

at 500 Hz, thus sampling the entire surface of the bouton every two milliseconds (Figure 6g). Without knowing the exact location of the fusion site *a priori*, I was sure to cross it several times in every spiral scan. Christian Schulze developed an automatic 3D repositioning routine was developed to compensate for slow drift of the tissue, allowing for stable optical recordings over hundreds of trials. To compensate for small amounts of drift between stimulations, I did not use a static region of interest (ROI), but sorted the 'pixel columns' (spatial positions) by the change in fluorescence (dynamic ROI). If no clear stimulus-evoked change in fluorescence was detected (e.g. presumably a failure trial), the same column order was used as in the previous trial. To extract the amplitude of individual trials, I constructed a template (exponential decay) from a number of manually selected large responses for individual boutons. A single parameter (amplitude) was fit to match the template to each individual trial. To define a detection threshold for every experiment, I fit the response template to a time window before stimulation (baseline, gray markers in (Figure 6h) where no release events occurred. Responses that exceeded 2σ the baseline noise were classified as 'successes'. Occasionally, I observed green fluorescent particles moving through the axon. These were detected by an elevated green/red ratio at baseline and excluded from further analysis (~ 1% of trials). At most boutons, the failure rate was stable over the time of the experiment (Figure 6h). Failure of glutamate release could be due to the stochastic nature of vesicle release. In simultaneously imaged neighboring boutons, failures were not

correlated, arguing for randomness generated inside individual boutons rather than being due to action potential propagation failure into individual branches of the extensive network of axon collaterals (Figure 6i). I next asked whether the release probability between two neighbouring boutons located on the same axon is more similar than two boutons from different axons from different cells. I therefore monitored iGluSnFR signals in response to a single action potential for ~100 trials in 2 neighbouring boutons, consecutively. I then determined the release probability and the average iGluSnFR signal given a success (Figure 7a,b) as described in the method (section 2.6). The ∆Pr of two neighbouring boutons (red vertical line) is more similar than expected from the difference of the average release probability of two boutons randomly paired (distribution of $|p_r$ BX-p_r BY|, X and Y being boutons from the dataset used to measure the experimental ∆Pr) (Figure 7c,d). On the other hand, the amplitude of the iGluSnFR signal given a success of a bouton (B1) and its neighbour on the same axon (B2) are not more similar than expected by chance (Figure 7e,f). This finding is in accordance with data from hippocampal primary cultures where the CV of the release probability is lower for boutons belonging to the same axon than boutons from different axons and cells (Ariel et al., 2013).

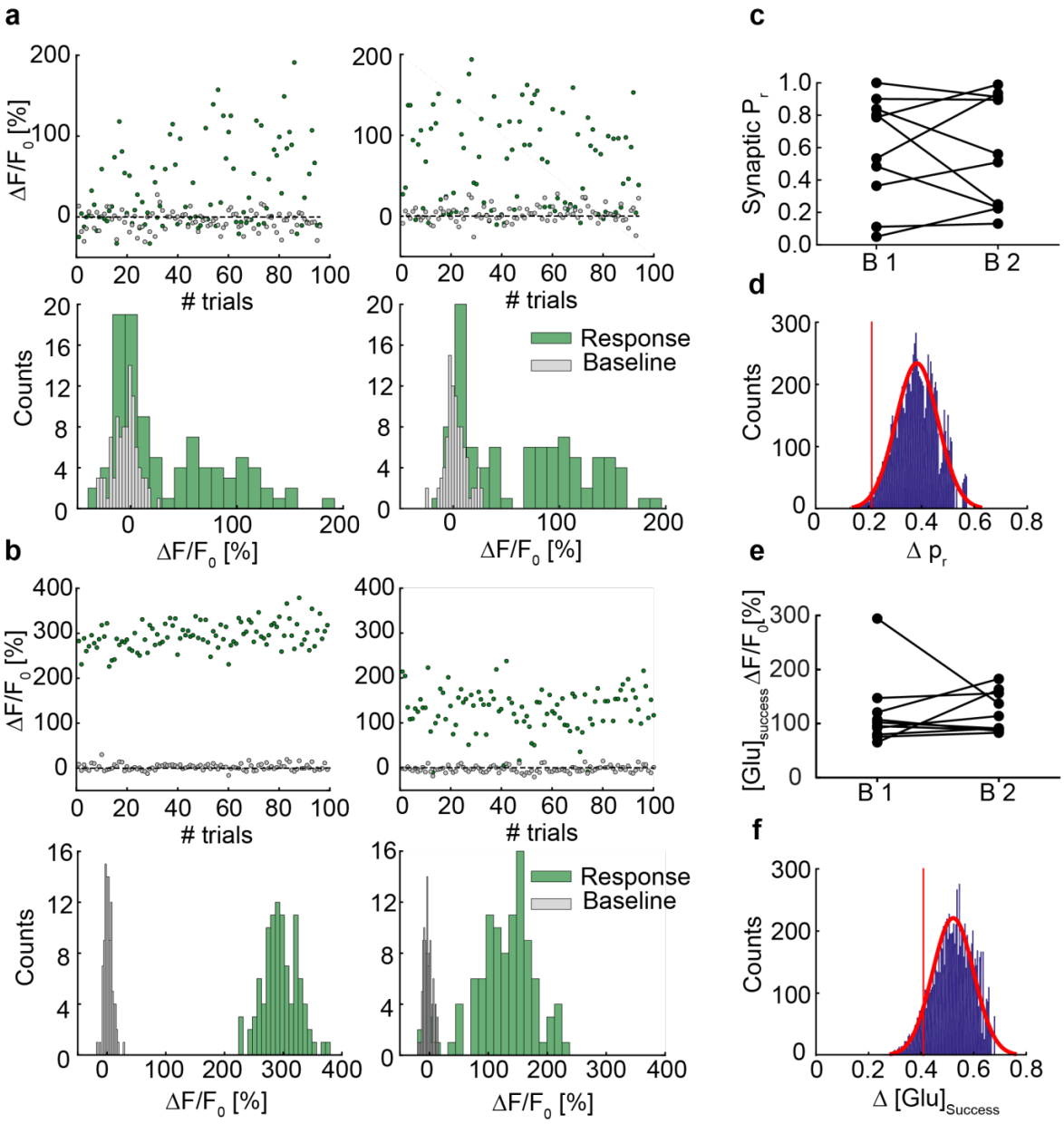

Figure 7: Release statistics of neighbouring boutons on the same axon

a) Glutamate transients (green dots) and baseline fluorescence (grey dots) of two neighbouring boutons measured in ACSF containing 2 mM Ca^{2+} and 1 mM Mg^{2+} located on the same axon (upper panels) and their corresponding histogram counts (lower panel). **b**) Glutamate transients (green dots) and baseline fluorescence (grey dots) of two neighbouring boutons located on the same axon (upper panels) and their corresponding histograms (lower panel) measured in ACSF containing 2 mM Ca^{2+} and 1 mM Mg^{2+} **c)** Synaptic release probability (calculated out of ~ 100 trials) of individual boutons (B1) and their neighbourg bouton on the same axon (B2); n=10 **d)** Histogram of $\Delta\ p_r = |p_r\,\mathrm{BX}\text{-}p_r\,\mathrm{BY}|$. BX and BY are

randomly paired from the dataset in (c). $|\Delta p_r$B2-Δp_rB1$|$ (red vertical line) is significantly more similar than mean Δp_r of two boutons paired randomly from the same dataset; (p-value: 0.0148) **e)** Amplitude of the iGluSnFR signal given a success of a bouton B1 and its neighbourg on the same axon (B2); n=10 **f)** Histogram count of the difference between the average $\Delta F/F_0$ of successes only of two random neighbouring boutons. The difference of the average $\Delta F/F_0$ of successes from two neighbouring boutons (red vertical line) is not more similar than the randomly connected pairs of boutons.

3.2 Modulating synaptic release probability affects cleft glutamate concentration

Most likely, the stochastic nature of iGluSnFR signals is caused by the unreliable vesicle fusion machinery. Since presynaptic vesicle fusion is Ca^{2+}-dependent (Katz, 1951), I expected a steep dependence of the synaptic release probability p_{syn} on the extracellular Ca^{2+} concentration, $[Ca^{2+}]_e$. Indeed, switching $[Ca^{2+}]_e$ from 1 mM to 4 mM dramatically increased p_{syn} from 0.17 ± 0.04 to 0.87 ± 0.07 (Figure 8a and 8b, n = 11 boutons) (Wilcoxon signed rank test: p<0.001). 4 out of 11 boutons reached the ceiling of p_{syn} = 1 in 4 mM $[Ca^{2+}]_e$. Interestingly, the amplitude of iGluSnFR signals increased as well. I evaluated only responses that were classified as successes (filled black markers in Figure 8) and found a significant increase in amplitude from 97% ± 7% $\Delta F/F_0$ to 174% ± 15% $\Delta F/F_0$; paired t- test, p<0.0001 (Figure 8b, n = 11 boutons), indicating higher glutamate concentrations in the synaptic cleft under high p_{syn} conditions. In low $[Ca^{2+}]_e$, success amplitudes (ranging from 51% to 132% $\Delta F/F_0$) were similar across boutons and there was no correlation with p_{syn} (Figure 8c). In high $[Ca^{2+}]_e$, on the other hand, the same set of boutons had more variable success amplitudes (ranging from 77% to 230% $\Delta F/F_0$) that were strongly correlated with p_{syn}. To further explore the non-linear relationship between p_{syn} and cleft glutamate concentrations, I performed a set of experiments in 2 mM $[Ca^{2+}]_e$ which is often considered physiological (Figure 8d). Under these conditions, p_{syn} was highly variable between individual boutons. Again, low p_{syn} boutons produced consistent low success amplitudes (response

amplitude range from 76% to 95% $\Delta F/F_0$) while high p_{syn} boutons produced considerably larger successes with more variable amplitudes. A simple binomial model of release, allowing for different numbers of readily releasable vesicles (n) in individual boutons (Figure 8d, gray curves), provided a straightforward explanation for the non-linear relationship between p_{syn} and success amplitude on the population level: At low p_{syn} boutons, only a single vesicle is released, regardless of the number of readily releasable vesicles. High p_{syn} boutons frequently released 2 or more vesicles, generating fluorescence transients of larger amplitude that are more variable.

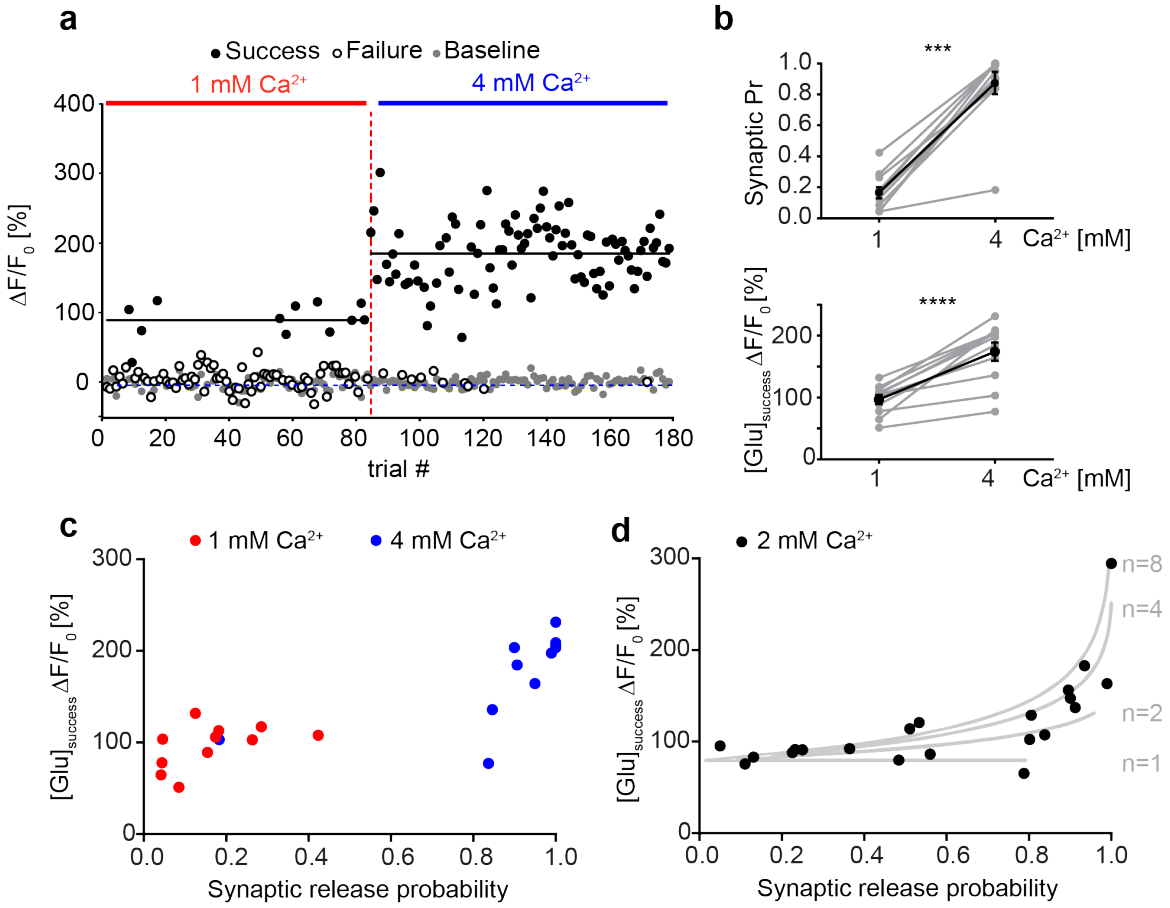

Figure 8: iGluSnFR signals depend on the extracellular Ca^{2+} concentration

a) Glutamate transients in a single bouton, switching from saline containing 1 mM Ca^{2+} to 4 mM Ca^{2+}. The black line represents the average of the amplitude of successes in each saline condition **b)** Summary of 11 boutons in low/high Ca^{2+}. The probability of successful glutamate release (upper panel) went from 0.17 ± 0.04 in 1 mM Ca^{2+} to 0.87 ± 0.07 in 4 mM Ca^{2+} (Wilcoxon signed rank test: $p<0.001$). The amplitude of fluorescence transients in trials classified as 'success' (lower panel) went from 97% ± 7% $\Delta F/F_0$ in 1 mM Ca^{2+} to 174 % ± 15% $\Delta F/F_0$ in 4 mM Ca^{2+} (paired t test: $p<0.0001$) indicating higher glutamate concentrations in the synaptic cleft under conditions of higher release probability. **c)** The probability of successes was correlated with the amplitude of success trials in a non-linear fashion. **d)** In 2 mM Ca^{2+}, the release probability of individual synapses ranged from 0.05 to 1. The amplitude of success trials was similar for boutons with low p_r, but rose steeply for $p_r > 0.8$. Simulations (gray curves) show that the data are consistent with a uniform quantal size (fluorescence transient caused by the fusion of a single vesicle, here 80% $\Delta F/F_0$), but variable p_{ves} and n (number of readily releasable vesicles, here 1, 2, 4, and 8).

3.3 Mapping the spatial location of individual fusion events

Large iGluSnFR signals from high p_{syn} boutons suggest multivesicular release, but are all vesicles released from a single active zone? To map the spatial location of individual release events (fusion site), I acquired rapid frame scans (16x16 pixels, 62.5 Hz) at high zoom (Figure 9a). The red (cytoplasmic) fluorescence was used to align all frames. I classified trials into 'successes' and 'failures' based on the standard deviation of green fluorescence before stimulation (2σ criterion). In principle, the site of vesicle fusion can be localized by finding the center of the iGluSnFR signal from frame scans of the boutons. Therefore, in success trials, the location of vesicle fusion could be located by fitting the iGluSnFR signals with a two-dimensional Gaussian kernel (Figure 9b). The success fusion events were typically localized to a small region of the boutons in low p_r conditions (Figure 9c, 1 mM Ca^{2+}). Under conditions of increased p_r (4 mM Ca^{2+}), fusion events localized to the same sub-region of the bouton (Figure 9d and Appendix: Response Localization). The same fitting procedure applied to failure trials resulted in a widely distributed locations (Figure 9e),

suggesting that the 2σ criterion correctly distinguished failures from successes. A similar distribution was observed when the frame before stimulation was analyzed (Figure 9f). The spatial distribution of fusion events was often elliptical, suggesting a synaptic contact on the side of the bouton (Figure 9g). The distribution of the localized fusion events was fitted with an ellipse including 95% of the responses. I assume that the long axis of the fusion site distribution represents the true diameter of the active zone whereas the short axis is the result of a geometrical projection of an active zone tilted with respect to the focal plane. To calibrate the localization method, I acquired series of images from a green fluorescent microspheres next to a bouton (Figure 9h), which resulted in more confined and circular maps (Figure 9i). From these bead measurements, which were matched to the photon count of iGluSnFR signals, I estimate the localization precision to be 0.05 ± 0.01 µm while the lateral resolution of the microscope is 0.48 ± 0.02 µm. In high Ca^{2+}, the same boutons displayed significantly more confined locations (Figure 9j). In high Ca^{2+}, when multiple vesicles fuse simultaneously, the glutamate cloud is not generated by a single 'point source' and I therefore localized the centroid of multiple fusion events. The distribution of centroids is expected to be less variable than the distribution of individual fusion events, explaining the tighter spatial distribution of iGluSnFR signals in high Ca^{2+}. Most importantly, the localization experiments confirmed that at the majority of boutons, iGluSnFR signals were generated by a single active zone of 0.29 to 0.98 µm diameter (mean long axis in 1mM Ca^{2+}: 0.56 ± 0.06 µm). In a few experiments, I observed what appears to be more than one active site on a single bouton (Figure 10). Such apparently multi-synapse boutons, which could also be identified in line scan mode (Figure 10b), were excluded from further analysis. Taken together, my measurements show that synaptic vesicles are released at positions within a confined area (single active zone). Whether vesicle release sites were further organized into discrete nanodomains within the active zone, as has been shown for synapses grown on

glass cover slips (Tang et al., 2016), could not be determined due to inevitable three-dimensional movement of intact brain tissue.

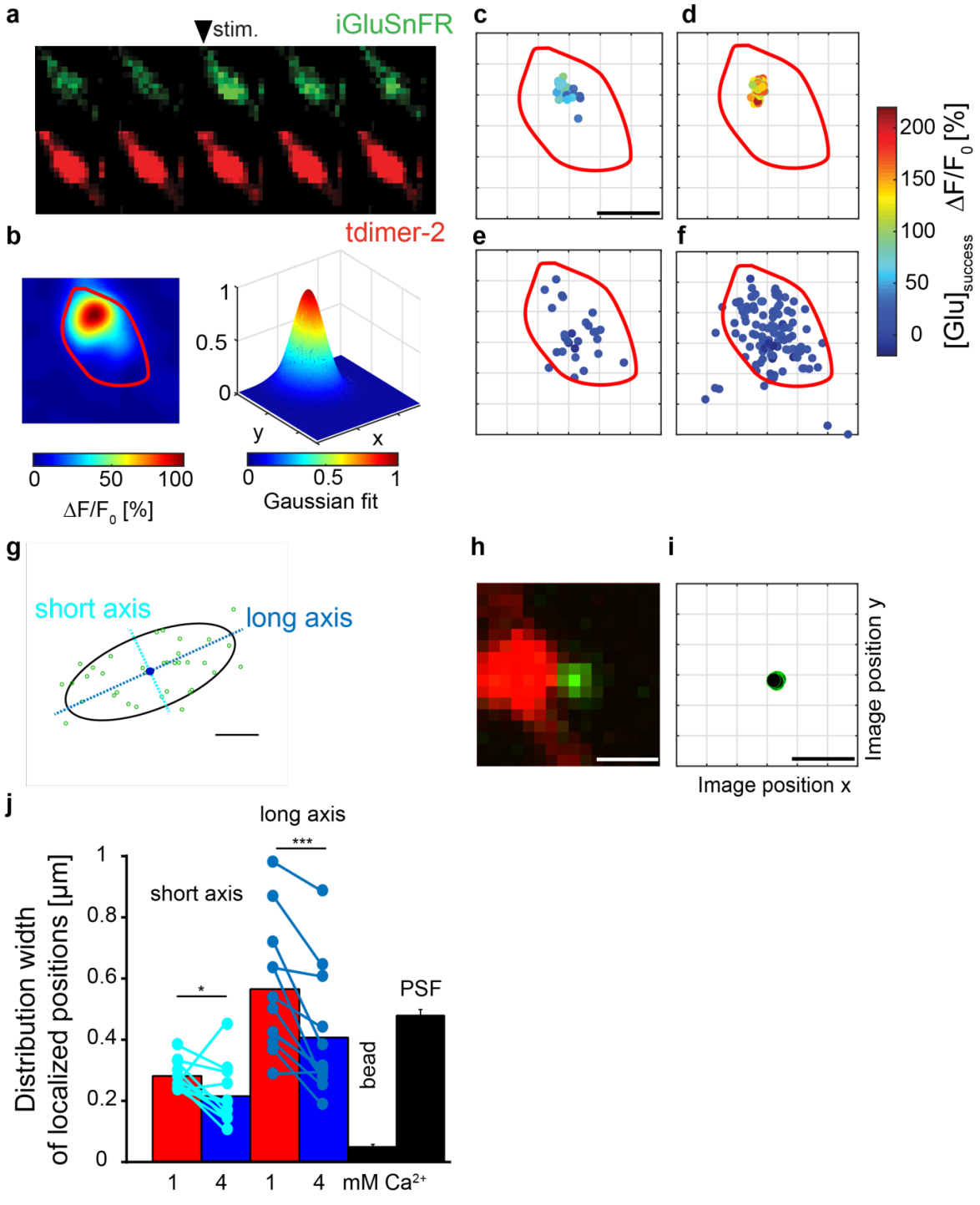

Figure 9: Localizing the fusion site

a) Time-lapse (62.5 Hz) of a bouton releasing glutamate upon action potential. **b)** Top view of average responses of signals classified as successes (left panel) and side view of the resulting 2D-Gaussian kernel fit **c)** Center positions of 2D-Gaussian kernel fits in success trials in ACSF containing 1 mM Ca^{2+}. The scale bar represents 1 µm. **d)** Center positions of 2D-Gaussian kernel fit in success trials in ACSF containing 4 mM Ca^{2+}. **e)** Center positions of 2D-Gaussian kernel fits in failure trials (below 2σ of the 'no pulse frame'). **f)** Center positions of 2D-Gaussian kernel fits in failure frames before the stimulation. **g)** Scheme of a fitted ellipse including 95% of localized successes from a single bouton. The length of the short and long axis of the fitted ellipse in 1 mM Ca^{2+} and 4 mM Ca^{2+} are used to test for a relative enlarging of the release area in 4 mM Ca^{2+} indicative of a multisynapse bouton. The scale bar represents 128 nm. **h)** Single plane of a two-photon microscope image of a bouton (tdimer2) next to a yellow-green fluorescent microsphere (0.17 µm). The scale bar represents 1 µm. **i)** Center positions of 2D-Gaussian kernel fits to the fluorescent signal of a yellow-green fluorescent microsphere. 50 consecutive images were acquired at 62.5 Hz. The scale bar represents 1 µm. **j)** Histogram of short/long axis of the fitted ellipse to the localized responses and FWHM distribution of the localized bead and PSF measurement. Success localization short axis, 0.28 ± 0.01 µm in 1 mM Ca^{2+} and 0.21 ± 0.03 µm in 4 mM Ca^{2+} ($p = 0.04$, Wilcoxon test) ; success localization long axis, 0.56 ± 0.06 µm in 1 mM Ca^{2+} and 0.41 ± 0.06 µm in 4 mM Ca^{2+} ($p = 0.001$, Wilcoxon test); bead localization 0.05 ± 0.01 µm; PSF bead, 0.48 ± 0.02 µm). Error bars indicate SEM.

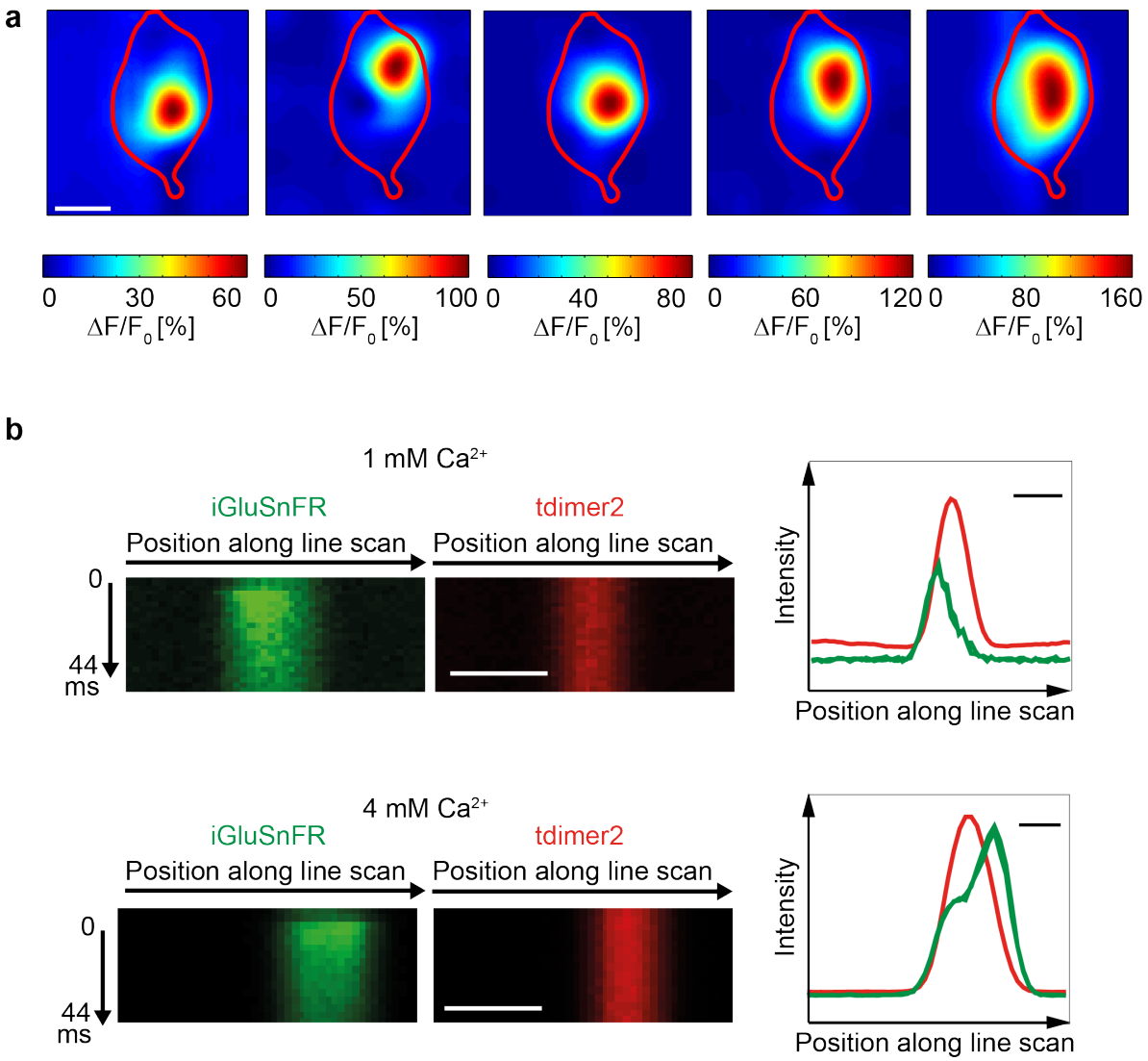

Figure 10: Examples of boutons with multiple active zones

a) Example of color-coded iGluSnFR signal of a multi-synapse bouton. Each frame represent the iGluSnFR signal in response to a single action potential. Scale bar represents 1 µm. **b)** Example of the average intensity profile of the scanning line across a multisynaptic bouton in 1 mM Ca^{2+} (upper panel) with a single hot spot and in 4 mM Ca^{2+} (lower panel) with the appearance of a second hot spot. All boutons with a similar pattern of release were excluded from further analysis. Scale bar represents 1 µm.

3.4 Desynchronized release events reveal quantal size

Although previous studies using postsynaptic measurements of AMPAR currents found evidence for multivesicular release at Schaffer collateral synapses (Tong and Jahr, 1994; Bolshakov et al., 1997; Oertner et al., 2002; Christie and Jahr, 2006; Minneci et al., 2006; Boucher et al., 2010) and in dissociated hippocampal cultures (Abenavoli et al., 2002; Watanabe et al., 2013b), it has not been possible to compare the amplitude of evoked responses to the amplitude of spontaneous fusion events ('minis') *at the same synapse*. To perform a classical quantal analysis, the size of the quantum (q) has to be known. I therefore replaced extracellular Ca^{2+} with Sr^{2+} to desynchronize vesicle fusion events (Fry, 1969) at single boutons. Sr^{2+} is known to lead to asynchronous release due to its slow clearance from the presynaptic terminal (Xu-Friedman and Regehr, 2000) and its low affinity for Ca^{2+} sensors like synaptotagmin-1 (Fernandez et al., 2002; Evans et al., 2015). As expected, large-amplitude glutamate release events occurred with high probability in 4 mM extracellular Ca^{2+} (Figure 11a, left panel). When ACSF containing 4 mM Ca^{2+} was slowly replaced by ACSF containing 4 mM Sr^{2+}, the glutamate transients started to decompose into smaller events of relatively uniform amplitude (Figure 11a, panels 2-3). When 4 mM Sr^{2+} was fully washed-in, evoked responses largely disappeared while baseline fluorescence became very noisy (Figure 11a, panel 4). The amplitude histogram shows clear separation between evoked responses (Figure 11b, c, green bars) and delayed events (blue bars). The quantal amplitude determined with this method was q = 96% ± 15% $\Delta F/F_0$ (n = 3 boutons).

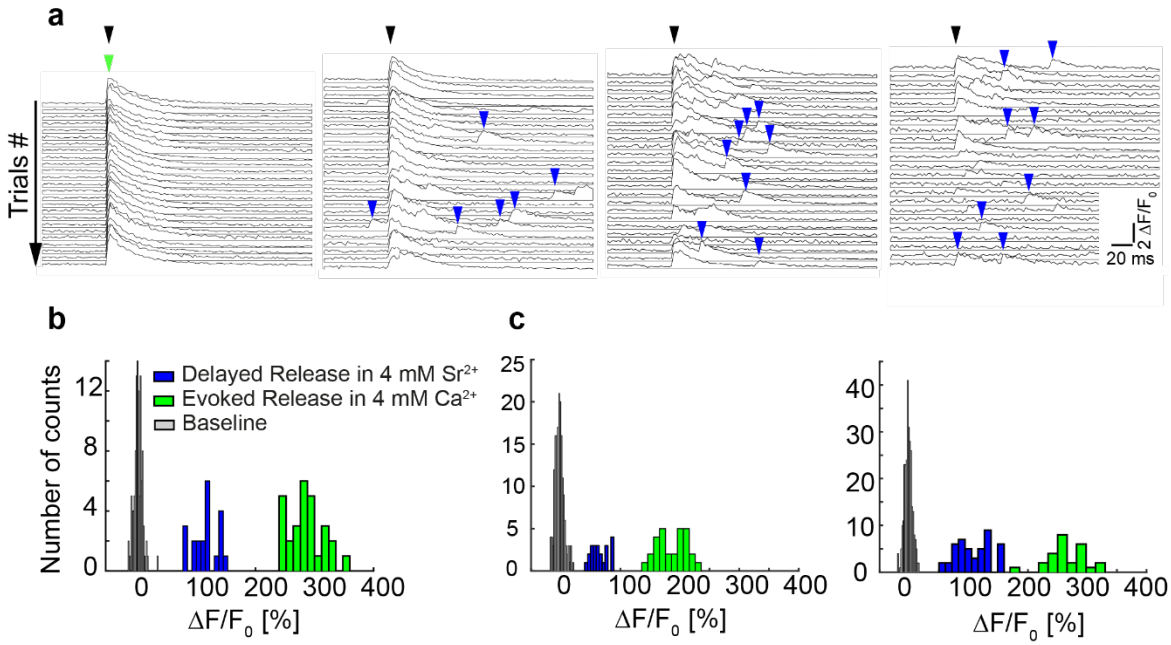

Figure 11: Desynchronized release events reveal quantal size

a) iGluSnFR changes in fluorescence (single bouton, 25 consecutive trials) in response to single action potentials (green arrowhead) in ACSF containing 4 mM Ca^{2+}. The black arrow shows evoked responses upon single AP propagation. Synaptic release probability was 1 (no failures). During wash-in of 4 mM Sr^{2+} (last 3 panels), discrete events appear in the wake of the stimulation (blue arrowheads). **b)** Amplitude histogram of evoked responses (green bars) and delayed events (blue bars) of the example. The black arrows shows the evoked responses upon single AP propagation. Fluctuations of baseline fluorescence were also analyzed (gray bars). **c)** Amplitude histograms of two different boutons with evoked responses (green bars), delayed events (blue bars) and fluctuation of baseline fluorescence (gray bars).

3.5 Non-linear response of iGluSnFR to glutamate release

Fusion of a single vesicle produces an extremely localized source of glutamate in the synaptic cleft that rapidly disperses through diffusion. To explore how diffusing glutamate molecules interact with iGluSnFR and postsynaptic AMPA receptors, Christian Schulze set up a Monte Carlo model of a spine synapse surrounded by astrocytes. Simulated fusion of a

transmitter vesicle in the center of the synaptic cleft produced a local cloud of glutamate that filled the entire cleft within 10 µs and was largely cleared after 100 µs (Figure 12a). Consequently, iGluSnFR molecules became bound (and fluorescent) and doubly-bound AMPA receptors opened (Figure 12b). The model also allowed exploring how different orientations of the synapse with respect to the optical axis would affect the amplitude of iGluSnFR signals ($\Delta F/F_0$, Figure 12c, d). The largest signal in response to fusion of a single vesicle (quantal amplitude, q) is generated when both, spine and axon are in the focal plane, aligning the synaptic cleft with the optical axis. A synapse where the spine or the axon are tilted with respect to the focal plane will produce smaller signals, because tilted positions move more extrasynaptic bouton membrane into the point spread function (PSF). Bouton membrane outside the synaptic cleft contributes to F_0, but is never exposed to high concentrations of glutamate, thus decreasing the relative change in fluorescence ($\Delta F/F_0$). This was an important insight: horizontal axonal orientation is typical in organotypic slice cultures (Blumer et al., 2015), but I still expect some variability in q between individual boutons due to variable spine orientations. Thus, when modeling iGluSnFR amplitude distributions, q was treated as a free parameter (range: 20-120% $\Delta F/F_0$).

Fraction of bright iGluSnFR and fraction of open AMPARs was low after release of a single vesicle (Figure 12) assuming 3000 molecules of glutamate per vesicle. Simulated release of multiple vesicles revealed similar saturation curves for iGluSnFR and AMPARs, which could be approximated by a simple hyperbolic function:

Equation 1: $$r = \frac{[Glu]}{K_d + [Glu]}$$

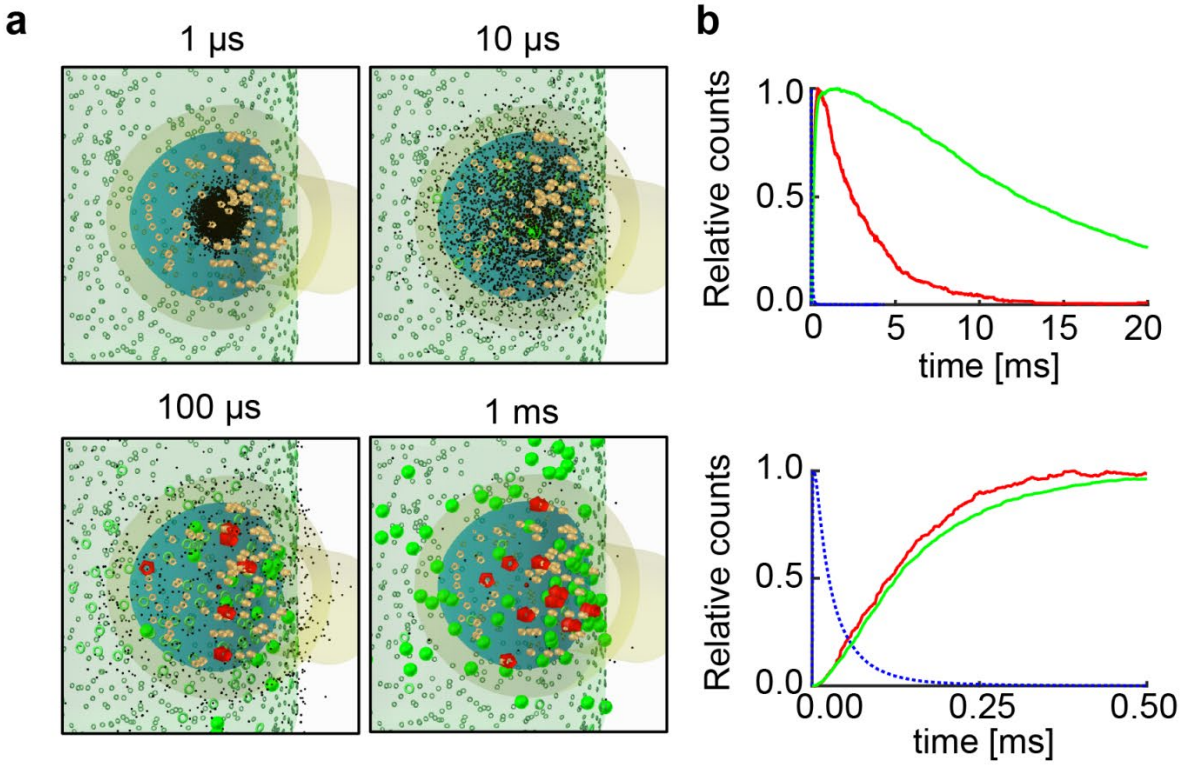
a
1 µs
10 µs
100 µs
1 ms
b
Relative counts
1.0
0.5
0.0
0
5
10
15
20
time [ms]
Relative counts
1.0
0.5
0.0
0.00
0.25
0.50
time [ms]

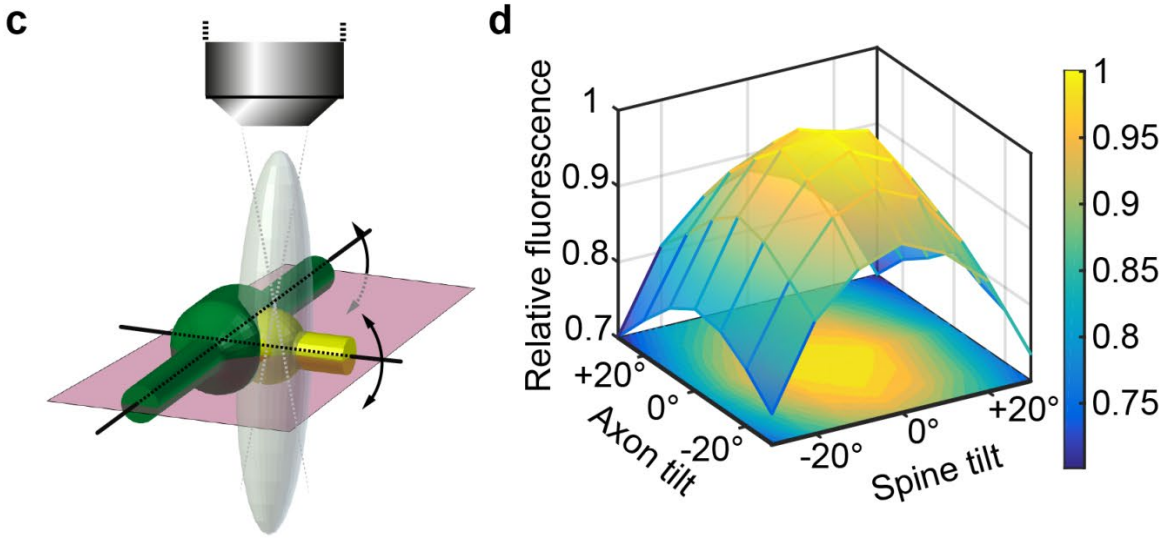
c
d
Relative fluorescence
1
0.9
0.8
0.7
+20°
0°
-20°
Axon tilt
-20°
0°
+20°
Spine tilt
1
0.95
0.9
0.85
0.8
0.75

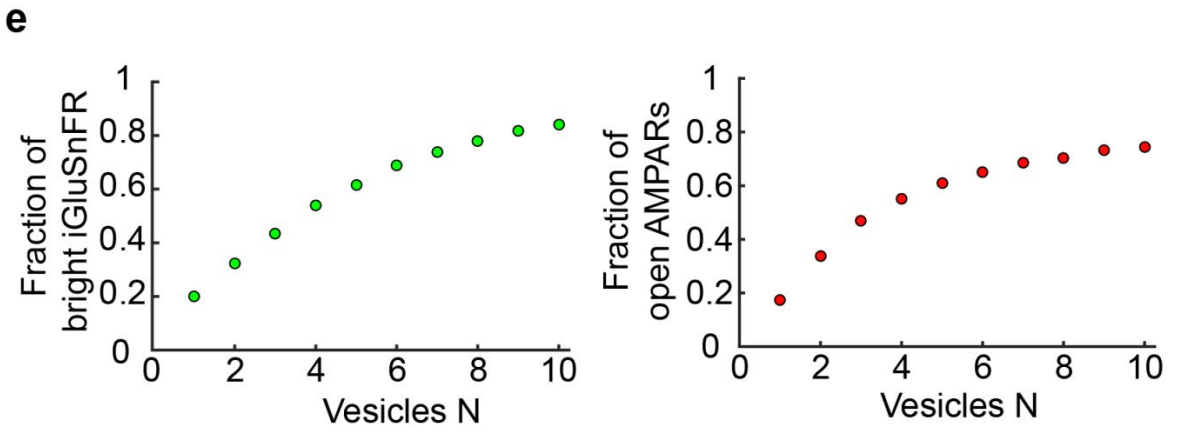
e
Fraction of bright iGluSnFR
1
0.8
0.6
0.4
0.2
0
0
2
4
6
8
10
Vesicles N
Fraction of open AMPARs
1
0.8
0.6
0.4
0.2
0
0
2
4
6
8
10
Vesicles N

Figure 12: Monte Carlo simulation of glutamate diffusion in the synaptic cleft

a) The model consists of a presynaptic terminal with iGluSnFR molecules (pale green) opposed to a spine with AMPA receptors (pale red) randomly distributed in a disc of 300 nm, separated by a 20 nm synaptic cleft. The synapse was embedded in a network of astrocytes equipped with glutamate transporters. Open state AMPARs bound to two glutamate molecules are depicted in red. iGluSnFR molecules bound to a single glutamate molecule and in a fluorescent state are depicted in green. **b)** Simulated reaction time profile of AMPARs opening and iGluSnFR in a bright fluorescent state after release of a single vesicle. Fusion of a vesicle containing 3000 glutamate molecules in the center of the active zone leads to a rapidly decaying glutamate transient (dashed blue curve), leaving activated AMPA receptors (red) and fluorescent iGluSnFR (green) in its wake. **c)** Scheme representing the optimal orientation of axon (green) and spine (yellow) with respect to the optical axis. iGluSnFR fluorescence was evaluated inside the simulated point spread function (PSF, depicted in grey). The synaptic cleft is in the center of the PSF. **d)** Plot of the normalized fluorescence transient with respect to tilted positions of axon or spine. Tilting the axon or the spine reduces $\Delta F/F_0$, as more iGluSnFR molecules outside the synaptic cleft are inside the PSF, contributing to the resting fluorescence F_0. **e)** Fraction of bright iGluSnFR bound to glutamate (left panel) and fraction of open AMPARs (right panel) after release of 1-10 vesicles assuming 3000 glutamates per vesicles. Occupancy of iGluSnFR and AMPA receptors is similar after single vesicle release, resulting in similar saturation curves.

3.6 The dynamic range of postsynaptic responses

My optical measurements demonstrate a steep dependence of release probability on $[Ca^{2+}]_e$. Would AMPA receptors report increased glutamate concentrations as larger currents? To measure the strength of unitary connections, I performed dual patch-clamp recordings from connected pairs of CA3 and CA1 pyramidal cells (Figure 13a and b). For each pair, I recorded EPSCs in 1 mM and in 4 mM $[Ca^{2+}]_e$, switching the sequence (low to high / high to low Ca^{2+}) between experiments. Between the two conditions, the median fold change in connection strength (6.02 fold, n = 7 pairs) was slightly but non-significantly smaller (Mann-Whitney U p-value=0.070) than the median fold change in iGluSnFR signal (Figure 13b) (10.81 fold, averaging over failures and successes, n = 9 boutons from 9 cells),

suggesting that AMPA receptors were becoming saturated and were not quite able to report the very high transmitter concentrations reached in 4 mM $[Ca^{2+}]_e$.

Due to AMPAR desensitization, we expected to see some degree of depression at higher stimulation frequencies, especially under conditions of high release probability (4 mM $[Ca^{2+}]_e$). I therefore analyzed paired-pulse ratios (48 ms inter-stimulus interval) in connected CA3-CA1 pairs. In 1 mM Ca^{2+}, EPSCs showed paired-pulse facilitation (ISI = 48 ms, PPR = 1.56, n=7 pairs) (Figure 13d), which was absent in 4 mM Ca^{2+} (PPR = 0.86, n=7 pairs). iGluSnFR responses showed weak facilitation in 1 mM Ca^{2+} (PPR = 1.18, n = 9 boutons + 4 boutons measured in 1 mM Ca^{2+} only (Figure 13d)) and weak depression in 4 mM $[Ca^{2+}]_e$ (PPR = 0.08, n= 9 boutons), consistent with the expected partial depletion of readily-releasable vesicles under high release probability conditions. Therefore, Schaffer collateral synapses are able to maintain a fairly linear paired pulse response over a 10.8 fold change in release probability, which is remarkable.

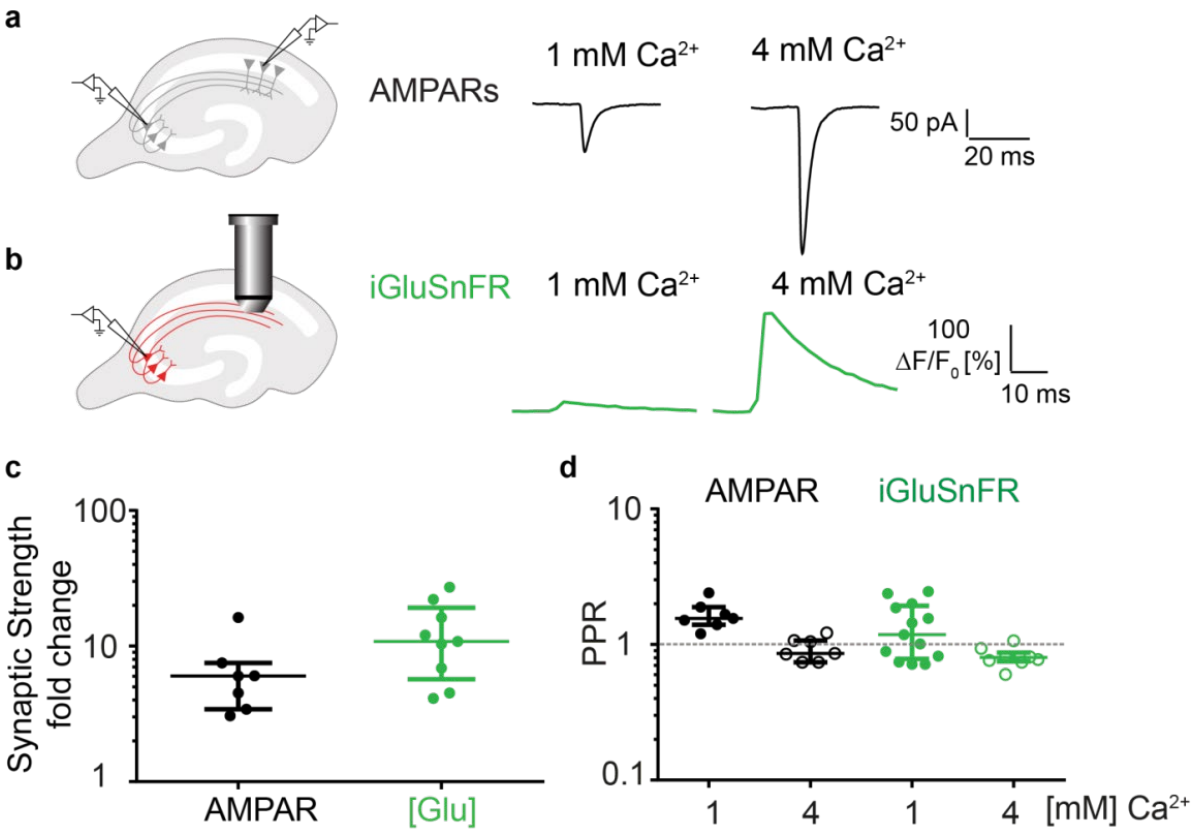

Figure 13: Dynamic range and paired pulse facilitation of AMPAR mediated currents and iGluSnFR signal

a) EPSCs were measured by dual patch-clamp recordings from connected CA3-CA1 pyramidal cell pairs. Perfusion was switched from 1 mM to 4 mM $[Ca^{2+}]_e$, leading to increased EPSC amplitudes. On the right, example of average responses in each of the saline solution **b)** iGluSnFR signals were measured as described previously (Figure 6). On the right, example of average responses in each of the saline solution. The switching sequence (low-high / high-low) was reversed between experiments. **c)** Increasing $[Ca^{2+}]_e$ increased the amplitude of AMPAR EPSCs by a factor of 6.02 (median, n = 7 pairs), the iGluSnFR response by 10.81 (median, n = 9 boutons). There is no significant difference (Mann-Whitney U p = 0.07) between the fold-change from low to high $[Ca^{2+}]_e$ of AMPARs and iGluSnFR signal. **d)** In 1 mM Ca^{2+}, EPSCs showed paired-pulse facilitation (ISI = 48 ms, PPR = 1.56 n = 7 pairs), which was absent in 4 mM Ca^{2+} (PPR = 0.86, n= 7 pairs). iGluSnFR responses showed weak facilitation in 1 mM Ca^{2+} (ISI = 48 ms, PPR = 1.18, n=9 boutons + 4 boutons measured in 1 mM Ca^{2+} only) and weak depression in 4 mM Ca^{2+} (PPR = 0.80, n=9 boutons). Boutons with very small iGluSnFR responses were not sampled.

3.7 Extracting synaptic parameters by histogram analysis

Histograms of iGluSnFR responses from individual boutons often showed multiple peaks (Figure 14; Appendix 7.1, Histograms counts of iGluSnFR responses measured in 2 mM Ca^{2+}). If these peaks indicate the simultaneous release of one, two, three, or more vesicles in response to a single presynaptic action potential, there are clear predictions about the amplitude and spacing of the peaks as the amplitude of the peaks would be expected to follow binomial statistics, as famously shown for endplate potentials (Boyd and Martin, 1956). Due to the saturation of iGluSnFR at 440% $\Delta F/F_0$, however, quantal peaks should not be equidistant, but compressed according to a hyperbolic saturation function (Equation 1).

To investigate release statistics in more detail, I acquired a dataset of 21 boutons in 2 mM Ca^{2+}, which provides slightly elevated p_r and a high variance of released vesicles. As the imaging conditions varied between individual experiments (depth in tissue, expression level, laser power), I analyzed the baseline noise ($\Delta F/F_0$ before stimulation) and discarded all experiments with a full width at half maximum above 0.4. The fluorescence trace in every trial was fit with a kernel (exponential decay function) to extract the peak amplitude (section 2.6). To extract the three quantal parameters n, p_{ves}, and q from the response histograms, predictions were generated (probability density functions) for all possible parameter triplets. First, for every combination of n and p_{ves}, the binomial probabilities were calculated for the different outcomes (failures, univesicular and various multivesicular events (Figure 14a). From the baseline fluorescence distribution of the synapse in question, the expected variability of failure events could be extracted (width of Gaussian, Figure 14b). As photon shot noise increases with the square root of the number of detected photons, amounts of 'noise' had to be added to the expected quantal peaks. To account for partial saturation of iGluSnFR at high glutamate concentrations ((F_{max} - F_0) / F_0 = 440%, see methods), the expected quantal peaks were not spaced at integer multiples of q, but according to the

saturation function (Equation 1). For every prediction, the amplitude was scaled to match the number of observations (histogram) and calculated the root mean square error (RMS) (Figure 14d). I observed that different combinations of n and p_{ves} generated near identical predictions, as there was no 'cost' associated with increasing n in the model. I therefore selected the prediction with the smallest number of vesicles that was within 1% of the minimum mean square error as the most plausible biophysical mechanism for the synapse in question. Furthermore, as I only stimulate individual boutons for 100 trials it seemed reasonable to assume that I could not estimate properly the probability of a high number of simultaneously released vesicles. To test whether a multivesicular model provide better fits to the data than a univesicular model, I fixed $n = 1$ and introduced the CV of responses (width of the Gaussian fit) as a new free parameter (Figure 14c). Thus, both models had the same number of free parameters. While the multivesicular model (binomial statistics) provided a better fit for some boutons (e.g. Figure 14c), many boutons recorded in 2 mM Ca^{2+} were fit equally well by uni- and multivesicular models of release (Figure 14d, black points).

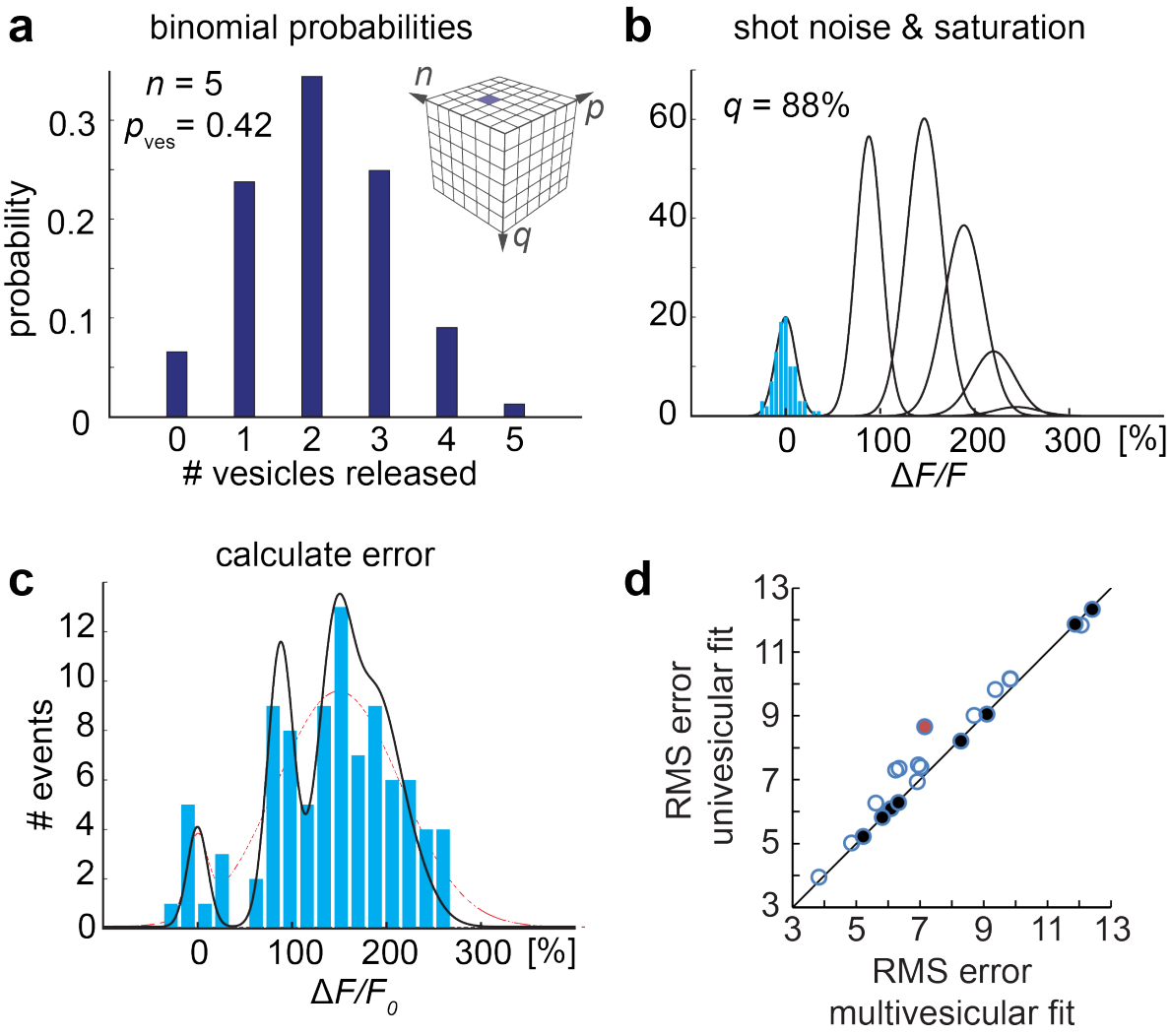

Figure 14: Extracting *n*, p_{ves} and *q* using a binomial model

a) For a combination of *n* and p_{ves}, the binomial probabilities of the possible outcomes were calculated (here: *n* = 5 vesicles and p_{ves}= 0.42). **b)** Without stimulation, amplitudes were normally distributed around zero (cyan bars). The width of this noise distribution, a function of the number of photons detected from a particular bouton, was used to determine the width of the expected Gaussian probability density functions (black) for a chosen quantal amplitude *q* (here: 88% $\Delta F/F_0$). iGluSnFR saturation (max. $\Delta F/F_0$ = 440%) was taken into account when setting the expected amplitudes of multiquantal events. **c)** The resulting probability density function (sum of the Gaussians) was compared to the measured amplitude distribution of a single bouton (cyan, recorded in 2 mM Ca^{2+}). RMS error was calculated and the best fit (shown here) was selected to determine the synaptic parameters, *n*, p_{ves} and *q*. **d)** Correlation plot of the RMS error of a univesicular fit (*n*=1) vs multivesicular fit (possible values for *n*: 1 to 20), n=21 boutons. The black points represents the boutons where the minimal RMS error obtain through exhaustive search of the free parameters was equal for the two models. The red point is the example shown in (c).

To further constrain the fitting procedure, I performed a set of experiments switching between 1 mM and 4 mM $[Ca^{2+}]_e$ while optically recording from individual boutons and maintaining somatic whole-cell access (Figure 15a-d). The fitting algorithm now had to find values for *q* and for *n* that could account for both histograms, as the quantal size and number of release-ready vesicles are not expected to change with $[Ca^{2+}]_e$. Only p_{ves} was allowed to vary between the low and high $[Ca^{2+}]_e$ conditions. The fitting results provided a convincing explanation why some boutons generated multi-peaked histograms in 1 mM $[Ca^{2+}]_e$ (Figure15d) while others showed multiple peaks only in 4 mM $[Ca^{2+}]_e$ (Figure 15b): p_{ves} differs between synapses. Due to partial saturation of iGluSnFR at high glutamate concentration, quantal peaks for 3 and more simultaneously released vesicles are not resolved, but compressed into a broad peak (Figure 15 a,d). Again, *n* should be considered as a lower limit, required to explain the observed distribution of iGluSnFR signals. Equally good fits can be generated with larger vesicle numbers (resulting in proportionally smaller p_{ves}). The estimates of quantal size are very uniform between different boutons (Figure 15e) and in different conditions (Figure 15f).

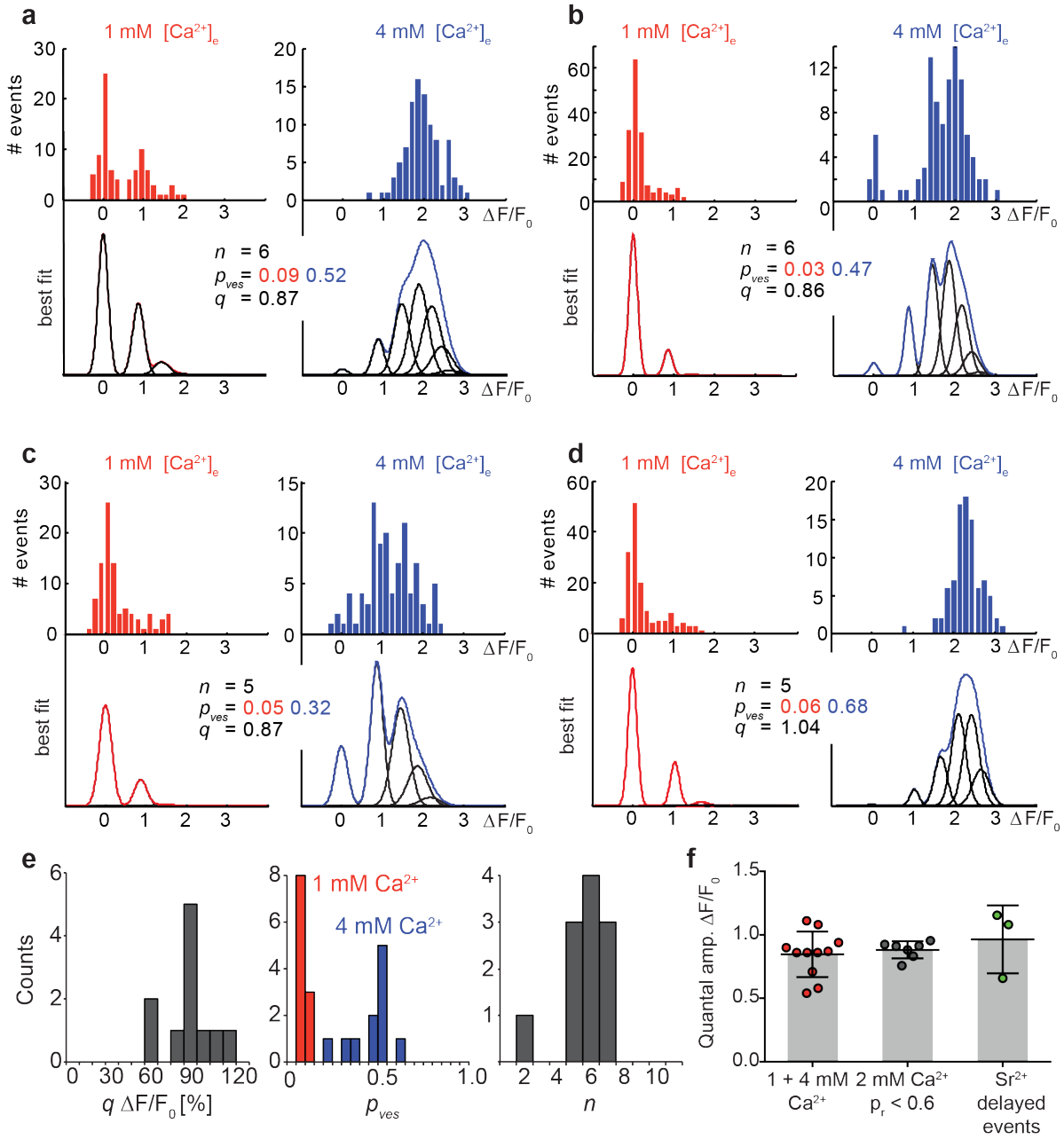

Figure 15: Quantal parameters of Schaffer collateral synapses

a-d) Single bouton response distributions recorded in low (1 mM) and high (4 mM) Ca^{2+}. Four examples from 4 different slice cultures. The binomial fitting procedure was applied to both histograms, searching for the best combined fit under the condition that *n* and *q* had to be identical in low and high Ca^{2+} while p_{ves} could vary. Best fits (probability density functions) and extracted parameters are shown below the experimental data. **e)** Summary of extracted quantal parameters, p_{ves} 1 mM Ca^{2+} = 0.045 ± 0.009; p_{ves} 4 mM Ca^{2+} = 0.415 ± 0.036; *q* = 0.85 ± 0.05; *n* =5.63 ± 0.43; (n = 11 boutons). Values are given as mean ± sem. **f)** Quantal amplitude estimates in 3 different recording conditions (independent datasets) are not different.

3.8 Publication in PNAS 2018

Ultrafast glutamate sensors resolve high-frequency release at Schaffer collateral synapses

Nordine Helassa[a,1,2], Céline D. Dürst[b,1], Catherine Coates[a], Silke Kerruth[a], Urwa Arif[a], Christian Schulze[b], J. Simon Wiegert[b,3], Michael Geeves[c], Thomas G. Oertner[b] and Katalin Török [a,4]

[a]Molecular and Clinical Sciences Research Institute, St George's, University of London, London SW17 0RE, UK; [b]Institute for Synaptic Physiology, Center for Molecular Neurobiology Hamburg, Hamburg 20251, Germany; [c]School of Biosciences, University of Kent, Canterbury CT2 7NZ, UK

[1]N.H. and C.D.D. contributed equally to this work.

[2]Present address: Department of Cellular and Molecular Physiology, Institute of TranslationalMedicine, University of Liverpool, L69 3BX Liverpool, United Kingdom.

[3]Present address: Research Group Synaptic Wiring and Information Processing, Center for Molecular Neurobiology Hamburg, 20251 Hamburg, Germany.

[4]To whom correspondence should be addressed. Email: k.torok@sgul.ac.uk.

This article contains supporting information online at www.pnas.org/lookup/suppl/doi:10.1073/pnas.1720648115/-/DCSupplemental.

Disclaimer:

The following section has been published. For this thesis, the original manuscript has been included in full. Numbering of figures and references has been reformated. I performed all experiments on hippocampal neurons including analysis and contributed to the writing of the publication (Figure 16i-m, Figure 17, Figure 18, Figure21, Figure 22, Figure 23, Figure 24, Figure 25).

Author contributions

J.S.W., T.G.O., and K.T. designed research; N.H., C.D.D., C.C., U.A., and K.T. performed research; N.H., C.D.D., C.C., S.K., C.S., M.G., T.G.O., and K.T. analyzed data; and T.G.O. and K.T. wrote the paper. The authors declare no conflict of interest. his article is a PNAS Direct Submission. This open access article is distributed under Creative Commons Attribution-Non Commercial-No Derivatives License 4.0 (CC BY-NC-ND). Data deposition: The plasmids for $iGlu_f$ and $iGlu_u$ have been deposited in the Addgene database, https://www.addgene.org/75443/.

ACKNOWLEDGMENTS

We thank Dr. Zoltan Ujfalusi (University of Kent) for assistance with stopped-flow experiments, Iris Ohmert for the preparation of organotypic cultures, and Dr. David Trentham for comments on the manuscript. Use of The Institute of Translational Medicine, University of Liverpool Imaging Facility is gratefully acknowledged. This project was supported by Wellcome Trust Grant 094385/Z/10/Z (to K.T.); Biotechnology and Biological Sciences Research Council Grant BB/M02556X/1 (to K.T.); German Research Foundation Grants SPP 1665, SFB 936, FOR 2419 (to T.G.O.), SPP 1926, and FOR 2419 (to J.S.W.); and European Research Council Grant ERC-2016-StG714762 (to J.S.W.).

3.8.1 ABSTRACT

Glutamatergic synapses display a rich repertoire of plasticity mechanisms on many different time scales, involving dynamic changes in the efficacy of transmitter release as well as changes in the number and function of postsynaptic glutamate receptors. The genetically encoded glutamate sensor iGluSnFR enables visualization of glutamate release from presynaptic terminals at frequencies up to ~10 Hz. However, to resolve glutamate dynamics

during high frequency bursts, faster indicators are required. Here we report the development of fast (iGlu$_f$) and ultrafast (iGlu$_u$) variants with comparable brightness, but increased K_d for glutamate (137 μM and 600 μM, respectively). Compared to iGluSnFR, iGlu$_u$ has a 6-fold faster dissociation rate in vitro and 5-fold faster kinetics in synapses. Fitting a three-state model to kinetic data, we identify the large conformational change after glutamate binding as the rate-limiting step. In rat hippocampal slice culture stimulated at 100 Hz, we find that iGlu$_u$ is sufficiently fast to resolve individual glutamate release events, revealing that glutamate is rapidly cleared from the synaptic cleft. Depression of iGlu$_u$ responses during 100 Hz trains correlates with depression of postsynaptic EPSPs, indicating that depression during high frequency stimulation is purely presynaptic in origin. At individual boutons, the recovery from depression could be predicted from the amount of glutamate released on the second pulse (paired pulse facilitation/depression), demonstrating differential frequency-dependent filtering of spike trains at Schaffer collateral boutons.

Significance

Excitatory synapses convert presynaptic action potentials into chemical signals that are sensed by postsynaptic glutamate receptors. To eavesdrop on synaptic transmission, genetically encoded fluorescent sensors for glutamate have been developed. However, even the best available sensors lag behind the very fast glutamate dynamics in the synaptic cleft. Here, we report the development of an ultrafast genetically encoded glutamate sensor, iGlu$_u$, which allowed us to image glutamate clearance and synaptic depression during 100 Hz spike trains. We found that only boutons showing paired-pulse facilitation were able to rapidly recover from depression. Thus, presynaptic boutons act as frequency-specific filters to transmit select features of the spike train to specific postsynaptic cells.

3.8.2 Introduction

The efficacy of synaptic transmission is not constant, but changes dynamically during high-frequency activity. In terms of information processing, different forms of short-term plasticity act as specific frequency filters: Facilitating synapses are most effective during high frequency bursts, while depressing synapses preferentially transmit isolated spikes preceded by silent periods (Markram et al., 1998). Mechanistically, a number of pre- and postsynaptic parameters change dynamically during high frequency activity, e.g. the number of readily releasable vesicles, presynaptic Ca^{2+} dynamics, and the properties of postsynaptic receptors, which may be altered by Ca^{2+}-activated enzymes (Regehr, 2012; Jenkins and Traynelis, 2012).

Electrophysiological analysis of short-term plasticity, by monitoring postsynaptic responses, is complicated by the fact that neurons are often connected by more than one synapse. In addition, it is not straightforward to distinguish between pre- and postsynaptic plasticity mechanisms. Directly measuring glutamate concentrations inside the synaptic cleft during high-frequency activity would allow isolating the dynamics of the vesicle release machinery from potential changes in glutamate receptor properties (e.g. desensitization, phosphorylation, lateral diffusion). Early fluorescent glutamate sensors, constructed by chemical labelling of the fused glutamate binding lobes of ionotropic glutamate receptor GluA2 (termed S1S2) (Best and Török, 2005; Chen and Gouaux, 1997; Kuusinen et al., 1995) and later of the bacterial periplasmic glutamate/aspartate binding protein (GluBP) (de Lorimier et al., 2002; Hu et al., 2008), were not suitable for quantitative single-synapse experiments due to their low dynamic range. Genetically encoded FRET-based fluorescent glutamate sensors e.g. FLIPE, GluSnFR and SuperGluSnFR (Figure 16a) have relatively low FRET efficiency, since glutamate binding causes only a small conformational change in GluBP (Hires et al., 2008; Okumoto et al., 2005; Tsien, 2005). A breakthrough in visualizing

glutamate release in intact tissue was achieved with iGluSnFR, a single-fluorophore glutamate sensor (Marvin et al., 2013). Following the concept developed for the GCaMP family of genetically encoded Ca^{2+} sensors (Nakai et al., 2001), iGluSnFR was constructed from circularly permuted (cp) EGFP (Baird et al., 1999) inserted into the GluBP sequence, creating a large fragment $iGlu_l$ (residues 1-253) at the N-terminus and a small fragment $iGlu_s$ (residues 254-279) at the C-terminus. Upon glutamate binding GluBP is reconstituted from its two fragments, pulling the cpEGFP β-barrel together, resulting in a ~5-fold fluorescence increase. Extracellular expression was achieved by fusion with a PDGFR peptide segment (Marvin et al., 2011).

iGluSnFR has high glutamate affinity and a large dynamic range, but reacts relatively slowly. Its fluorescence response is reported to have a decay half-time ($t_{1/2}$) of 92 ms upon synaptic glutamate release (Marvin et al., 2013). Imaging iGluSnFR in cultured hippocampal neurons during 10 Hz stimulation shows summation, which, without deconvolution, might indicate that glutamate accumulates during stimulation (Taschenberger et al., 2016). Deconvolution of the data suggests that glutamate is cleared between release events (Taschenberger et al., 2016). iGluSnFR itself is too slow for accurate tracking of synaptic glutamate dynamics during high frequency transmission. Here we introduce two fast iGluSnFR variants, $iGlu_f$ (for 'fast') and $iGlu_u$ (for 'ultrafast') and identify the rate-limiting step leading to bright fluorescence upon glutamate binding. In organotypic slice cultures of rat hippocampus, $iGlu_u$ directly reports discrete synaptic glutamate release events at 100 Hz. Combining high-speed two-photon imaging and electrophysiology, we show that short-term depression of Schaffer collateral AMPA responses is fully accounted for by the depression of glutamate release. Furthermore, we show a tight correlation between paired-pulse facilitation and rapid recovery from post-tetanic depression at individual boutons, suggesting that differential use of presynaptic resources (readily releasable vesicles) determines the filtering properties of CA3 pyramidal cell boutons.

3.8.3 Results

3.8.3.1 Affinity variants of iGluSnFR by binding site mutations

We generated six iGluSnFR variants by mutating residues coordinating glutamate or in the vicinity of the binding site (Hires et al., 2008). Two of the mutations lowered, and four increased, the K_d for glutamate. Variants in order of increasing dissociation constant (K_d) were E25A < E25R < iGluSnFR < E25D < S72T < R24K < T92A (from 19 μM to 12 mM) with Hill coefficients of 1.3–2.6 (Figure 20a and Table 1).

We selected the two variants with the fastest response kinetics, iGluSnFR E25D (termed $iGlu_f$) and iGluSnFR S72T (termed $iGlu_u$) (Figure 20a and b) for detailed biophysical characterization as isolated proteins and as membrane-bound glutamate sensors on HEK293T cells and pyramidal neurons. Selectivity for glutamate was determined against aspartate, glutamine, D-serine, GABA, and glycine. $iGlu_f$ and $iGlu_u$ affinities for aspartate were similar to that for glutamate, as previously reported for iGluSnFR (Marvin et al., 2013), but with two- to threefold lower fluorescence enhancement. The affinity for glutamine was in the millimolar range for all three probes (Figure 20b-e) D-serine, GABA, and glycine evoked no detectable response. pKa for the glutamate-bound form was ~6.5 for iGluSnFR, $iGlu_f$, and $iGlu_u$, whereas the apo-form showed little pH dependence, indicating a well-shielded chromophore (Figure 20c-e). Brightness values for $iGlu_f$ and $iGlu_u$ were similar to that for iGluSnFR (Table 1). In vitro measurements gave a K_d for glutamate of 33 μM for iGluSnFR, similar to that previously reported (Marvin et al., 2013), while $iGlu_f$ and $iGlu_u$ had increased K_d values of 137 μM and 600 μM, respectively (Figure 16c and Table 1).

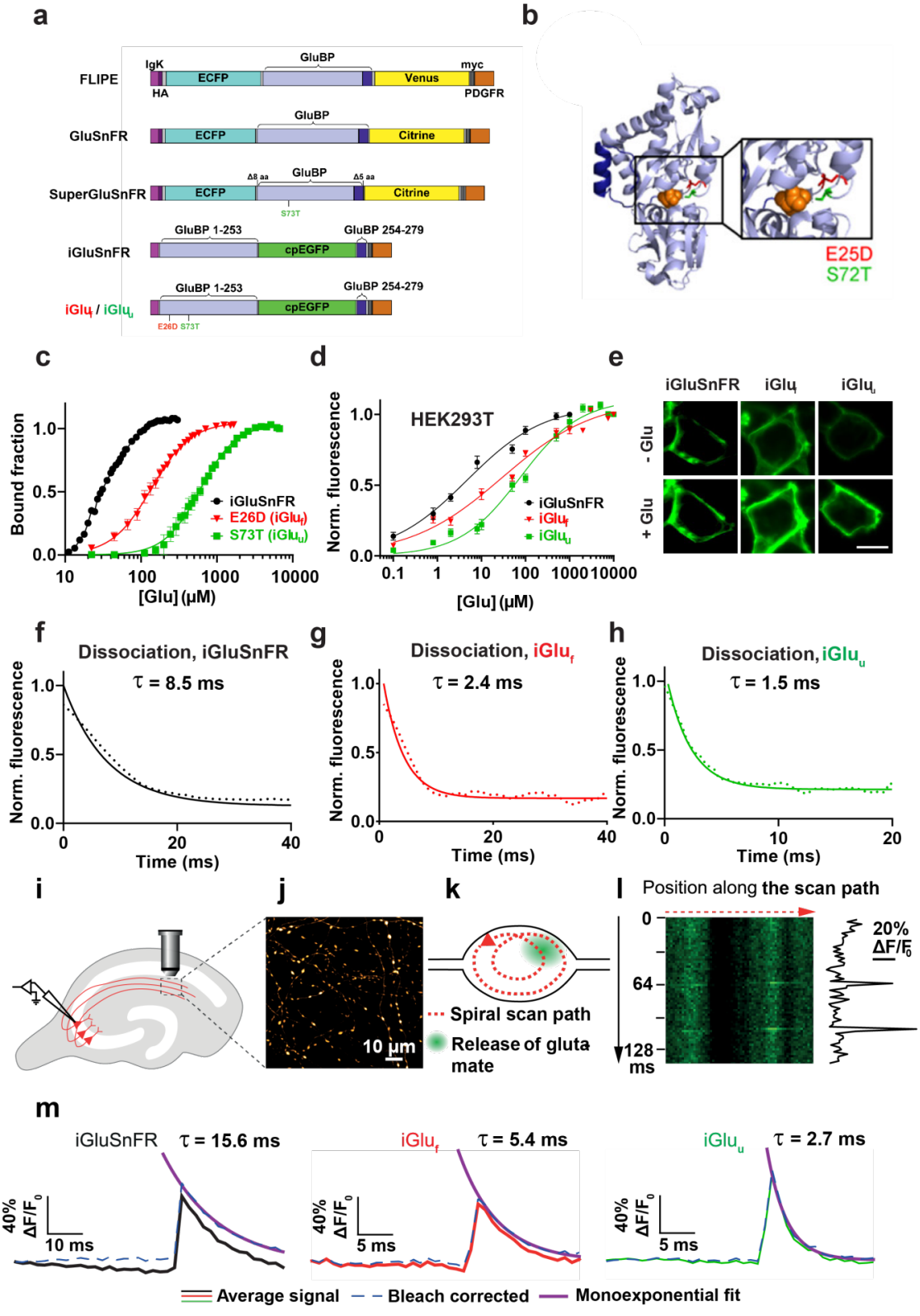
a
FLIPE
IgK
GluBP
myc
ECFP
Venus
HA
PDGFR
GluSnFR
Citrine
SuperGluSnFR
Δ8 aa
Δ5 aa
S73T
iGluSnFR
GluBP 1-253
GluBP 254-279
cpEGFP
iGlu$_f$ / iGlu$_u$
E26D S73T
b
E25D
S72T
c
Bound fraction
iGluSnFR
E26D (iGlu$_f$)
S73T (iGlu$_u$)
[Glu] (μM)
d
HEK293T
Norm. fluorescence
e
iGluSnFR
iGlu$_f$
iGlu$_u$
- Glu
+ Glu
f
Dissociation, iGluSnFR
τ = 8.5 ms
Time (ms)
g
Dissociation, iGlu$_f$
τ = 2.4 ms
h
Dissociation, iGlu$_u$
τ = 1.5 ms
i
j
10 μm
k
Spiral scan path
Release of glutamate
l
Position along the scan path
20% ΔF/F$_0$
m
iGluSnFR τ = 15.6 ms
iGlu$_f$ τ = 5.4 ms
iGlu$_u$ τ = 2.7 ms
40% ΔF/F$_0$
10 ms
5 ms
Average signal
Bleach corrected
Monoexponential fit

Figure 16: Genetically encoded glutamate indicators (GEGI)

a) Domain structure and design of FRET- and single fluorophore-based GEGI; key: (GluBP) (blue), cpEGFP (green), IgG kappa secretion tag (pink), hemagglutinin (HA) tag (purple), myc tag (grey) and a PDGFR transmembrane domain (brown); iGluSnFR lacks the hemagglutinin tag, GluBP 1-253 and 254-279 fragments are in light and dark blue, respectively; ∆8 aa and ∆5 aa specify deletions at the N- and C-terminus of GluBP introduced in GluSnFR. **b)** Design of selected iGluSnFR variants. Crystal structure of GluBP (PDB 2VHA, adapted from Hu et al. (Hu et al., 2008)). Selected mutated residues around the glutamate site are shown as red and green backbone as specified. Bound glutamate is represented in orange space filling display. **c)** Equilibrium glutamate binding titrations at 20°C for iGluSnFR (●), iGluSnFR E26D (iGlu$_f$) (▼) and iGluSnFR S73T (iGlu$_u$) (■) in vitro; **d)** Glutamate titrations in situ. iGluSnFR, iGlu$_f$ and iGlu$_u$ were expressed in HEK293T cells and titrated with glutamate. Data derived from iGluSnFR (n = 19), iGlu$_f$ (n = 41) and iGlu$_u$ (n = 33). **e)** Representative images of HEK293T cells prior to glutamate addition and at saturating (1, 3 and 10 mM, respectively) glutamate. The scale bar represents 10 µm. Glutamate dissociation kinetics of **(f)** iGluSnFR, **(g)** iGlu$_f$ and **(h)** iGlu$_u$ determined by stopped-flow fluorimetry. Experimental data (dotted lines) are overlaid by curves fitted to single exponentials (solid lines). Fluorescence changes are normalised to F_{max} of 1. Imaging glutamate release from single presynaptic terminals. **i)** Schematic representation of organotypic hippocampal slice culture with transfected and patch-clamped CA3 pyramidal cell; **j)** Imaging axonal projections in CA1 (two-photon stack, maximum intensity projection); **k)** Individual bouton with spiral scan path for 500 Hz sampling; **l)** Unfolded scan lines (64 lines, 2 ms/line), single trial. The scan line intersected the fusion site of the vesicle in two positions; Fluorescence time course ($\Delta F/F_0$) upon glutamate release stimulated by paired pulse stimulation (48 ms ISI) by iGlu$_u$. Decay time (τ_{off}) measurements with bleach correction (solid lines) for individual experiments by single exponential fit for **(m)** iGluSnFR (n = 13 boutons, 500 Hz sampling rate) and variants **(n)** iGlu$_f$ (n = 7 boutons, 1 kHz sampling rate) and **(o)** iGlu$_u$ (n = 7 boutons, 1 kHz sampling rate).

When expressed on the membrane of HEK293T cells, K_d values for glutamate were reduced to 3.1 ± 0.3 µM for iGluSnFR, 26 ± 2 µM for iGlu$_f$, and 53 ± 4 µM for iGlu$_u$ (measured at 37 °C, Fig. 1 D and E). A similar reduction of the K_d in the cellular environment compared with that in solution was reported for iGluSnFR (Marvin et al., 2013). The in situ fluorescence dynamic range ($(F_{+Glu} - F_{-Glu})/F$-Glu or $\Delta F/F_0$) was 1.0 ± 0.1 for both iGluSnFR and iGlu$_f$, but 1.7-fold larger for iGlu$_u$.

3.8.3.2 Kinetic measurements of iGluSnFR variants in vitro and in situ

Based on their large K_d values, we expected $iGlu_f$ and $iGlu_u$ to have faster glutamate release kinetics than iGluSnFR. Fluorescence measurements in a stopped-flow instrument indeed revealed faster off-rates for the new variants: using the non-fluorescent high-affinity GluBP 600n (Okumoto et al., 2005) in excess (0.67 mM) to trap released glutamate, k_{off} values of 110 s^{-1} (τ_{off} = 9 ms), 283 s^{-1} (τ_{off} = 4 ms) and 468 s^{-1} (τ_{off} = 2 ms) were obtained for iGluSnFR, $iGlu_f$ and $iGlu_u$, respectively, at 20°C (Figure 16f-h and Table 4). To compare in vitro response kinetics to physiological measurements, the temperature dependencies of the off-rates of iGluSnFR and the fast variants were determined. Linear Arrhenius plots were obtained between 4°C and 34°C (Figure 20f, g). For the fast variants, values exceeding the temporal precision of the stopped-flow device were linearly extrapolated (dotted line in Figure 20f, g). At 34°C, decay rates were 233 ± 3 s^{-1} for iGluSnFR (τ_{off} = 4.3 ms), 478 ± 5 s^{-1} for $iGlu_f$ (τ_{off} = 2.1 ms) and 1481 ± 74 s^{-1} $iGlu_u$ (τ_{off} = 0.68 ms). Thus, we were able to improve iGluSnFR kinetics by a factor of 6.3. To image glutamate dynamics in the synaptic cleft, we expressed the newly generated iGluSnFR variants in CA3 pyramidal cells in organotypic slice culture of rat hippocampus (Figure 16i). Fluorescence was monitored at single Schaffer collateral terminals in CA1 while action potentials were triggered by brief (2 ms) depolarizing current injections into the soma of the transfected CA3 neuron. As the precise orientation of the synaptic cleft on the bouton was unknown to us, we used rapid spiral scans to sample the entire surface of the bouton (Figure 16j). Typically, the spiral scan line intersected the release site multiple times (Figure 16k). To analyze individual trials, we sorted the columns (corresponding to positions along the scan line) according to their relative increase in fluorescence ($\Delta F/F_0$) and evaluated the top 80% (region of interest, ROI). In contrast to straight line scans, this method was robust against small movements of the bouton between trials (tissue drift). While 500 Hz sampling was sufficient for iGluSnFR, we increased the

scanning speed to 1 kHz to capture the peak of the very brief iGlu$_u$ response (Figure 16l). Responses started 4.5 ± 1.6 ms (mean ± SD) after the peak of the somatic action potential, consistent with a short propagation delay between CA3 and CA1. Consistent with the stochastic nature of glutamate release, individual boutons showed different release probabilities (median p_r = 0.56, range 0.05 – 1.0). For kinetic analysis, boutons with high release probability and good separation between release failures and successes were selected (Figure 21). The measured fluorescence decay time constants (τ_{off}) were 13.8 ± 3.8 ms for iGluSnFR, 5.2 ± 2.0 ms for iGlu$_f$, and 2.6 ± 1.0 ms for iGlu$_u$ (Figure 16m-o,Figure 22). Thus, compared to iGluSnFR, detected by iGlu$_u$ synaptic responses were revealed to be faster by a factor of 5.3. Interestingly, blocking glutamate uptake with DL-threo-beta-benzyloxyaspartate (DL-TBOA, 40 µM) did not slow down the decay of iGlu$_u$ fluorescence (Figure 23), suggesting that after sparse activation of Schaffer collateral synapses, glutamate is rapidly cleared from the synaptic cleft by diffusion, not by active transport. The situation may be different in highly active neuropil (Marvin et al., 2013; Zheng and Rusakov, 2015).

3.8.3.3 Synaptic glutamate dynamics during high frequency stimulation

With decay kinetics of 1-2 milliseconds, iGlu$_f$ and iGlu$_u$ were promising tools for direct tracking of synaptic glutamate during high frequency stimulation. The response of iGluSnFR, iGlu$_f$ and iGlu$_u$ to paired-pulse stimulation (Figure 17 and Figure 21) and to trains of 10 action potentials (APs) at 50, 67 and 100 Hz (Figure 24) was tested. While the responses of iGluSnFR and iGlu$_f$ suggested build-up of glutamate during high frequency stimulation, iGlu$_u$ responses revealed that even at 100 Hz stimulation, glutamate was completely cleared from the synaptic cleft between action potentials (Figure 17f, Figure 24i). Interestingly, the amplitudes of synaptic fluorescence signals ($\Delta F/F_0$) were similar for all three indicators,

suggesting that the on-rate, not the overall affinity, determined the number of glutamate-bound indicator molecules in the synaptic cleft.

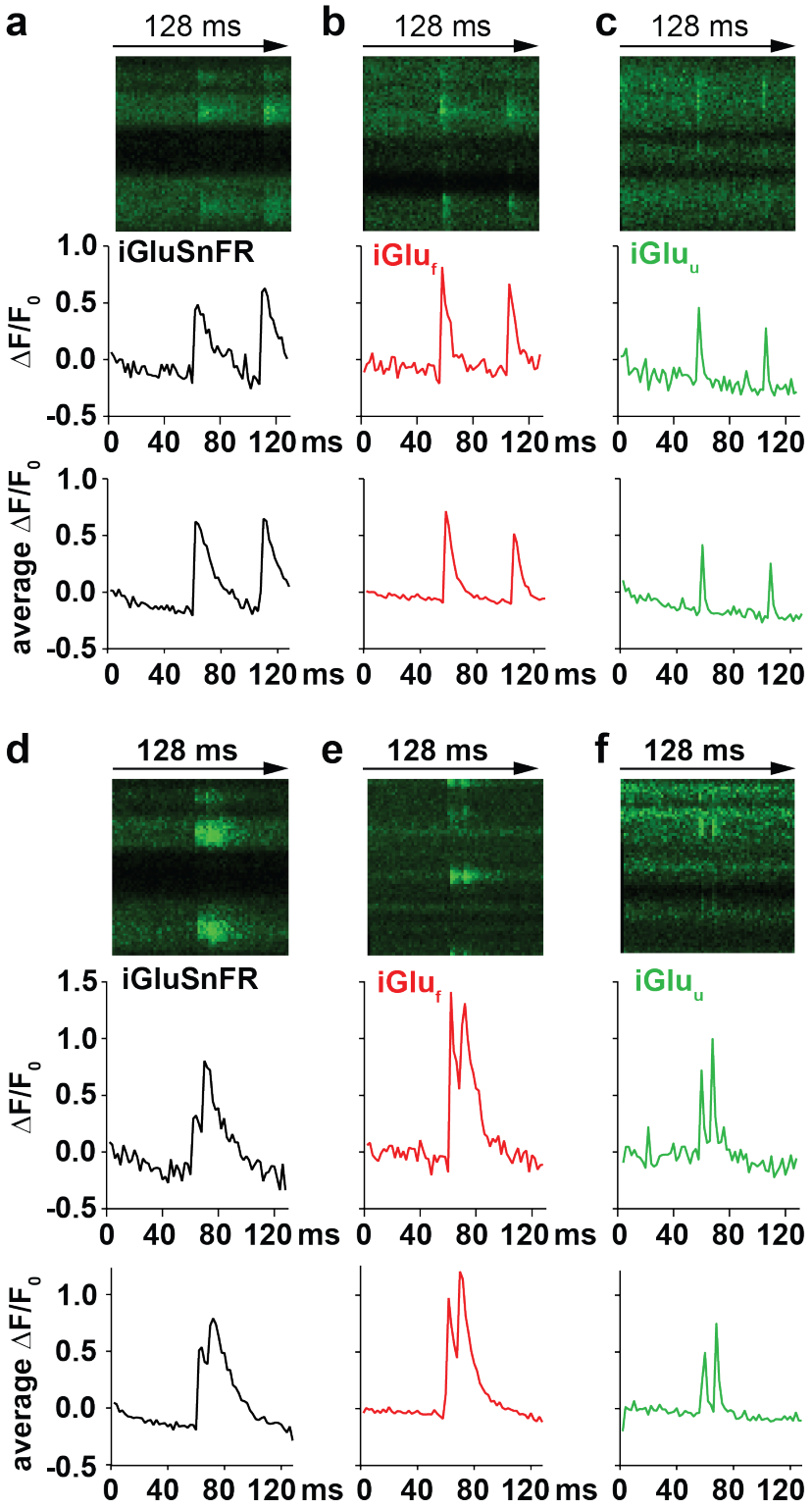

Figure 17: Imaging glutamate release from single presynaptic terminals

Spiral line scans at 500 Hz were used to cover the entire surface of individual boutons, intersecting the release site multiple times. Responses of **(a,d)** iGluSnFR, **(b,e)** $iGlu_f$ and **(c,f)** $iGlu_u$-expressing boutons stimulated by 2 somatic action potentials at 48 ms **(a-c)** and 10 ms inter-stimulus interval **(d-f)**. Upper traces: single trial responses. Lower traces: averages of 3-6 responses.

Excitatory postsynaptic potentials (EPSPs) in CA1 become strongly depressed during high-frequency stimulation (Kim et al., 2012). We were interested whether EPSP depression during 100 Hz stimulation could be fully accounted for by depression of glutamate release from presynaptic boutons. In paired recordings from connected CA3-CA1 pyramidal cells, we triggered APs in the CA3 cell by brief current injections while monitoring postsynaptic potentials (EPSPs) in the CA1 cell. The protocol consisted of a short high frequency burst (10 APs at 100 Hz) followed by a single AP 500 ms after the burst to probe recovery of synaptic function (Tsodyks and Markram, 1997). We repeated the protocol up to 100 times at 0.1 Hz and averaged the recorded traces (Figure 18a). The decay time constant of the recovery response was used to extract the amplitude of individual responses during the 100 Hz train by deconvolution (Figure 18b, d). As expected, connected CA3-CA1 pyramidal cell pairs showed strong depression during the high frequency train. The response to the recovery test pulse (#11) was not significantly different from the first EPSP in the train, indicating full recovery of synaptic function. To investigate depression and recovery of glutamate release, we evaluated $iGlu_u$ signals during identical stimulation (Figure 18c, e). Due to the extremely fast kinetics of the indicator, deconvolution of the fluorescence time course was not necessary: We read the peak amplitudes during the 100 Hz train directly from the averaged fluorescence time course (average of 10 individual trials sampled at 1 kHz, Figure 25). Glutamate release decreased during the train with a time course that matched EPSP depression (Figure 18c). This result points to a purely presynaptic origin of

depression, which is consistent with AMPA receptors rapidly recovering from desensitization after each release event ($r_{ecovery}$ = 5 ms (Crowley et al., 2007)). However, glutamate release 500 ms after the tetanus was still significantly depressed (two-tailed student's test, p-value: 0.0034) while AMPA receptor currents were not. This discrepancy suggests that the response of AMPA receptors to cleft glutamate was in fact potentiated 500 ms after the high frequency train, compensating for the reduced output of Schaffer collateral boutons.

3.8.3.4 Paired-pulse facilitation correlates with rapid recovery from depression

The rapid kinetics of $iGlu_u$ allowed us to analyze frequency filtering at individual boutons. On the second AP, boutons showed a wide range of facilitated (3 out of 12 boutons) or depressed responses (9 out of 12 boutons, Figure 18e). The response to the tenth AP was strongly depressed in all boutons (16% of response amplitude to first AP), with no correlation between the second and the tenth response (R^2 = 0.005, Figure 18f). Interestingly, a highly significant correlation was observed between the response to the second AP and the recovery response 500 ms after the high frequency train (R^2 = 0.72, Figure 18g). Could the $iGlu_u$ response to the 11^{th} pulse have been depressed due to bleaching of indicator molecules? We found no correlation between the amount of bleaching in individual experiments (F_0 before 11^{th} pulse / F_0 before 1^{st} pulse) and the amplitude of the recovery response ($(\Delta F/F_0)_{11th\ pulse}$ / $(\Delta F/F_0)_{1st\ pulse}$), indicating that poor recovery was not caused by excessive bleaching or dilution of indicator molecules. In conclusion, synapses that showed pronounced paired-pulse facilitation were also able to recover rapidly from depression, both of which is indicative of a low utilization of presynaptic resources (Tsodyks and Markram, 1997). Such boutons are optimized for the transmission of high-frequency activity (spike bursts). In contrast, boutons that showed paired-pulse depression were still depressed 500

ms after the high-frequency train. These boutons act as low-pass filters: They preferentially transmit isolated APs preceded by a silent period.

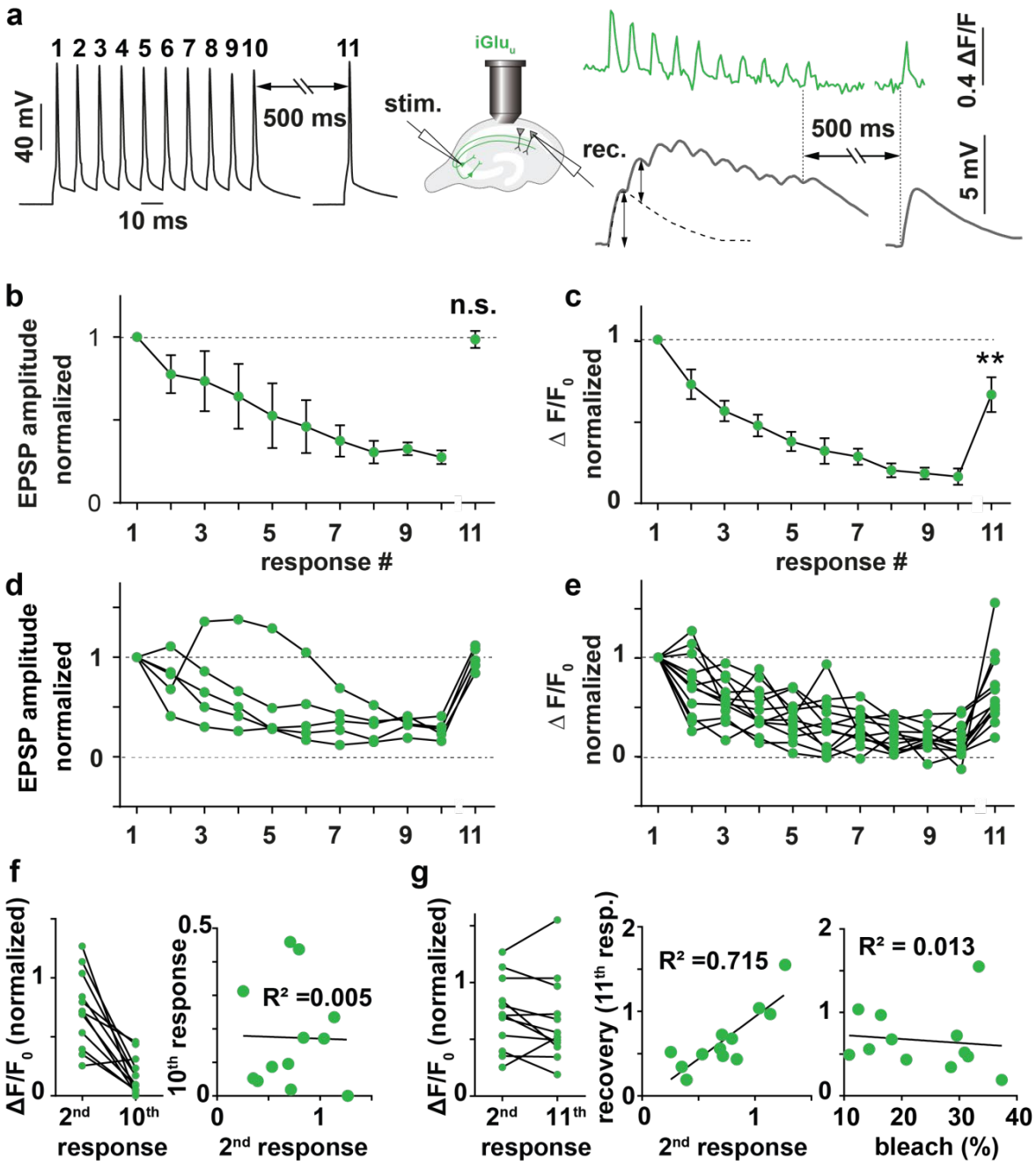

Figure 18: Depression and recovery of synaptic transmission during 100 Hz trains

a) Example of patch-clamp recording from a connected pair of CA3-CA1 pyramidal cells. Black trace: Induced action potentials (APs) in CA1 pyramidal cell, 100 Hz train and single AP. Gray trace: EPSPs in CA1 pyramidal cell (average of 50 sweeps). The single AP response (right) was used to extract EPSP amplitudes from the burst response (dotted line). Green trace: Single-bouton $iGlu_u$ response to identical stimulation (average of 10 sweeps). **b)** EPSPs (deconvolved amplitudes) show strong depression during the 100 Hz train, full recovery 500 ms later (n = 5 CA3-CA1 pairs), two-tailed student's test comparing EPSP #1 and EPSP #11. **c)** Glutamate release showed strong depression during the 100 Hz train, partial recovery 500 ms later (n = 12 boutons, 8 cells), two-tailed student's test comparing response #1 and response #11 ($p<0.01$). **d)** Individual paired recordings show consistent depression (response 10) and recovery (response #11). **e)** Individual Schaffer collateral boutons show large variability in 2nd response and in recovery response (#11) **(f)** $iGlu_u$ responses to second AP (paired-pulse facilitation/depression) were not correlated with total depression (response #10 normalized to response #1). **g)** $iGlu_u$ responses to second AP (response #2 normalized to response #1) were highly correlated with recovery after 500 ms (response #11 normalized to response #1). Recovery was independent of indicator bleach ($F_{0,\ response\ \#11}/\ F_{0,\ response\ \#1}$).

3.8.3.5 Response kinetics of iGluSnFR and variants $iGlu_f$ and $iGlu_u$ are based on the rate of structural change

Finally, we investigated the response mechanism of iGluSnFR and its fast variants using fluorescence stopped-flow with millisecond time resolution. In association kinetic experiments (20°C), the fluorescence response rates (k_{obs}) showed hyperbolic glutamate concentration dependence, approaching saturating rates of 643 s^{-1} and 1240 s^{-1} for iGluSnFR and $iGlu_f$, respectively (Figure 19a-d). For $iGlu_u$, in contrast, k_{obs} was found to be concentration-independent at 604 s^{-1} (Figure 19e,g). k_{off} values of 110 s^{-1}, 283 s^{-1} and 468 s^{-1} were obtained for iGluSnFR, $iGlu_f$ and $iGlu_u$, respectively (Table 4). We considered two different reaction pathways to explain our kinetic data (Figure 19g). iGluSnFR is represented as a complex of the large fragment of the GluBP domain (GluBP 1-253, $iGlu_l$), N-terminally flanking cpEGFP and of the C-terminally fused small GluBP fragment (GluBP 254-279, $iGlu_s$). The term $iGlu_l$~$iGlu_s$, indicates that the large GluBP fragment $iGlu_l$ and the small

fragment $iGlu_s$ are within one molecule, albeit separated by the interjecting cpEGFP. In Scheme 1, the binding of glutamate to $iGlu_l$ in $iGlu_l$~$iGlu_s$ is the primary step (no change in fluorescence). Glutamate binding is followed by a conformational change induced by the reattachment of $iGlu_s$ to Glu-bound $iGlu_l$, resulting in the highly fluorescent $Glu.iGlu_c^*$ complex (rate limiting step). According to Scheme 1, the hyperbolic dependence of the observed rate k_{obs} on the glutamate concentration [Glu] has the intercept of the y-axis at k_{-2} (see Kinetic Theory, eq. 7). At low [Glu], the initial linear slope gives $k_{+2}K_1$. At high [Glu], k_{obs} tends to $k_{+2}+k_{-2}$. Although k_{obs} for $iGlu_u$ appears essentially concentration independent, its kinetics is consistent with Scheme 1, with $k_{+2}+k_{-2}$ having a similar value to k_{-2} (Table 5).

In the alternative pathway (Scheme 2), the reattachment of $iGlu_s$ to $iGlu_l$ occurs without prior binding of glutamate. Therefore, $iGlu_l$~$iGlu_s$ with the GluBP fragments separated and complete GluBP domain ($iGlu_c$*) are in equilibrium. The conformational change that represents the reattachment of the two GluBP fragments is expected to generate a fluorescent state of cpEGFP. However, the equilibrium is likely to be strongly shifted to the separated, non-fluorescent state ($iGlu_l$~$iGlu_s$). Assuming that this equilibrium is fast and glutamate binding stabilizes the fluorescent state, at low [Glu], a linear dependence of k_{obs} on [Glu] is predicted with a slope of $K_3k_{+4}/(1+K_3)$ and an intercept of the y-axis at k_{-2} (see Kinetic Theory, eq. 15). Although at low [Glu], mono-exponential fluorescence changes are expected, as [Glu] increases, the concentration of $iGlu_c$* cannot be assumed to be at steady-state and slow isomerisation will limit k_{obs}, in a similar pattern to that for Scheme 1. Thus, at high [Glu], even if $iGlu_c$* and $Glu.iGlu_c$* have equal relative fluorescence intensities, biphasic fluorescence changes would be expected for the association reactions. As all the reactions studied here for the three variants had a single exponential appearance, we can exclude Scheme 2 as a possible reaction pathway. In conclusion, Scheme 1 provides an excellent fit to our measurements (Table 5), pointing to ‘Venus fly-trap’ closure by glutamate binding as a required first step for the conformational change that increases iGluSnFR fluorescence.

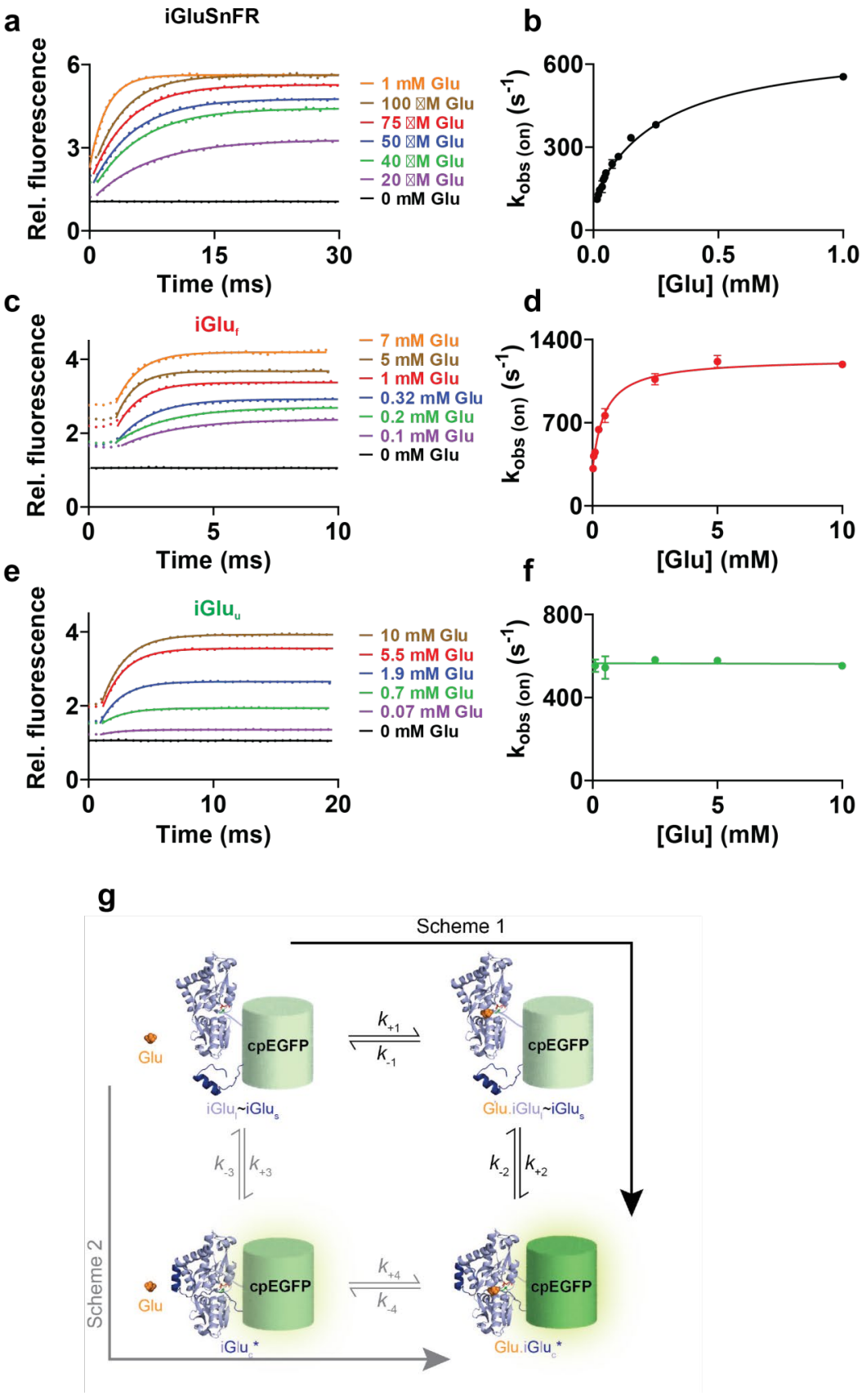
a
iGluSnFR
Rel. fluorescence
Time (ms)
1 mM Glu
100 ⊠M Glu
75 ⊠M Glu
50 ⊠M Glu
40 ⊠M Glu
20 ⊠M Glu
0 mM Glu
b
k_{obs} (on) (s^{-1})
[Glu] (mM)
c
iGlu$_f$
7 mM Glu
5 mM Glu
1 mM Glu
0.32 mM Glu
0.2 mM Glu
0.1 mM Glu
0 mM Glu
d
e
iGlu$_u$
10 mM Glu
5.5 mM Glu
1.9 mM Glu
0.7 mM Glu
0.07 mM Glu
0 mM Glu
f
g
Scheme 1
Scheme 2
Glu
cpEGFP
k_{+1}
k_{-1}
iGlu$_f$~iGlu$_s$
Glu.iGlu$_f$~iGlu$_s$
k_{-3}
k_{+3}
k_{-2}
k_{+2}
k_{+4}
k_{-4}
iGlu$_c$*
Glu.iGlu$_c$*

Figure 19: Kinetics of glutamate binding by iGluSnFR variants (20°C)

a, c, e) Glutamate association kinetics of iGluSnFR, $iGlu_f$ and $iGlu_u$, respectively. Stopped-flow records of iGluSnFR, $iGlu_f$ and $iGlu_u$ reacting with the indicated concentrations of glutamate. Experimental data (dotted lines) are overlaid with curves fitted to single exponentials (solid lines); **b, d, f)** Plot of observed association rates, $k_{obs(on)}$ of iGluSnFR, $iGlu_f$ and $iGlu_u$ as a function of glutamate concentration; **g)** Cartoon diagram depicting the putative molecular transitions of iGluSnFR and its fast variants to the fluorescent state. Key: cpEGFP (green), GluBP 1-253 ($iGlu_l$) (light blue) and 254-279 ($iGlu_s$) (dark blue) fragments, glutamate (orange).

3.8.4 Discussion

The development of iGluSnFR was a breakthrough in fluorescent glutamate sensors towards investigating neurotransmission in living organisms (Xie et al., 2016). Here we describe how to overcome one of the key limitations of iGluSnFR, its slow response kinetics, and use the new utrafast variant $iGlu_u$ to investigate synaptic transmission and frequency filtering at individual Schaffer collateral boutons.

For all tested variants, synaptic off-kinetics were slower by a factor of 2.5 - 3.8 compared to temperature-matched in vitro measurements on isolated protein. This is consistent with the much higher affinities of HEK293T cell-expressed glutamate sensors compared to soluble protein. These systematic differences, also noted in the original characterization of iGluSnFR (Marvin et al., 2013), may be attributed to the tethering of the molecule to a membrane anchor, slowing down conformational changes compared to free-floating sensor molecules. Nevertheless, the relative differences in affinity and kinetics of the new versions compared to iGluSnFR were preserved in vitro and in situ. The on- and off-rates of $iGlu_u$ are greater (2- and 5-6 fold, respectively) compared to iGluSnFR. Interestingly, $iGlu_u$ was a faster reporter in the hippocampal slice than $iGlu_f$, even though the latter has a faster limiting on-rate. $iGlu_u$ may be put at an advantage over $iGlu_f$ by its concentration-independent response

kinetics. It must be noted that the kinetics of iGluSnFR-type indicators are ultimately limited by the structural change that reconstitutes the fluorescent complex, similar to calcium-sensing GCaMPs. The constraints of the mechanism with regard to the onset of fluorescence suggest that it cannot be engineered to resolve sub-millisecond glutamate dynamics. To achieve microsecond response times, it might be necessary to develop hybrid glutamate indicators using synthetic dyes.

Synaptic $iGlu_u$ imaging revealed complete clearance of glutamate between release events even at 100 Hz stimulation frequency. The first attempts to estimate the time course of synaptic glutamate transients were based on the decay of NMDA receptor responses in primary cell culture: Kinetic analysis of the displacement of a competitive NMDA receptor antagonist suggested glutamate clearance with τ = 1.2 ms (Clements et al., 1992). More recent studies using computational modeling and fluorescence anisotropy imaging in tissue suggest that it is closer to 100 µs (Beato and Scimemi 2009; Zheng et al. 2017). Thus, due to the intrinsic kinetic limits of the iGluSnFR mechanism, even $iGlu_u$ cannot resolve the true dynamics of free glutamate in the synaptic cleft. What we can say with confidence is that accumulation of glutamate in the synaptic cleft does not contribute to short-term plasticity at Schaffer collateral synapses.

In our analysis of synaptic responses, we did not correct for the non-linearity of the iGluSnFR variants (Figure 16c), as response amplitudes (40% - 120% $\Delta F/F_0$) were typically less than half of the maximum change in fluorescence determined for the three indicators (Table 3). For a more detailed analysis of variations in cleft glutamate concentration (optical quantal analysis) at high release probability boutons, however, partial iGluSnFR saturation during large responses (up to 280% $\Delta F/F_0$) would have to be taken into account (Figure 21). Glutamate release showed strong depression during 100 Hz firing, in line with the expected depletion of release-ready vesicles. As we controlled the generation of every action potential by somatic current injections, we can exclude decreased afferent excitability as a source of

depression in these experiments (Kim et al., 2012). AMPA receptor currents during 100 Hz firing did not show more run-down than $iGlu_u$ responses, suggesting that AMPA receptor desensitization did not play a major role in the decrease of synaptic efficacy during the train. Paradoxically, AMPA responses were fully recovered 500 ms after the train while the $iGlu_u$ response was still significantly depressed. The most parsimonious explanation is a long-lasting depression of glutamate release. There are alternative scenarios that could explain smaller $iGlu_u$ responses on the 11th pulse, e.g. indicator molecules retrieved into endosomal structures during endocytosis, or accumulation of indicator in a (hypothetical) desensitized state. In these scenarios, facilitating boutons, which experience more exo- and endocytosis and $iGlu_u$ activation during the train, would be expected to show smaller responses at the 11th pulse. However, we found a strong correlation in the opposite direction, making these scenarios less likely (Figure 18g).

The full recovery of the AMPA response points to an unexpected increase in sensitivity of the postsynaptic compartment to glutamate. By association with different auxiliary proteins and other scaffold-related mechanisms, the density and open probability of postsynaptic glutamate receptors can quickly change (Compans, Choquet and Hosy 2016; Carbone and Plested, 2016). In hippocampal slice cultures, post-tetanic potentiation is well established and requires the activity of protein kinase C (Brager et al., 2003). Thus, it is possible that elevated Ca^{2+} levels in the spine during our high frequency protocol enhanced AMPA receptor currents by a number of mechanisms, compensating for the reduced glutamate release 500 ms after the tetanus.

The surprisingly tight correlation between paired-pulse facilitation and rapid recovery from depression at individual boutons provides direct evidence that differential use of presynaptic resources determines the neural code between pyramidal cells (Tsodyks and Markram, 1997; Markram et al., 1998). Using Schaffer collateral synapses as an example, we show that $iGlu_u$ is a useful tool for a mechanistic analysis of high frequency synaptic

transmission, interrogating presynaptic function independently of postsynaptic transmitter receptors.

3.8.5 Methods

We provide a detailed description of the methods, data analysis and kinetic modeling in the on-line Supplemental Information.

Materials. pCMV(MinDis).iGluSnFR and pRSET FLIPE-600n plasmids were a gift from Loren Looger (Addgene Plasmid #41732) and Wolf Frommer (Addgene plasmid # 13537), respectively. Site-directed mutagenesis was carried out following the QuikChange II XL protocol (Agilent Technologies).

Fluorescence spectroscopies. Glutamate association and dissociation kinetic experiments of iGluSnFR proteins were carried out on a Hi-Tech Scientific SF-61DX2 stopped-flow system equipped with a temperature manifold (Walklate and Geeves, 2015). Fluorescence spectra and equilibrium glutamate titrations were recorded on a Fluorolog3 (Horiba Scientific).

In situ glutamate titration. HEK293T cells were cultured on 24-well glass bottom plates in DMEM containing non-essential amino-acids (Life Technologies), 10% heat inactivated FBS (Life Technologies) and penicillin/streptomycin (100 U/ml, 100 mg/ml, respectively), at 37°C in an atmosphere of 5% CO_2. Cells were allowed 24 h to adhere before transfection with Lipofectamine 2000 (Invitrogen). Cells were examined at 37°C (OKO lab incubation chamber) with a 3i Marianas spinning-disk confocal microscope equipped with a Zeiss AxioObserver Z1, a 40x/NA1.3 oil immersion objective and a 3i Laserstack as excitation light source (488 nm).

Synaptic measurements. Organotypic hippocampal slices (400 µm) were prepared from male Wistar rats at postnatal day 5 as described (Gee et al., 2017). iGluSnFR and variant

plasmids were electroporated into 2-3 CA3 pyramidal cells at 40 ng/µl (iGluSnFR) or 50 ng/µl ($iGlu_f$, $iGlu_u$) together with tdimer2 (20 ng/µl), a cytoplasmic red fluorescent protein (Wiegert et al., 2017). 2 - 4 days after electroporation (at DIV 14-30), slice cultures were placed in the recording chamber of a two-photon microscope and superfused with artificial cerebrospinal fluid (ACSF) containing (in mM) 25 $NaHCO_3$, 1.25 NaH_2PO_4, 127 NaCl, 25 D-glucose, 2.5 KCl, 2 $CaCl_2$, 1 $MgCl_2$. Whole-cell recordings from a transfected CA3 pyramidal cell were made with a Multiclamp 700B amplifier (Molecular Devices). Red and green fluorescence was detected through the objective (LUMPLFLN 60XW, 60x, NA 1.0, Olympus) and through the oil immersion condenser (NA 1.4, Olympus) using 2 pairs of photomultiplier tubes (H7422P-40SEL, Hamamatsu).

3.8.6 Supplementary information

Materials. pRSET FLIPE-600n and pCMV(MinDis).iGluSnFR plasmids were a gift from Loren Looger (Addgene Plasmid #41732) and Wolf Frommer (Addgene plasmid # 13537), respectively. pET41a and pET30b vectors were obtained from Novagen. *E. coli* XL10-Gold and BL21 (DE3) Gold cells were purchased from Invitrogen. Restriction enzymes were obtained from New England Biolabs and T4 DNA ligase from Fermentas.

Cloning of glutamate binding proteins into bacterial expression vectors. The *iGluSnFR* gene was subcloned from pCMV(MinDis).iGluSnFR by restriction-ligation into pET41a (GST-fusion expression vector) at BglII and NotI restriction sites and *ybeJ* encoding GluBP was subcloned from pRSET FLIPE 600n (ECFP-ybeJ-Venus) into pET30b (His-fusion expression vector) at BglII and NotI restriction sites.

Site-directed mutagenesis of iGluSnFR. A series of DNA mutations were performed on pET41a-iGluSnFR. Site-directed mutagenesis was carried out following the QuikChange II XL protocol (Agilent Technologies) using the following primers (5'→3'):

R25K, GGTGTGATTGTCGTCGGTCACAAGGAATCTTCAGTGCCTTTCTCT;

E26A, GTCGTCGGTCACCGTGCATCTTCAGTGCCTTTC;

E26D, GATTGTCGTCGGTCACCGTGATTCTTCAGTGCC;

E26R, GATTGTCGTCGGTCACCGTAGATCTTCAGTGCCTTTCTCT;

S73T, GTAAAACTGATTCCGATTACCACGCAAAACCGTATTCCACTGCTG;

T93A, TTGAATGTGGTTCTACCGCCAACAACGTCGAACGC;

Mutations were confirmed by DNA sequencing (Genewiz).

Expression and purification of genetically encoded glutamate indicator (GEGI) proteins. His-tagged GluBP, GST-fused iGluSnFR and variant proteins were overexpressed in *E. coli* BL21 (DE3) Gold cells. Cells were grown at 37 °C and expression was induced overnight at 20 °C in the presence of 0.5 mM isopropyl thio-β-D-galactoside (IPTG). Cells were resuspended in 50 mM Na^+-HEPES, 200 mM NaCl, pH 7.5 containing one tablet of Complete protease inhibitor cocktail (Roche, Basel, Switzerland) and lysed by sonication on ice (VibraCell, Jencons PLS). For GST-fused proteins, clarified lysates were purified by a single-step GST chromatography (GSTrap, ÄKTA Purifier, GE Healthcare) at 4 °C. The purified protein was eluted in 50 mM Na^+-HEPES, 200 mM NaCl, 10 mM reduced glutathione, pH 7.5. For His-tagged GluBP clarified lysate was purified on a NiNTA column (QIAGEN, ÄKTA Purifier, GE Healthcare) at 4 °C. The purified protein was eluted with a linear gradient of 0-0.5 M imidazole. Purity was assessed by SDS-PAGE (gradient of 6.4% - 20% acrylamide/bisacrylamide) and aliquoted fractions were dialyzed against 50 mM Na^+-HEPES, 200 mM NaCl, pH 7.5 and stored at -80 °C.

Measuring protein concentrations. iGluSnFR and GluBP proteins were highly purified, allowing protein concentration to be determined spectroscopically. The absorption spectra of all iGluSnFR proteins comprised three peaks at wavelengths 280 nm, 400 nm and 497 nm. Protein concentrations were determined with molar extinction coefficients (ε_o) at 280 nm calculated from the amino acid composition using a Nanodrop 1000 spectrophotometer (Thermo Scientific). $\varepsilon_{o(280)}$ of 90690 $M^{-1}cm^{-1}$ for GST-iGluSnFR and 24075 $M^{-1}cm^{-1}$ for His-GluBP was calculated (Gill and von Hippel, 1989).

Equilibrium binding titrations for iGluSnFR proteins. Glutamate affinity assays of iGluSnFR proteins were performed by continuous titration using an automated syringe pump (ALADDIN 1000, WPI). iGluSnFR and variants at 50-100 nM concentration (50 mM Na^+-HEPES, 100 mM NaCl, 2 mM $MgCl_2$, pH 7.5 at 20°C) were titrated with an appropriate stock solution of glutamate at a 10 μL/min flow rate in a stirred 3 mL cuvette. Fluorescence was measured at 492 nm excitation and 512 nm emission wavelengths using a Fluorolog3 spectrofluorimeter (Horiba Scientific). Fluorescence records were corrected for dilution and photobleaching (0.1%/min). Data were normalized and expressed as bound fraction and glutamate dissociation constant (K_d) and cooperativity (n) were obtained by fitting the data to the Hill equation using GraphPad Prism 7 software. All titrations were performed at least in triplicates and expressed as mean ± SEM. Ligand binding specificity was assessed by titrating iGluSnFR proteins as described above with L-aspartate, L-glutamine, D-serine, GABA and glycine.

Stopped-flow fluorimetry. Glutamate association and dissociation kinetic experiments of iGluSnFR proteins were carried out on a Hi-Tech Scientific SF-61DX2 stopped-flow

system equipped with a temperature manifold (Walklate and Geeves, 2015) in the 4 °C to 34 °C temperature range, as specified. Fluorescence excitation was set to 492 nm. Fluorescence emission was collected using a 530 nm cut-off filter. At least 3 shots from 3 replicates were averaged for analysis. Data were fitted to a single exponential to obtain the fluorescence rise or decay rate using KinetAssyst software (TgK scientific).

Association kinetics. The solution containing 1 μM protein in 50 mM Na^+-HEPES, 100 mM NaCl, 2 mM $MgCl_2$, pH 7.5 was rapidly mixed (1:1) with 50 mM Na^+-HEPES, 100 mM NaCl, 2 mM $MgCl_2$, pH 7.5 containing increasing glutamate concentrations (concentrations given are those in the mixing chamber). For the determination of temperature dependence of glutamate association rates, protein samples at 1 μM concentration were mixed as above to give a final glutamate concentration of 1 mM for iGluSnFR, 5 mM for iGluSnFR E26D ($iGlu_f$) and 10 mM for iGluSnFR S73T ($iGlu_u$) in the mixing chamber.

Dissociation kinetics. The solution containing 1 μM protein in 50 mM Na^+-HEPES, 100 mM NaCl, 2 mM $MgCl_2$, pH 7.5 with saturating glutamate (15 x K_d) was rapidly mixed (1:1) with 0.67 mM GluBP in 50 mM Na^+-HEPES, 100 mM NaCl, 2 mM $MgCl_2$, pH 7.5 (concentrations in the mixing chamber). For the determination of temperature dependence of glutamate dissociation rates, protein samples at 1 μM concentration were premixed to give a final glutamate concentration of 0.2 mM for iGluSnFR, 0.5 mM for $iGlu_f$ and 1 mM for $iGlu_u$ in the mixing chamber.

pH sensitivity of iGluSnFR, $iGlu_f$ and $iGlu_u$ proteins. To determine the apparent pK_a for iGluSnFR proteins, a series of buffers were prepared. Depending on their respective pH

buffering range, appropriate buffer was used for the measurements (MES for pH 6 - 6.5, HEPES for pH 7 - 8, Tris for pH 8.5 - 9 and CAPS for pH 10). The pH titrations were performed by recording fluorescence spectra in glutamate-free (50 mM Na^+-buffer, 100 mM NaCl, 2 mM $MgCl_2$) or glutamate-saturated (50 mM Na^+-buffer, 100 mM NaCl, 2 mM $MgCl_2$, 1 - 10 mM glutamate) using 1 µM protein in 0.5 pH unit intervals (Fluorolog3, Horiba). Final glutamate concentrations were 1 mM for iGluSnFR, 2 mM for $iGlu_f$ and 10 mM for $iGlu_u$.

Quantum yield determination. The concentration of iGluSnFR proteins was adjusted such that the absorbance at the excitation wavelength (492 nm) was between 0.001 and 0.04. A series of dilutions was prepared in a buffered solution (50 mM Na^+-HEPES, 100 mM NaCl, 2 mM $MgCl_2$, pH 7.5 with either no glutamate or 1 - 10 mM glutamate. Final glutamate concentrations were 1 mM for iGluSnFR, 2 mM for $iGlu_f$ and 10 mM for $iGlu_u$. Fluorescence spectra were recorded on a Fluorolog3 (Horiba Scientific). GCaMP6f quantum yield measured in Ca^{2+}-saturated buffer was used as a reference ($\Phi_{+Ca}2+ = 0.59$) (Chen et al., 2013). Data were plotted as integrated fluorescence intensity as a function of absorbance and fitted to a linear regression with slope S. Quantum yield for iGluSnFR proteins was obtained using the following equation:

$$\Phi_{protein} = \Phi_{GCaMP6f} \times (S_{protein}/S_{GCaMP6f}).$$

In situ glutamate titration. HEK293T cells were cultured on 24-well glass bottom plates in DMEM containing non-essential amino-acids (Life Technologies), 10% heat inactivated FBS (Life Technologies) and penicillin/streptomycin (100 U/ml, 100 mg/ml, respectively), at 37 °C in an atmosphere of 5% CO_2. Cells were allowed 24 h to adhere before transfection

with Lipofectamine 2000 (Invitrogen) following the manufacturer's recommendations (1.5 µL Lipofectamine 2000 and 0.5 µg plasmid DNA in 50 µL OptiMEM (Life Technologies)) and maintained for 24 h before being used in experiments. HEK293T cells transfected with iGluSnFR, $iGlu_f$ or $iGlu_u$ were washed with PBS and imaged in 20 mM Na^+-HEPES, 145 mM NaCl, 10 mM glucose, 5 mM KCl, 1 mM $MgCl_2$, 1 mM NaH_2PO_4, pH 7.4. Cells were examined at 37 °C (OKO lab incubation chamber) with a 3i Marianas spinning-disk confocal microscope equipped with a Zeiss AxioObserver Z1, a 40x/NA1.3 oil immersion objective and a 3i Laserstack as excitation light source (488 nm). Emitted light was collected through a 525/30 nm BrightLine® single-band bandpass filter (Yokogawa CSU-X filter wheel) onto a CMOS camera (Hamamatsu, ORCA Flash 4.0; 1152x1656 pixels). Glutamate titrations were carried out using 0 - 10 mM L-glutamate (final concentration). Regions of interest (ROI) were defined by ellipses along each cell membrane. A single ROI was analyzed in each cell. ImageJ was used to process the images. GraphPad Prism 7 was used to plot and fit data with the Hill equation. The number of cells analyzed (n) were between 19 and 41, as specified. Data was expressed as mean ± SEM.

Organotypic slice cultures and single cell electroporation. Organotypic hippocampal slices were prepared from male Wistar rats at post-natal day 5 as described (Gee et al., 2017). Briefly, dissected hippocampi were cut into 400 µm slices with a tissue chopper and placed on a porous membrane (Millicell CM, Millipore). Cultures were maintained at 37 °C, 5% CO_2 in a medium containing 80% MEM (Sigma M7278), 20% heat-inactivated horse serum (Sigma H1138) supplemented with 1 mM L-glutamine, 0.00125% ascorbic acid, 0.01 mg/ml insulin, 1.44 mM $CaCl_2$, 2 mM $MgSO_4$ and 13 mM D-glucose. No antibiotics were added to the culture medium. DNA encoding iGluSnFR and tdimer2 were subcloned into a mammalian expression vector (pCI) under the control of the neuron-specific human

synapsin1 promoter. $iGlu_f$ and $iGlu_u$ were generated by site-directed mutagenesis of pCI-synapsin-iGluSnFR using the oligonucleotides for the E26D ($iGlu_f$) and S73T ($iGlu_u$) mutations. Individual CA3 pyramidal cells were transfected by single-cell electroporation (Wiegert et al., 2017). iGluSnFR and variant plasmids were electroporated at 40 ng/µl (iGluSnFR) or 50 ng/µl ($iGlu_f$, $iGlu_u$) along with a cytoplasmic red fluorescent protein tdimer2 (20 ng/µl). During electroporation slices were kept in 10 mM Na^+-HEPES, 145 mM NaCl, 25 mM D-glucose, 1 mM $MgCl_2$ and 2 mM $CaCl_2$, pH 7.4.

Electrophysiology. Experiments were performed between DIV 14-30 (2 - 4 days after electroporation). Hippocampal slice cultures were placed in the recording chamber of the microscope and superfused with artificial cerebrospinal fluid (ACSF) containing 25 mM $NaHCO_3$, 1.25 mM NaH_2PO_4, 127 mM NaCl, 25 mM D-glucose, 2.5 mM KCl and (saturated with 95% O_2 - 5% CO_2), 2 mM $CaCl_2$ and 1 mM $MgCl_2$. Whole-cell patch clamp recordings from a transfected CA3 pyramidal neurons were performed with a Multiclamp 700B amplifier (Molecular Devices) under the control of Ephus software written in MATLAB (Suter et al., 2010). CA3 neurons were held in current clamp and stimulated through the patch pipette by brief electrical pulses (2 - 3 ms and 1500 - 3500 pA current injection) to induce single action potentials. Analog signals were filtered at 6 kHz and digitized at 10 kHz. Patch pipettes with a tip resistance of 3.5 to 4.5 MΩ were pulled with a Narishige PC-10 vertical puller and filled with 10 mM K^+-HEPES, 135 mM K^+-gluconate, 4 mM $MgCl_2$, 4 mM Na^+_2-ATP, 0.4 mM Na^+-GTP, 10 mM Na^+_2-phosphocreatine and 3 mM ascorbate (pH 7.2). Slice experiments were performed at 34°C ± 1°C by controlling the temperature of the ACSF with an in-line heating system and the oil immersion condenser with a Peltier element. Dual patch experiments and $iGlu_u$ measurements (Figure 18) were done under NMDAR block (10 µM CPP-ene) to prevent induction of long-term plasticity during high frequency stimulation.

Two-photon microscopy and data analysis. The custom-built two-photon imaging setup was based on an Olympus BX51WI microscope controlled by a customized version the open-source software package ScanImage (Pologruto et al., 2003) written in MATLAB (MathWorks). We used a pulsed Ti:Sapphire laser (MaiTai DeepSee, Spectra Physics) tuned to 980 nm wavelength to simultaneously excite both the cytoplasmic tdimer2 and the membrane bound iGluSnFR. Red and green fluorescence was detected through the objective (LUMPLFLN 60XW, 60x, NA 1.0, Olympus) and through the oil immersion condenser (NA 1.4, Olympus) using 2 pairs of photomultiplier tubes (PMTs, H7422P-40SEL, Hamamatsu). 560 DXCR dichroic mirrors and 525/50 and 607/70 emission filters (Chroma Technology) were used to separate green and red fluorescence. Excitation light was blocked by short-pass filters (ET700SP-2P, Chroma). ScanImage was modified for the user to freely define the scanning path. Signals from iGluSnFR and fast variants were measured by repeatedly scanning a spiral line across the bouton to maximize the signal-to-noise ratio. iGluSnFR signals were sampled at 500 Hz and $iGlu_f$ and $iGlu_u$ signals were sampled either at 500 Hz or 1 kHz.

A spiral scan covering the entire bouton may hit the diffusing cloud of glutamate just once or several times per line (Figure 16l). We had no prior knowledge about the precise location of fusion events on the bouton surface (Figure 16k). To maximize the signal-to-noise ratio in every trial, we assigned a dynamic region of interest (ROI): pixel columns (i.e. spatial positions) were sorted according to the change in fluorescence (ΔF) in each column (Figure 21). The peak amplitudes were extracted from the average of 10 trials acquired at 0.1 Hz (Figure 18). To avoid bleach-related run-down during the train, we normalized each of the 11 peaks by a baseline measurement (F_0) taken just 1 ms before. This strategy was possible since the inter-stimulus interval was 10 ms (500 ms for pulse #11) and τ_{off} was 2.6 ms. For the peak amplitude measurement of postsynaptic AMPA responses (Figure 18a), we repeated the protocol 70 - 100 times at 0.1 Hz and manually removed trials in which the CA1

neuron received spontaneous synaptic input. In addition, we discarded trials where the patch-clamped CA3 neuron failed to spike in response to a somatic current injection, and averaged the remaining trials. The decay time course of the recovery action potential was fitted with a mono-exponential decay function. This decay time constant was then used to extract the amplitude of individual responses during the 100 Hz train by deconvolution. Analysis was done in MATLAB and GraphPad Prism.

Data analysis and kinetic modelling. Biophysical experiments were performed at least in triplicates and analysed using GraphPad Prism 7 and KinetAsyst (TgK Scientific) software. Experiments on HEK293T cells were carried out on three independent cultures each. The total number of cells analysed in each condition is given in the figure legends. The software package IBS (http://ibs.biocuckoo.org) was used to display the domain structure glutamate sensors. The PyMOL Molecular Graphics System (2002) by W. L. Delano (https://www.pymol.org/ RRID: SCR_000305) was employed for displaying the crystal structure. Global fitting to kinetic data was performed using DynaFit4 software (http://www.biokin.com/dynafit RRID: SCR_008444) according to the Schemes 1 & 2.

Kinetic theory. iGluSnFR is represented as $iGlu_l$~$iGlu_s$, indicating that the N-terminally flanking large GluBP fragment (GluBP 1-253, $iGlu_l$) and the C-terminally fused small GluBP fragment (GluBP 254-279, $iGlu_s$) are within one molecule but separated by the interjecting cpEGFP.

Scheme 1:

$$iGlu_l{\sim}iGlu_s + Glu \underset{k_{-1}}{\overset{k_{+1}}{\rightleftharpoons}} Glu.iGlu_l{\sim}iGlu_s \underset{k_{-2}}{\overset{k_{+2}}{\rightleftharpoons}} Glu.iGlu_c^*$$

Glutamate binds to the large domain $iGlu_i$ of GluBP. This is a pre-equilibrium that is described by the following equation:

(1) $\frac{\partial[Glu.iGlu_l{\sim}iGlu_s]}{\partial t} = k_{+1}[iGlu_l{\sim}iGlu_s][Glu] - k_{-1}[Glu.iGlu_l{\sim}iGlu_s]$

With the equilibrium constant defined as:

(2) $K_1 = \frac{k_{+1}}{k_{-1}}$

The total concentration of iGluSnFR, $[iGluSnFR]_0$ is the sum of all iGluSnFR complexes involved in the scheme.

(3) $[iGluSnFR]_0 = [iGlu_l{\sim}iGlu_s] + [Glu.iGlu_l{\sim}iGlu_s] + [Glu.iGlu_c^*]$

From this term $[iGlu_i{\sim}iGlu_s]$ is derived as:

(4) $[iGlu_l{\sim}iGlu_s] = [iGluSnFR]_0 - [Glu.iGlu_l{\sim}iGlu_s] - [Glu.iGlu_c^*]$

If steady-state is assumed for the glutamate-bound iGluSnFR ($Glu.iGlu_l{\sim}iGlu_s$) then eq. 1 equals zero and we can insert eq. 4 to obtain a term for $[Glu.iGlu_l{\sim}iGlu_s]$.

(5) $[Glu.iGlu_l{\sim}iGlu_s] = \frac{K_1[Glu]}{1+K_1} \cdot ([iGluSnFR]_0 - [Glu.iGlu_c^*])$

The formation of the fluorescent state $[Glu.iGlu_c^*]$ is defined by:

(6) $\frac{\partial[Glu.iGlu_c^*]}{\partial t} = k_{+2}[Glu.iGlu_l{\sim}iGlu_s] - k_{-2}[Glu.iGlu_c^*]$

Inserting eq. 5 into eq. 6 and performing a partial differentiation leads to:

(7) $k_{obs} = \frac{k_{+2}K_1[Glu]}{1+K_1[Glu]} + k_{-2}$

With the amplitude A, the $K_{overall}$ and K_d defined as:

(8a,b,c)

$$A = \frac{k_{+2}K_1[Glu][iGluSnFR]_0}{1+K_1[Glu]}$$

$$K_{overall} = K_1(1 + K_2)$$

$$K_d = \frac{1}{K_o} = \frac{1}{K_1+K_1K_2}$$

Scheme 2:

$$iGlu_l{\sim}iGlu_s \underset{k_{-3}}{\overset{k_{+3}}{\rightleftharpoons}} iGlu_c^* + Glu \underset{k_{-4}}{\overset{k_{+4}}{\rightleftharpoons}} Glu.iGlu_c^*$$

$iGlu_l{\sim}iGlu_s$ first forms the complete state $iGlu_c^*$ that is fluorescent. The pre-equilibrium can be defined as:

(9) $\frac{\partial[iGlu_c^*]}{\partial t} = k_{+3}[iGlu_l{\sim}iGlu_s] - k_{-3}[iGlu_c^*]$

With the equilibrium constant defined as:

(10) $K_3 = \frac{k_{+3}}{k_{-3}}$

The total concentration of iGluSnFR, $[iGluSnFR]_0$ is the sum of all iGluSnFR complexes involved in the scheme.

(11) $[iGluSnFR]_0 = [iGlu_l{\sim}iGlu_s] + [iGlu_c^*] + [Glu.iGlu_c^*]$

From this term $[iGlu_i{\sim}iGlu_s]$ is derived as:

(12) $[iGlu_l{\sim}iGlu_s] = [iGluSnFR]_0 - [iGlu_c^*] - [Glu.iGlu_c^*]$

If steady-state is assumed for ($iGlu_c^*$) then eq. 9 equals zero and we can insert eq. 12 to obtain a term for [$iGlu_c^*$].

(13) $[iGlu_c^*] = \frac{K_3}{1+K_3} \cdot ([iGluSnFR]_0 - [Glu.iGlu_c^*])$

The formation of the fluorescent state [$Glu.iGlu_c^*$] is defined by:

(14) $\frac{\partial[Glu.iGlu_c^*]}{\partial t} = k_{+4}[iGlu_c^*][Glu] - k_{-4}[Glu.iGlu_c^*]$

Inserting eq. 13 into eq. 14 and performing a partial differentiation leads to:

(15) $k_{obs} = \frac{k_{+4}K_3[Glu]}{1+K_3} + k_{-4}$

With the amplitude A, the $K_{overall}$ and K_d defined as:

(16a,b,c)

$$A = \frac{k_{+4}K_3[Glu][iGluSnFR]_0}{1+K_3}$$

$$K_{overall} = K_3(1+K_4)$$

$$K_d = \frac{1}{K_o} = \frac{1}{K_3+K_3K_4}$$

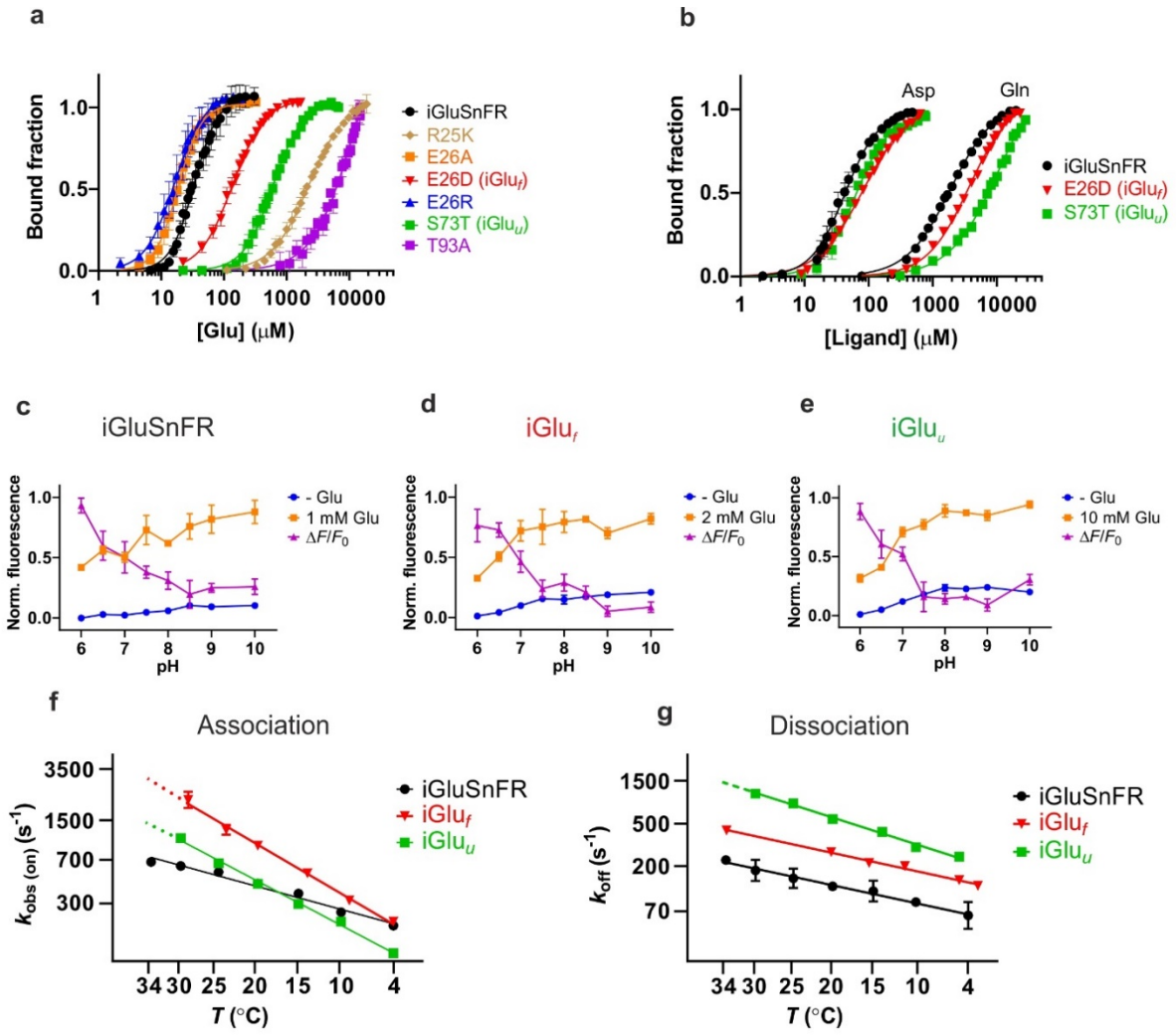

Figure 20: Biophysical characterization of iGluSnFR variants

a) Equilibrium glutamate binding titrations at 20 °C for iGluSnFR (●), iGluSnFR E26D (iGlu$_f$) (▼), iGluSnFR S73T (iGlu$_u$) (■), iGluSnFR E26R (▲), iGluSnFR E26A (■), iGluSnFR R25K (♦), iGluSnFR T93A (■). Fluorescence changes are normalized to F_0 of 0 and F_{max} of 1. **b)** Ligand selectivity. Equilibrium titration of iGluSnFR (●), iGlu$_f$ (▼) and iGlu$_u$ (■) with aspartate and glutamine, as indicated. pH sensitivity and pK_a determination of **(c)** iGluSnFR; **d)** iGlu$_f$; **e)** iGlu$_u$. Normalized fluorescence in the presence of glutamate (■) (concentration as specified), or in the absence of glutamate (●); $\Delta F/F_0$ (▲). **f)** Arrhenius plots of the limiting *on*-rates of iGluSnFR, iGlu$_f$ and iGlu$_u$. Values at 34 °C for iGlu$_f$ and iGlu$_u$ are extrapolated assuming the measured slope. **g)** Arrhenius plot of the dissociation rate constants of iGluSnFR, iGlu$_f$ and iGlu$_u$. The value for iGlu$_u$ 34 °C is extrapolated assuming the measured slope.

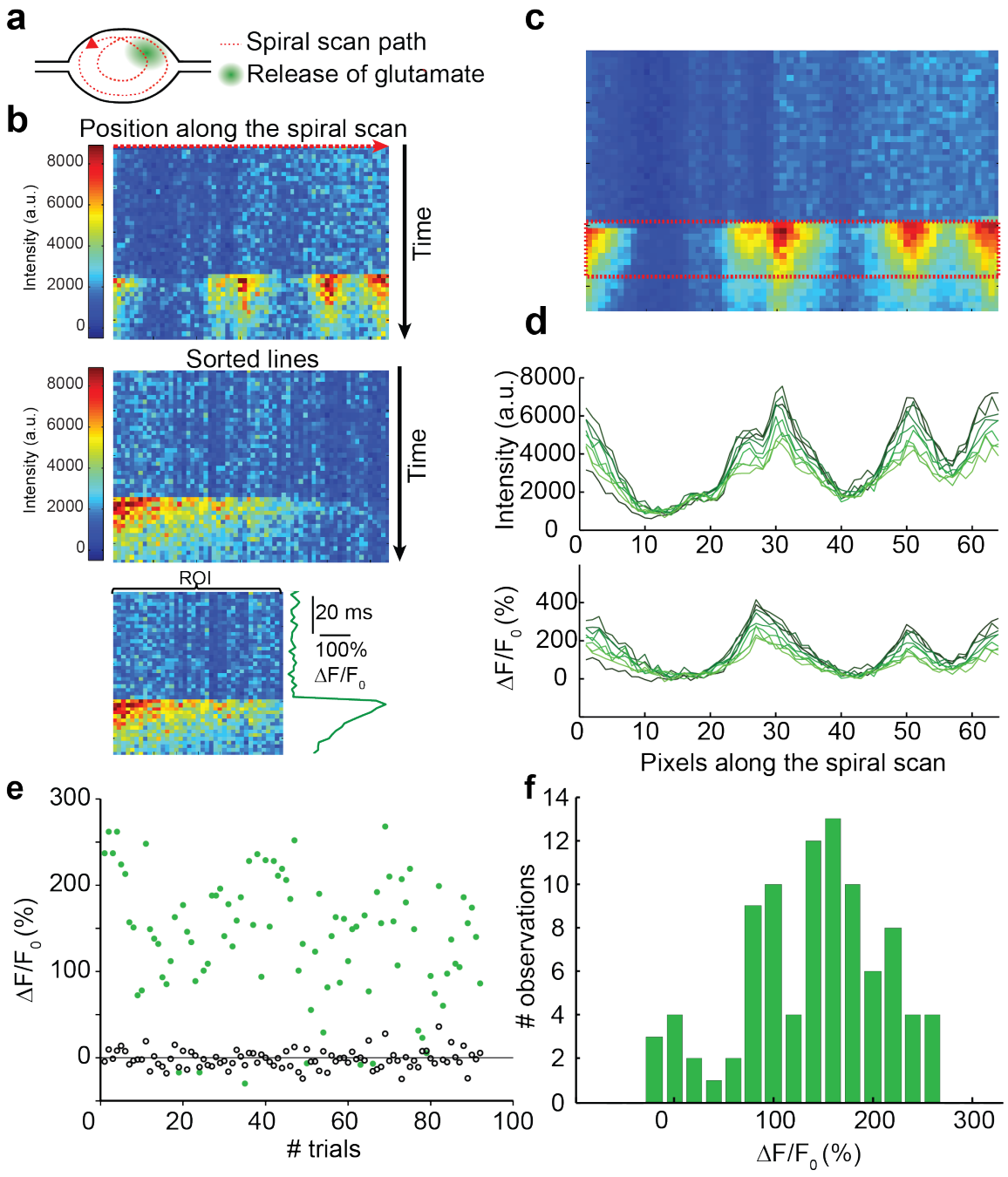

Figure 21: Extraction of amplitudes from spiral scans

a) Spiral scan intersecting site of vesicular fusion. **b)** Spiral scan, single trial response. Columns were sorted according to the signal amplitude (ΔF). The region of interest (ROI) was defined as the columns with ΔF > 50% of max ΔF (63.2% of max for $iGlu_u$). **(c)** Average of 10 trials (single APs) to analyze lateral spread of signal (red box). **d)** Decay of fluorescence transient (9 scan lines = 18 ms). Note lack of lateral spread of the signal due to slow diffusion of membrane-anchored iGluSnFR. **e)** iGluSnFR responses from a single Schaffer collateral bouton plotted over time. Green circles: Single action potential stimulation. Open circles: No

stimulation. Note clear separation of successes and failures. **f)** Histogram of response amplitudes (same data as panel a) shows multiple peaks, possibly due to multi-vesicular release events.

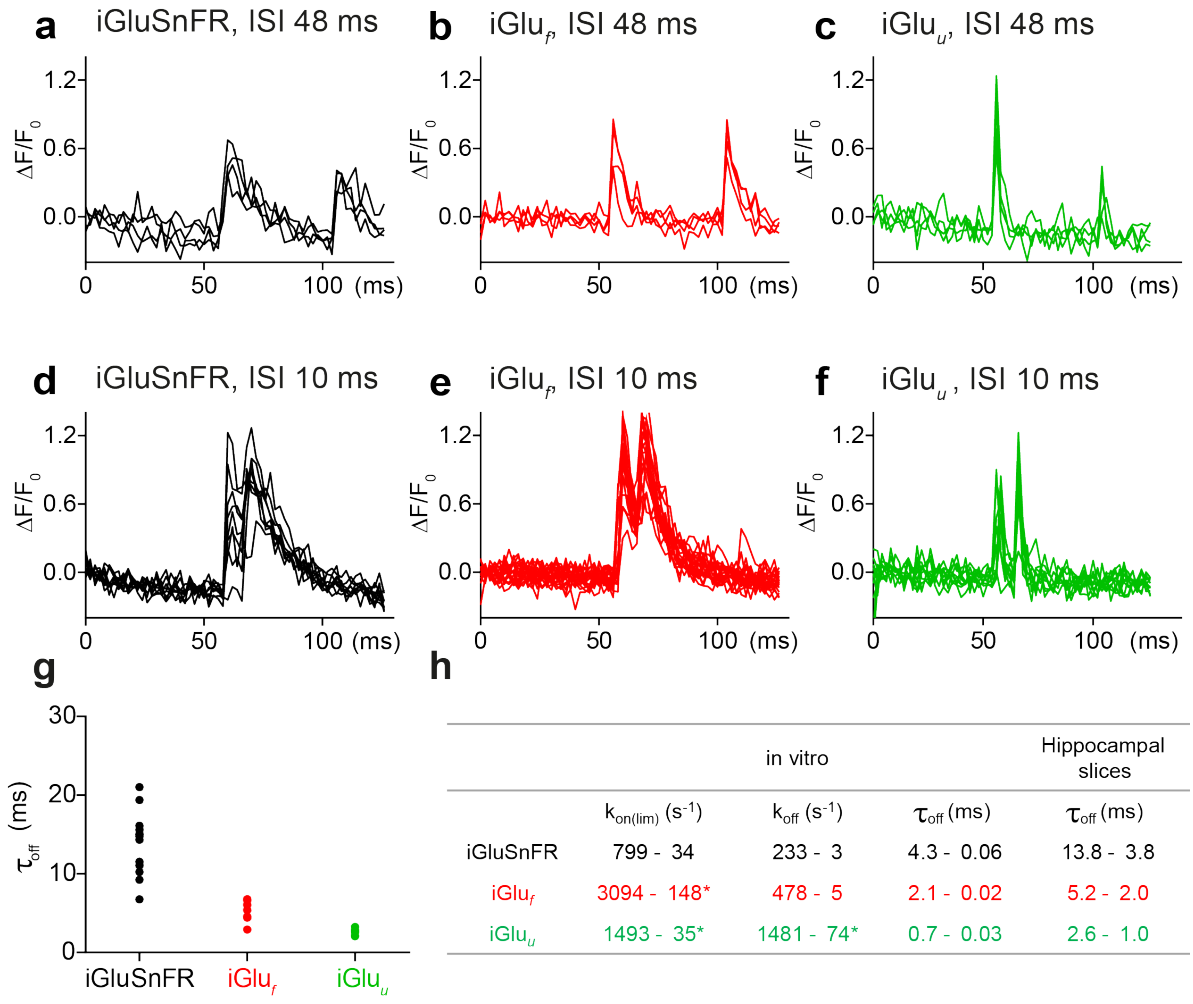

	in vitro			Hippocampal slices
	$k_{on(lim)}$ (s^{-1})	k_{off} (s^{-1})	τ_{off} (ms)	τ_{off} (ms)
iGluSnFR	799 - 34	233 - 3	4.3 - 0.06	13.8 - 3.8
iGlu$_f$	3094 - 148*	478 - 5	2.1 - 0.02	5.2 - 2.0
iGlu$_u$	1493 - 35*	1481 - 74*	0.7 - 0.03	2.6 - 1.0

Figure 22: Paired-pulse stimulation and decay time measurements

a, b, c) Fluorescence time course ($\Delta F/F_0$) in single boutons expressing iGluSnFR, iGlu$_f$ and iGlu$_u$, respectively stimulated by a somatic paired pulse (48 ms ISI). **d, e, f)** Fluorescence time course ($\Delta F/F_0$) of single boutons expressing iGluSnFr, iGlu$_f$ and iGlu$_u$, respectively stimulated by a somatic paired pulse (10 ms ISI). **g)** Decay time constant τ_{off} measured in hippocampal slices at 34 ºC for iGluSnFR (n = 13, 500 Hz sampling rate), iGlu$_f$ (n = 7, 1 kHz sampling rate) and iGlu$_u$ (n = 7, 1 kHz sampling rate). **h)** Summary of on- and off-rates *in vitro* and decay times measured *in vitro* and in hippocampal slices at 34 ºC. Values are given as mean ± SEM. Values marked by * are extrapolated from the Arrhenius plot.

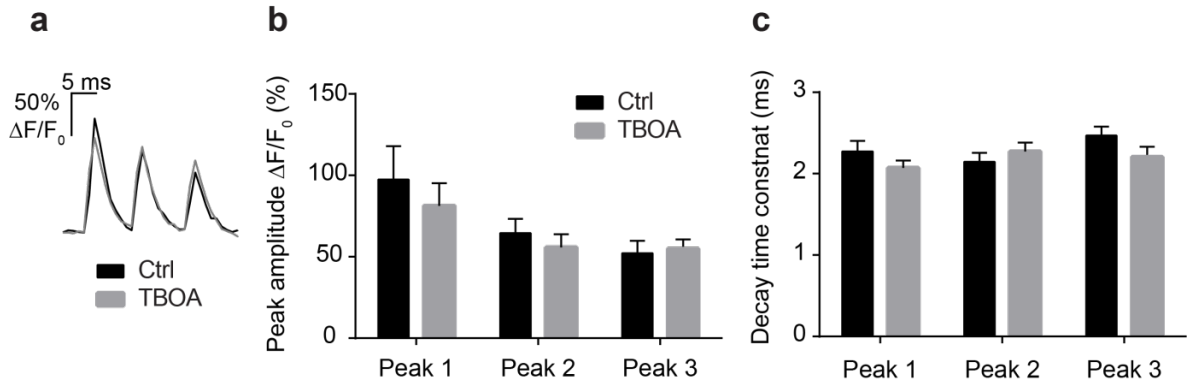

Figure 23: Testing the effect of glutamate uptake blocker TBOA on synaptic iGlu$_u$ transients

a) Average traces (iGlu$_u$) from single Schaffer collateral bouton stimulated at 100 Hz, before and after wash-in of TBOA (40 µM). **b)** Peak amplitude was not affected by TBOA (*n* = 10 boutons). **c)** Decay kinetics was not affected by TBOA (*n* = 10 experiments).

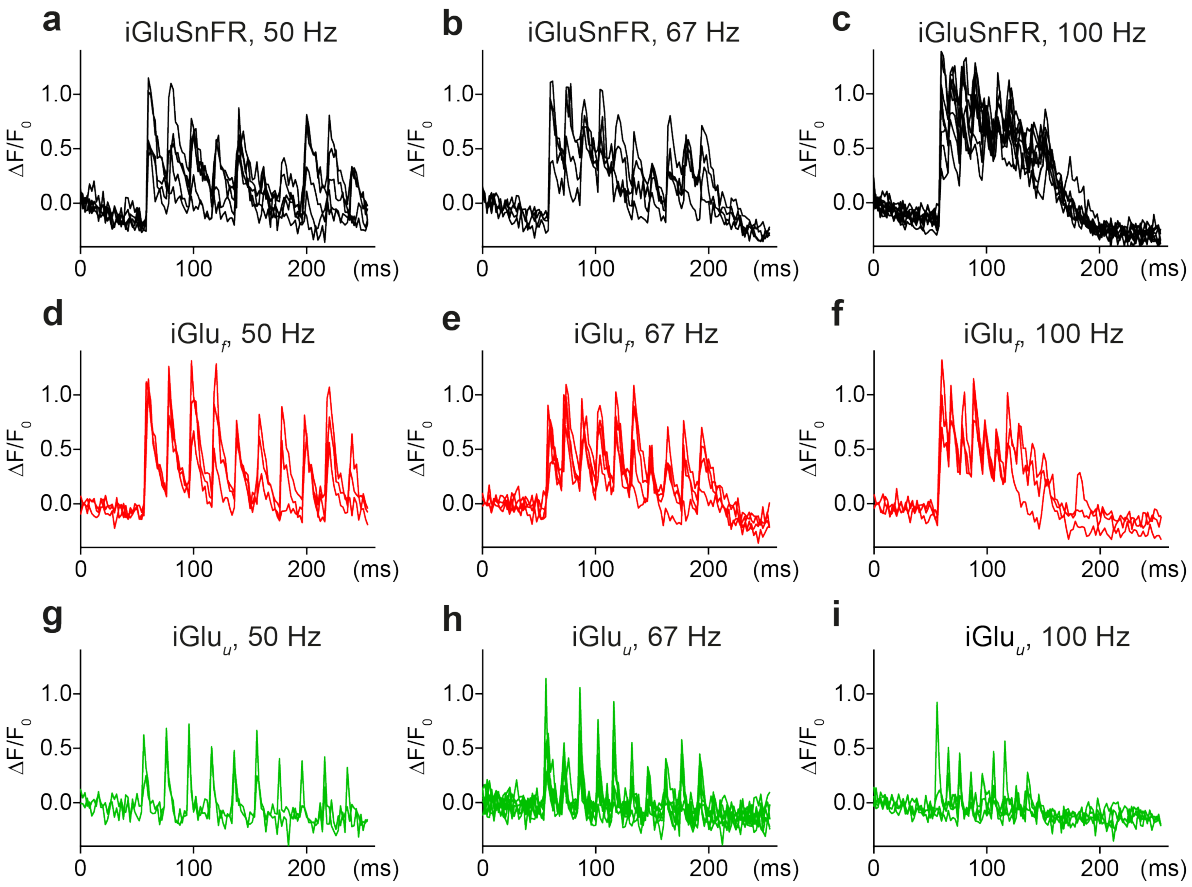

Figure 24: Fluorescence time course in single boutons of iGluSnFR and variants

Fluorescence time course ($\Delta F/F_0$) in single boutons expressing **(a-c)** iGluSnFR, **(d-f)** iGlu$_f$ and **(g-i)** iGlu$_u$ stimulated by 10 action potentials fired at **(a, d, g)** 50 Hz, **(b, e, h)** 67 Hz and **(c, f, i)** 100 Hz. Number of trials: **(a)**, 5; **(b)**, 4; **(c)**, 8; **(d)**, 3; **(e)**, 4; **(f)**, 3; **(g)**, 2; **(h)**, 7; **(i)**, 4.

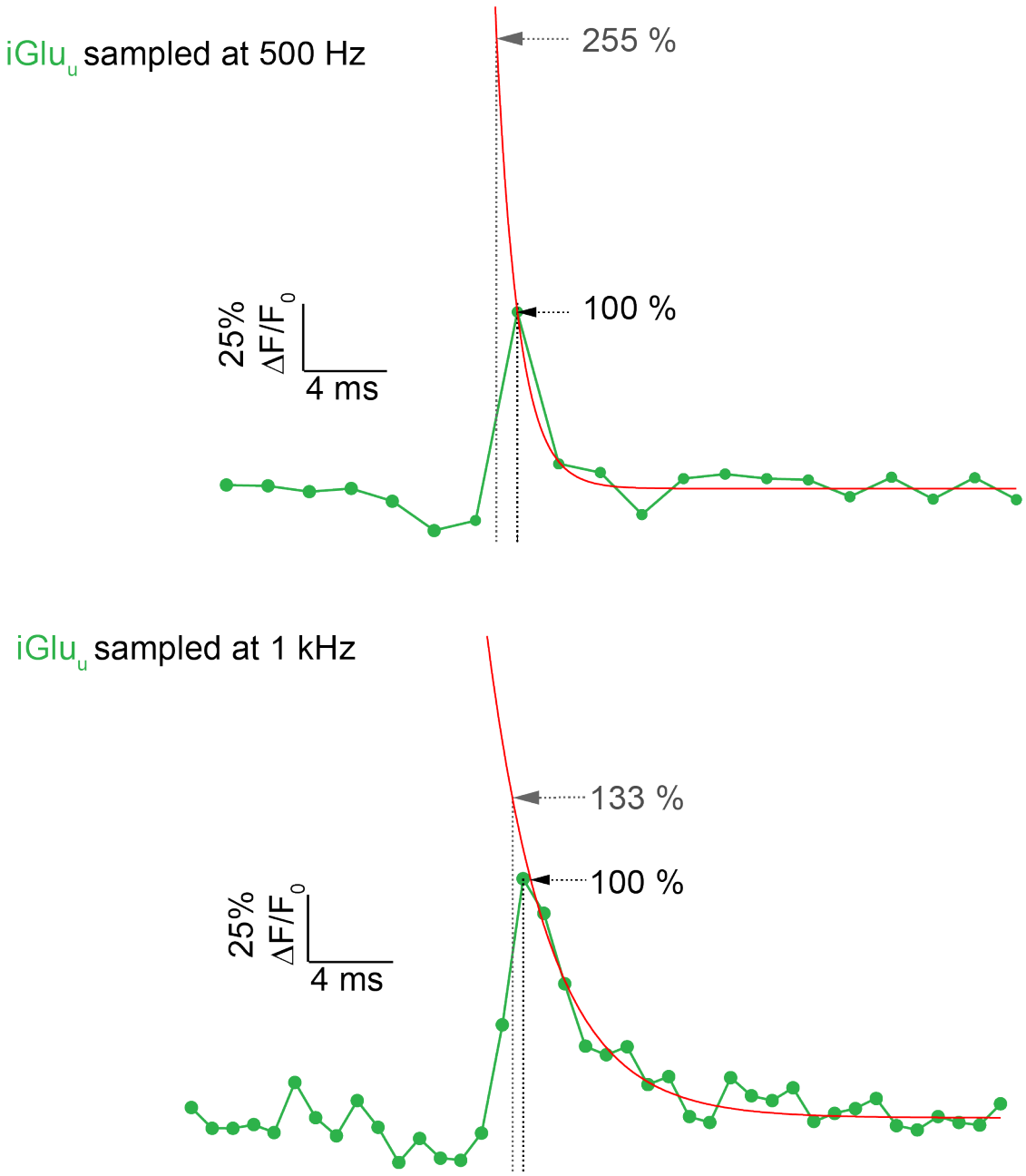

Figure 25: Estimating peak amplitudes at different sampling frequencies

When sampling iGlu$_u$ fluorescence at 500 Hz, it is possible to miss the peak of the fluorescence transient. Sampling at 1 kHz reduces the potential error to ~33%.

Table 1: Brightness of iGluSnFR variants

Protein	Φ		$\varepsilon_{o(492nm)}$ ($M^{-1}cm^{-1}$)		Brightness ($mM^{-1}cm^{-1}$)	
	-Glu	+Glu	-Glu	+Glu	-Glu	+Glu
iGluSnFR	0.65 ± 0.02	0.66 ± 0.02	9294 ± 86	38801 ± 293	6.1 ± 0.2	25.4 ± 0.8
Glu_f	0.65 ± 0.02	0.68 ± 0.02	8789 ± 76	28644 ± 127	5.7 ± 0.2	19.4 ± 0.6
$iGlu_u$	0.67 ± 0.02	0.67 ± 0.02	7895 ± 105	22796 ± 120	5.3 ± 0.2	15.3 ± 0.5

Brightness values were obtained from quantum yield and ε_o measurements.

Table 2: Fluorescence and equilibrium glutamate binding properties of iGluSnFR variants

Protein	F_r[a] -Glu	F_r[a] +Glu	$F_{r(+Glu)}$ / $F_{r(-Glu)}$	K_d (μM)	*n*
iGluSnFR	1.0	5.4	5.4 ± 0.7	33.4 ± 0.2	2.3 ± 0.2
E26A	3.6	12.3	3.4 ± 0.6	18.6 ± 0.02	2.6 ± 0.1
E26R	4.7	7.3	1.6 ± 0.5	19.3 ± 0.8	2.3 ± 0.2
R25K	1.5	3.1	2.1 ± 0.1	(2.3 ± 0.1) x 10^3	1.5 ± 0.1
T93A	0.7	1.2	1.7 ± 0.5	(12 ± 4) x 10^3	1.3 ± 0.2

[a]Relative fluorescence values were determined using apo-iGluSnFR as reference (F_r = 1).

Table 3: Selectivity of iGluSnFR, iGlu$_f$ and iGlu$_u$ for L-aspartate and L-glutamine

Protein	$F_{(+Asp)}$ / $F_{(-Asp)}$	$K_{d(Asp)}$ (μM)	*n*	$F_{(+Gln)}$ / $F_{(-Gln)}$	$K_{d(Gln)}$ (μM)	*n*
iGluSnFR	4.7 ± 0.3	44.6 ± 0.3	1.6 ± 0.1	6.4 ± 0.8	1900 ± 100	1.3 ± 0.1
iGlu$_f$	2.7 ± 0.2	82.0 ± 0.6	1.2 ± 0.1	5.6 ± 0.5	3700 ± 100	1.3 ± 0.1
iGlu$_u$	1.6 ± 0.2	61.7 ± 0.4	1.7 ± 0.1	2.3 ± 0.3	10800 ± 300	1.1 ± 0.1

[a]Fluorescence dynamic range is reported as fold enhancement by aspartate or glutamine ligand binding.

Table 4: Kinetic properties of fast iGluSnFR variants iGlu$_f$ and iGlu$_u$

Protein	K_d (μM)	*n*	$k_{on(lim)}$ (s^{-1})	$t_{1/2(on)(lim)}$ (ms)	k_{off} (s^{-1})	$t_{1/2(off)}$ (ms)
iGluSnFR	33 ± 0.2	2.3 ± 0.2	643 ± 23	1.1 ± 0.04	110 ± 4	8.5 ± 0.4
E26D (iGlu$_f$)	137 ± 4	1.7 ± 0.1	1240 ± 77	0.6 ± 0.04	283 ± 36	2.4 ± 0.3
S73T (iGlu$_u$)	600 ± 16	1.8 ± 0.1	604 ± 12	1.1 ± 0.02	468 ± 58	1.5 ± 0.2

K_d and Hill coefficient (*n*) values were obtained from the equilibrium glutamate titrations at 20 °C. Fluorescence rise (limiting rate, $k_{on(lim)}$) and decay (k_{off}) rates were measured by glutamate association and dissociation stopped-flow kinetic experiments.

Table 5: **Fitted and modelled kinetic parameters of the fluorescence response of iGluSnFR variants**

Scheme 1	K_1 (M^{-1})	K_2	$K_{d(calculated)}$ (M)	k_{+1} ($M^{-1}s^{-1}$)	k_{-1} (s^{-1})	k_{+2} (s^{-1})	k_{-2} (s^{-1})	K_1k_{+2} ($M^{-1}s^{-1}$)	$K_{d(measured)}$ (M)	n
iGluSnFR	3642	5.2	4.4×10^{-5}	2.7×10^{7}	5965	569	110	2.1×10^{6}	3.3×10^{-5}	2.3
(20 °C)	3431	3.4	6.6×10^{-5}	2.8×10^{7}	8161	756	220	2.6×10^{6}	4.0×10^{-5}	1.7
(34 °C)										
$iGlu_f$	1568	2.35	1.47×10^{-4}	3.5×10^{6}	2206	944	283	1.5×10^{6}	1.37×10^{-4}	1.7
(20 °C)										
$iGlu_u$	1291	0.29	6.00×10^{-4}	2.2×10^{6}	1704	136	468	1.7×10^{5}	6.00×10^{-4}	1.8
(20 °C)										

Fitted parameters to the kinetic model illustrated in Figure 19 are shown for iGluSnFR and fast variants. Fitting the association kinetic records to Scheme 1 (Supplementary information, Kinetic theory) gives parameters for a hyperbole, K_1, $k_{+2} + k_{-2}$, k_{-2} and the initial gradient, the apparent association rate constant K_1k_{+2}. Values for k_{+1} and k_{-1} were obtained by global fitting using Dynafit. The measured and calculated overall K_d values were in good agreement.

4 Discussion

By measuring glutamate release into the cleft of Schaffer collateral synapses, we provide direct evidence for frequent MVR events at a single AZ under conditions of high p_r. This study confirms a series of previous studies suggesting MVR can occur at various synapses in the CNS (Tong and Jahr, 1994; Auger et al., 1998; Wadiche and Jahr, 2001; Oertner et al., 2002). We estimated the iGluSnFR response to the release of a single vesicle (q) with three different approaches of increasing complexity: analyzing the amplitude of successes under low p_r conditions, measuring the amplitude of desynchronized events during strontium perfusion, and fitting a binomial model to the complete distribution of successes and failures from a single bouton. The resulting estimates of q were very consistent between methods and between individual experiments, indicating that the presynaptic *quantum* is indeed of constant size at glutamatergic synapses (although postsynaptic responses may vary). We can reject the univesicular release hypothesis for the majority of Schaffer collateral synapses, as they are capable of increased glutamate output under high p_r conditions and produce amplitude distributions consistent with binomial statistics.

4.1 Presynaptic dynamic range

My results show that even the smallest synapses in the brain are capable of MVR. The strong correlation I and others (Leitz and Kavalali, 2011) observe between potency and p_r indicates that p_r is the mechanism that regulates whether multiple vesicles are released simultaneously or not. Thus, if docked vesicles undergo exocytosis independently of each other, the more docked vesicles (and the higher p_{ves}*),* the higher the likelihood of observing MVR events. I found very few synapses that were not capable of releasing multiple vesicles

even in a condition of very high p_r. Those synapses have the feature of 'elementary synapses' (Pulido et al., 2014) as suggested by the one-site-one-vesicle paradigm. Nevertheless, the fact that those synapses release only a single vesicle is more likely to be a consequence of the synapse having only a single docked vesicle rather than a molecular machinery mediating lateral inhibition for limiting the number of released vesicles to one, as was suggested previously (Stevens, 2003). Thus, even if those elementary synapses exist, they represent a minority and not a rule for synaptic transmission at CNS synapses. However, under low calcium conditions, p_{ves} is low (0.02 - 0.09), and MVR events are quite rare. Given that physiological $[Ca^{2+}]_e$ in awake animals is about 1.0 -1.3 mM (Ding et al., 2016) this raises the question why synapses use only such a small fraction of their dynamic range. Whether these synapses operate in a high or low p_r regime when the animal is engaged in a behavioral task and neuromodulatory inputs are active remains to be seen.

4.1.1 Variability in p_r and PPR among boutons

PPR is a measure that is often used to assess whether a change in p_r mediates a change in synaptic strength. However, in my experiments, I show that a ~ 10-fold change in p_r, resulting in strongly potentiated EPSPs, can be induced without significant change in PPR (Figure 13d). What could be the reason for such a small paired-pulse depression in 4 mM Ca^{2+}? According to the well-known steep anticorrelation between initial p_r and PPF (Debanne et al., 1996), I expected a strong depression under high $[Ca^{2+}]_e$ leading to very high p_r. However, I barely observed any depression. A reason could be that substantial Ca^{2+} influx not only leads to high p_r, but also accelerates the recovery from depression by inducing mobilization of vesicles to the AZ. In addition, as I used a relatively long interval between the two APs (ISI 48 ms), there might have been enough time for replenishing the RRP between

the first and second stimulus (Wang and Kaczmarek, 1998). Thus, the importance of presynaptic changes for short-term plasticity might have been underestimated when assessed only with a pair of pulses.

The location of presynaptic terminals relative to each other and relative to the postsynaptic cell also seems to play a role in p_r variability. I observed that two neighboring boutons have more similar p_r than expected by chance (Figure 7c and d). This is in accordance with data from primary hippocampal cultures where the CV of the p_r is lower for boutons belonging to the same axon than boutons from different axons and cells (Ariel et al., 2013). Another study, combining fluorescence imaging in dissociated hippocampal cultures, FM-dye labeling, electrophysiological recordings and subsequent EM analysis, showed that presynaptic terminals from a common axon connecting the same dendritic branch shows strongly correlated p_r (Branco et al., 2008). However, with our approach, we cannot assess whether two neighbor boutons contact the same cell or even the same dendritic branch.

4.1.2 Ca^{2+} dependent release

It is known that the increase in vesicular p_{ves} evolves with the third to the fifth power of the Ca^{2+} influx (Schneggenburger and Neher, 2000). Therefore, I would have expected to measure a ~4^4 fold increase in p_{ves} from the quantal analysis when monitoring glutamate transients from 1 mM to 4 mM $[Ca^{2+}]_e$. However, my analysis showed only a ~ 10-fold increase in p_{ves}, on average. There are several parameters to consider here. First, to avoid changes in membrane excitability, I adjusted $[Mg^{2+}]$ according to $[Ca^{2+}]$ in order to keep the concentration of divalent ions constant ($[Ca^{2+}] + [Mg^{2+}] = 4$ mM) from low (1 mM) to high (4 mM) $[Ca^{2+}]$. How Mg^{2+} affects the p_{ves} is poorly understood. For this reason, I cannot exclude any contribution of external Mg^{2+} to p_{ves}. Second, a study monitoring the presynaptic Ca^{2+} influx in response to a single AP under gradually increased $[Ca^{2+}]_e$ ranging from 2 to 10 mM

Ca^{2+} observed that Ca^{2+} influx saturates along with the saturation of exocytosis monitored with vGlut1-pHluorin (Ariel, 2010). This suggests that the saturation of exocytosis is a consequence of the saturation of Ca^{2+} capable of fluxing into the terminal regardless of the amount of external Ca^{2+}. Third, in some boutons I recorded from, I might have reached the maximum number of vesicles that can be released upon a single AP, leading to a ceiling effect (p_{ves} = 1).

4.1.3 Comparing AMPAR-mediated currents to iGluSnFR signals

An unknown factor to take into account while measuring iGluSnFR signal is that I am unsure whether the glutamate transients are occurring at synapses onto other excitatory (i.e. pyramidal) or inhibitory neurons. This was not the case during paired-recordings of CA3-CA1 cells since I ensured that the postsynaptic cell was a CA1 pyramidal neuron by measuring intrinsic electrical properties. Could my results depend on the identity of the postsynaptic cell? Recent work has shown that excitatory synapses on the same axon may have different properties, depending on their target cell (Collman et al., 2015). In *stratum radiatum* of CA1, most CA3 boutons contact spines of excitatory CA1 pyramidal neurons, while only a small percentage (~2%) excites local interneurons (Gulyas et al., 1993). With my approach, I cannot distinguish between boutons innervating pyramidal CA1 cells or local interneurons. Therefore, I cannot rule out the possibility that a small fraction of synapses I imaged was innervating interneurons.

4.2 Function of MVR for synaptic transmission

How and to which extent does MVR shape synaptic transmission? When multiple vesicles are released simultaneously, they interact with a shared pool of postsynaptic receptors and the simultaneous release of multiple vesicles can have different effects for a synapse. First, MVR can increase the dynamic range of the presynaptic output allowing for analog modulation of synaptic transmission by altering the number of vesicles being released. Of course, this only holds true if postsynaptic receptors occupancy is low upon release of a single SV to be able to match the dynamic range of the cleft glutamate. My comparison of iGluSnFR imaging and AMPA receptor currents (Figure 13) as well as the diffusion simulation (Figure 12e) suggest that this is the case.

MVR affects synaptic transmission during high-frequency activity. Indeed, if a synapse only has a single docked vesicle (therefore MVR cannot occur), it would be expected to become strongly depressed during a burst of APs. If there are several docked vesicles - and therefore a higher likelihood for MVR to occur – the synapses are capable of transmitting more reliably in response to a single AP and with higher fidelity during a train of APs (Pulido et al., 2014). Under this assumption, MVR serves to counteract the unreliability of the stochastic nature of SV exocytosis. On the other hand, MVR leads to a faster consumption of presynaptic resources. Is MVR compatible with reliable transmission at high frequencies? In 4 mM Ca^{2+}, where the synaptic output is 10 times larger, I only observed weak paired-pulse depression of cleft glutamate (PPF = 0.8, Figure 13c and d). Thus, at least for a pair of pulses, synapses can avoid depression even under high release probability conditions. During long high-frequency trains, all boutons reduce their output in a similar fashion, regardless of their initial short-term plasticity (Figure 18). What mediates the short-term plasticity properties of a synapse? Is it the initial p_{ves} or is it the size, i.e., the number of docked vesicles? My data support the second hypothesis. It seems that the size of individual

boutons, measured as the intensity of the red morphological marker, are a better predictor than p_r of the behavior of that synapses when given a paired-pulse (Figure 26). Taken together, synapses having many docked vesicles are more likely to sustain transmission during high-frequency activity.

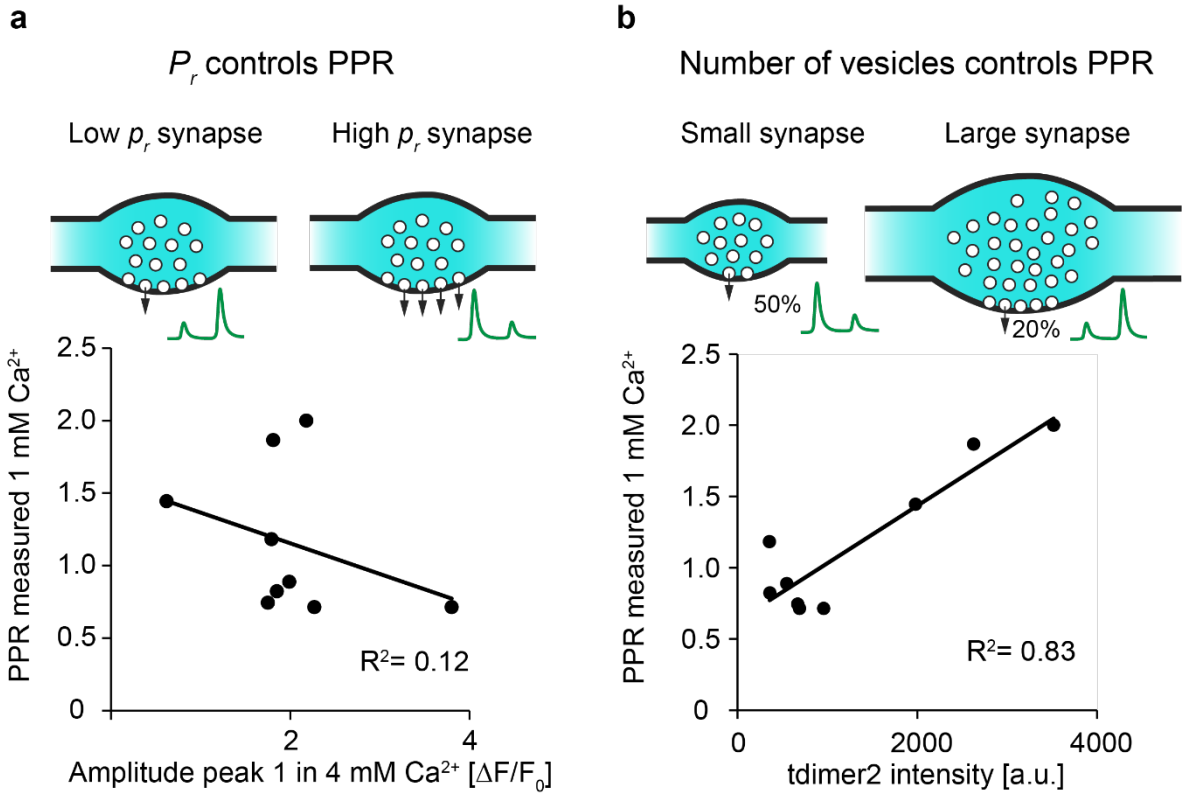

Figure 26: The number of docked vesicles sets the short-term plasticity properties at individual synapses.

a) Correlation between the PPR measured with iGluSnFR from the average synaptic strength in 1 mM Ca^{2+} and the synaptic strength of the first peak of the same bouton measured in 4 mM Ca^{2+} as an indicator of the frequency of occurrence of MVR. The two parameters show only a very weak correlation. **b)** Correlation between the PPR measured with iGluSnFR from the average synaptic strength in 1 mM Ca^{2+} and the intensity of the red morphological marker tdimer2 as an indicator of synapse size shows a strong correlation. Thus, the bouton size (i.e., number of docked vesicles) is a reliable indicator of PPF.

4.2.1 Spillover

MVR increases the amount of released glutamate in the cleft, increasing the risk of spill-out or spillover of glutamate. It has been shown that the release of glutamate leads to activation of NMDARs located on the dendritic shaft and high-affinity mGluRs located on the presynapse (peri- or extrasynaptic) (Kullmann et al., 1996). Spillover can also activate neighbor synapses (Kullmann et al., 1996). Thus, with MVR events, synaptic transmission would not be restricted to one-to-one transmission but include inter-synaptic crosstalk by acting on neighboring NMDARs. NMDARs have a higher affinity than AMPARs and are therefore more prone to be activated by glutamate upon spillover. Whether glutamate reaches neighbor synapses depends on the inter-synapse distance, the geometry, diffusion speed of glutamate and the uptake rate of glutamate. Thus, MVR alone does not necessarily lead to inter-synaptic crosstalk even though the more vesicles being released, the higher the likelihood of observing spillover. From postsynaptic recordings only, it can be challenging to assess whether the increased amount of glutamate in the cleft is solely a consequence of MVR or also spillover. The interpretation of the origin of glutamate is notably a problem in studies using simultaneous stimulation of near-adjacent fibers where activation of many presynaptic terminals further increases spillover. In my study, I combined sparse expression with extremely sparse stimulation (single neuron) to exclude the possibility of spillover contaminating my optical measurements.

4.3 Classical quantal analysis

Studies based on purely electrophysiological recordings encounter interpretation issues regarding whether CNS synapses are capable of releasing multiple vesicles upon AP propagation. In a typical multi-peaked histogram from a postsynaptic electrical recording,

different sources could account for the variability. Signals could come from different synapses, and the variability in amplitude could be a consequence of the integration of multiple synapses. While recording at the soma, there is no information on the location and number of synapses. Hence, due to dendritic filtering, EPSCs from two different synapses give rise to different EPSC amplitude each (i.e., the further away from the soma the smaller the amplitude) in response to an equal number of SVs released, further smearing out the multiple peaks of the histogram. Therefore, at CA3-CA1 connections, distinct quantal peaks of EPSC distribution are not clear. An approach used to quantify the variability arising from a single synapse was to apply a hypertonic solution leading to spontaneous release to a small region of the dendrite (Bekkers et al., 1990; Raastad et al., 1992). This methodology allowed measuring mEPSCs stemming from a small region of the dendrite, in order to minimize the variability from dendritic filtering. Using whole-cell patch clamp recordings, Bekkers and colleagues adopted this strategy to monitor mEPSCs in cultured hippocampal neurons and hippocampal slices. They found that CA3-CA1 connections typically have a large trial-to-trial variability in quantal size and that this variability is not only a feature of cultured neurons. In summary, they proposed continuous synaptic amplitude, which is at odds with many studies. This study was heavily criticized (Larkman et al., 1992); pointing to quantal ('peaky') histogram counts: the diffusion of the hypertonic solution up to 15 µm lead to the activation of several synapses thus, contributing to the quantal size variability and, in addition, the frequency of the hypertonic solution evoked EPSCs should be much higher than the frequency of the mEPSCs to ensure variability measurement at a single synapse. Deconvolution of 'peaky' histograms has been attempted multiple times at CA3-CA1 connections to characterize the quantal parameters of individual synapses (Sayer and Redman, 1989; Sayer, Rod J and Redman, 1990; Larkman et al., 1992; Kullmann and Nicoll, 1992; Foster and McNaughton, 1991; Malinow, 1991; Larkman et al., 1997; Stricker et al., 1996; Stratford et al., 1997; Christian Stricker, 2003; Dityatev et al., 2003; O'Connor et al.

2007). Those studies used different statistical models of release and analytical methods for simplifying the deconvolution of the histogram counts (such as denoising of data, spectral analysis); a detailed description of these analyses is beyond the scope of this discussion. However, regardless of the level of accuracy and complexity, all data were generated from 'minimal stimulation', leading to the selection of specific synaptic connections that fulfilled the criteria for minimal stimulation. At least in some studies, this lead to a circular argument (non-uniform response amplitudes were an exclusion criterion). Furthermore, the number of axons stimulated and whether the same number of axons was stimulated at each trial was unknown. Some studies attempted paired recordings in acute slices, where the chance to find a connected pair is very low, thus requiring a large number of trials needed for quantal analysis and making the experiment very challenging and rather inefficient (ex: 2 pairs out of 150 (Stricker et al., 1996)). In all those scenarios, the number of connections is unknown allowing the authors to speculate on the number of connections recorded from, depending on the number of 'peaks' detected in the histogram. Besides, due to different electrotonic distances, *q* and its variability cannot be measured directly (unlike frog NMJ experiments). In classical quantal analysis applied to CNS synapses, *q* and its standard deviation are determined from their probability of failures and variability in fluctuation. However, this type of measurement relies heavily on a model like Poisson or a binomial model. By measuring direct glutamate release from the presynaptic terminals, I overcame all the major problems encountered in quantal analysis at CNS synapses discussed above and in section 1.7. In my study, the location of the synapse could not affect my measurement, and by desynchronizing the release by gradually replacing the $[Ca^{2+}]_e$ by $[Sr^{2+}]_e$, I could optically monitor *q* and its variability. It is important to note that the measured amplitude of *q* depends not only on the indicator but also on the spatial and temporal resolution of the detection system as it is trying to catch the peak fluorescence caused by a rapidly diffusing cloud of glutamate. However, for optical quantal analysis, the interpretation between the signal and noise is slightly different

due to inherent properties of photon noise. Indeed, photon noise is not independent of the signal, as it follows a Poisson statistics. Shot noise increases with the square root of the photon count, therefore, for a larger number of quanta release (larger $\Delta F/F_0$ in our case) the variability of the signal increases as well. Experimentally, my approach is rather straightforward and only a few trials (~ 60 trials per $[Ca^{2+}]_e$) were sufficient to determine quantal parameters. A low number of trials not only simplifies the experiment in practical terms, but most importantly, it can allow detecting changes in quantal parameters over time. Furthermore, with my approach, I avoided synaptic input from other synapses, and changes in series resistance cannot account for artifacts in amplitude (a problem when doing electrophysiological measurements). The only selection criterion to assess the quality of my optical recordings was based on the baseline noise. The latter depends on the expression level of the glutamate sensor: if there are too few molecules of iGluSnFR, the change in fluorescence upon release of a single SV is too low to be resolved from the imaging noise. Nevertheless, smaller boutons tend to be dimmer and therefore I might have preferentially select larger boutons. The efficacy of presynaptic performance has been previously been linked to the size of the boutons (Branco et al., 2010; Welzel et al., 2011). Therefore, the larger boutons that we imaged also tend to have higher p_r.

Analysis of spine calcium signals provided p_r estimates at individual synapses yielding an average p_r of 0.37 in 1.5 mM Ca^{2+} (Oertner et al., 2002), which is consistent with the slightly higher value I saw with iGluSnFR in 2 mM Ca^{2+}.

4.3.1 Monitoring [glu] transients has distinct advantages over EPSCaTs measurements

What are the advantages of optical quantal analysis with a glutamate sensor as opposed to spine Ca^{2+} measurements? Even though optical quantal analysis using excitatory

postsynaptic spine Ca^{2+} transients (EPSCaTs) as a proxy for electrical postsynaptic responses allows for direct investigation of individual synapses (Yuste et al., 1999; Oertner et al., 2002; Emptage et al., 2003), direct measurement of glutamate from the presynaptic terminal has several advantages: First, the unitary response to the release of a single vesicle (quantal size q, here measured in units of $\Delta F/F_0$) is largely determined by the properties of iGluSnFR and thus, is very similar across individual synapses. EPSCaT amplitude, in contrast, depends on the density of NMDA receptors, AMPA receptors, and the diluting volume of the spine. The unitary EPSCaT is therefore different in every synapse, and it is practically impossible to wait for spontaneous EPSCaTs (the equivalent of "miniature end-plate potentials") while imaging continuously. Knowing q is at the heart of a true quantal analysis. Furthermore, the low number and stochastic behavior of postsynaptic NMDA receptors (Nimchinsky et al., 2004) add variability to EPSCaTs, making it difficult to conclude vesicular release statistics from the amplitude distribution. Second, EPSCaTs are mediated by voltage-dependent NMDA receptors and voltage-gated calcium channels. Dendritic depolarization by other active synapses can, therefore, influence EPSCaT amplitudes at the synapse under scrutiny in a non-linear fashion. iGluSnFR signals, in contrast, are highly localized and unlikely to be contaminated by the activity of nearby synapses. Third, EPSCaTs are sensitive to the extracellular divalent ion concentration (Ca^{2+}, Mg^{2+}, Sr^{2+}) as they affect both, the release machinery and the response of the optical calcium sensor while iGluSnFR is not affected. The calcium-independent read-out made it possible for us to directly investigate the impact of $[Ca^{2+}]_e$ on the release machinery and to replace $[Ca^{2+}]_e$ by $[Sr^{2+}]_e$, generating desynchronized fusion events. Fourth, iGluSnFR probes presynaptic function directly. The identity of the presynaptic neuron is known and therefore the most challenging part of EPSCaT imaging, finding a responding spine, is no longer necessary. Several boutons on the same axon can be probed in parallel or sequentially, removing the bias towards strongly responding synapses that troubles EPSCaT analysis. Fifth, even if the

synapse of interest does release multiple vesicles simultaneously, if AMPARs are close to saturation, the release of multiple vesicles will not give rise to equal increments of EPSCaTs amplitude as the saturation kinetic is hyperbolic. Last, the throughput of this approach is low as only a single synapse at a time can be studied and it is not possible to assess changes at other synapses formed by the same axon.

4.3.2 Binomial model

The quantal parameters were extracted by fitting a probabilistic model of transmitter release to the data. The binomial model of transmitter release first applied at central synapses in 1964 in the spinal motor neurons of the cat (City, 1964). How well the binomial model applies to system of interest influences the reliability of the measured parameters. Whether the binomial model is the best model for describing release at CNS synapses has been under debate, but it presents the advantage of keeping the number of variables as low as possible. The assumptions underlying the binomial model include: (1) docked vesicles undergo exocytosis independently of each other (2) release is synchronous, (3) uniform p_{ves} at all release sites. Let us take the example of two docked vesicles: if each vesicle had a p_{ves} of 0.4, then the probability that the two vesicles are released simultaneously is 0.4*0.4 = 0.16. The binomial model seems to be a very reasonable model of release statistic at CA3-CA1 synapses as I observed a steep non-linear relationship between p_r and the amplitude of successes. This relationship is confirmed in a previous study monitoring the release of vesicles with a VGlut1-pHluorin at individual synaptic terminals under different external Ca^{2+} concentration in dissociated cultures (Leitz and Kavalali, 2011). Consequently, the higher the p_r, the higher the likelihood that several docked vesicles undergo exocytosis. When fitting of response histograms with multiple Gaussians, we constrained the relative amplitude of

the individual Gaussians by the binomial distribution. The underlying assumption such as identical p_{ves} seemed reasonable as I monitored the release from a single synapse and not from multiple connections. We noted, however, that in several cases alternative combinations of n, p_{ves}, and q provided almost equally good fits. To further constrain the model, I used data from boutons that were recorded in different Ca^{2+} concentrations. In essence, the low p_r condition allowed estimating q while the high p_r condition gave a precise measure of n. Saturation of iGluSnFR during multivesicular events was taken into account.

4.3.3 Inter and intrasynapse variability in [glu] transients

Why do some histograms appear 'peakier' than others? Is the trial-to-trial variability real biological variability due to SVs size or partial release? Do imaging noise or tissue drift contribute to those observed phenomena? The release sites were very local and very sensitive to mechanical drift. In this respect, the rather large PSF of a 2PLSM along the optical axis (z-direction) encompasses of the full signal and the system is, therefore, less drift sensitive. Small drifts along the optical axis change the SNR of the signal but not the peak amplitude ($\Delta F/F_0$). By scanning over the whole bouton with a spiral scan, I ensured hitting at least once the release site and compensate for any XY drift. In addition, I refocused frequently between individual trials. For this reason, I can exclude drift as the main contributor to trial-to-trial variability. iGluSnFR is a membrane-bound molecule. Its slow diffusion compared to a cytoplasmic protein does not allow a fast renewal of bleached iGluSnFR molecules. I therefore limited the number of imaging trials to ~100 per boutons to avoid gradual run-down of responses due to laser damage. Minimizing or excluding artifacts was important to ensure that trial-to-trial variability within an experiment truly reflected glutamate concentrations in the synaptic cleft. Quantal size (q) was remarkably constant between

boutons. I expected some variability as a consequence of the cleft orientation relative to the focal plane. I estimated 20% inter-bouton variability due to this factor, which is close to the measured value (CV of q = 21%). In rat hippocampal neurons the average diameter of SVs was found to have a mean outer-diameter range of 35–45 nm which corresponds to an average volume of vesicle lumen (considered as a physiologically more relevant measure) of 11'500 nm^3 (Schikorski and Stevens, 1997; Harata et al., 2001; Harris and Sultan, 1995). It was discovered that the mean SV volume varies up to five-fold (5000 nm^3 to 25000 nm^3) among neighboring excitatory rat hippocampal neurons both *in vitro and in vivo* (Qu et al., 2009; Hu et al., 2008). This size difference corresponds to a 5-fold difference in the volume between the smallest and the largest vesicles, suggesting a significant difference for neurotransmitter storage capacity between these vesicles (Hu et al., 2008). The consistent value for q I report here is therefore surprising. Variable fixation artifacts could have introduced additional variability in the EM diameter measurements. Alternatively, it is possible that only vesicles with a specific diameter or filling state are allowed to dock and fuse, which would be a novel quality control mechanism ensuring quantal uniformity. In any case, my functional measurements from life synapses suggest that glutamate quanta are more uniform than previous estimates from fixed tissue.

4.4 MVR controversy

How can I reconcile my data showing a steep non-linear correlation between p_r and cleft glutamate (Figure 8c and d) with a previous study measuring PSCs at the soma in response to focal stimulation and has evidence for equal quantal size under different p_r conditions (Dobrunz and Stevens, 1997)? A possible reason underlying this discrepancy could be the selection of the recorded synapses. Electrophysiological studies using focal stimulation apply

strict criteria whether the PSC is resulting from a single connection or not, thereby selecting small synapses that behave as suggested by the all-or-none hypothesis. Indeed, what the experimenter interprets as stimulation of several axons (large, reliable and variable EPSCs) could simply have been a 'strong' single synapse releases multiple vesicles upon propagation of an AP. If so, only the small and weak synapses – that indeed seem to release mainly a single vesicle in physiological conditions - will be used in the experiment. Whereas in my experiment, I rather selected large boutons, thereby having a higher proportion of synapses in which MVR prevails. Another explanation is that saturation of AMPA receptors in purely electrophysiological studies precludes the detection of MVR events. Indeed, under high receptor occupancy, the resulting closely spaced PSC amplitudes tend to appear as a single Gaussian peak in the PSC amplitude fluctuation count. However, I show that AMPARs do report the dynamic range of presynaptic release. Thus, the occupancy of AMPARs is relatively low upon release of a single vesicle to be able to match the ~10-fold increase of cleft glutamate from 1 mM to 4 mM $[Ca^{2+}]_{e.}$ Also, other studies have reported that receptor occupancy is not very high in physiological conditions (McAllister and Stevens, 2000). Under steady-state conditions, the concentration of glutamate from a single vesicle would be sufficient to saturate postsynaptic receptors. Glutamate concentration was estimated to reach 1.1 mM in cultured hippocampal synapses (Frerking and Wilson, 1996). However, as for the iGluSnFR molecules, the low on-rate limits the number of glutamate molecules that can be captured by AMPARs, preventing saturation upon release of a single vesicle.

4.4.1 Interpretation of glutamate transients amplitude variability under UVR assumption or partial fusion

The increase in synaptic glutamate associated with increased p_r observed in previous studies (Tong and Jahr, 1994), could be alternatively explained by diffusion of glutamate from adjacent sites (Barbour and Häusser, 1997). Could the larger glutamate concentrations observed with iGluSnFR under high p_r conditions indeed come from synaptic spillover? This seems rather unlikely. First, in contrast to extracellular field stimulations, where bundles of axons are stimulated, I triggered APs and thus release in only one pyramidal cell, and presynaptic boutons are spatially well separated. Second, I observed the same local confinement of glutamate release under low and high p_r conditions (Figure 9 and Appendix 7.2), indicating that the source of glutamate is only coming from the AZ of the bouton under investigation. Third, glutamate diffusion is locally restricted in tissue due to rapid clearance via glutamate uptake by the bouton and astrocytes at the periphery of synapses. Indeed, blocking glutamate uptake by TBOA did not affect the amplitude of synaptic iGluSnFR transients (Figure 23).

Does partial fusion of SVs account for the observed trial-to-trial variability? Interestingly, in some histograms, the distribution of the failure trials around zero was not perfectly symmetric but was slightly skewed towards positive values. This bias was not due to errors in the fitting routine since the fits from all ‘no pulse lines’ had a Gaussian distribution around 0. Instead, this population may represent incomplete fusion events (KR) of single SVs resulting in the release of only a fraction of the vesicular glutamate molecules (Zhang et al., 2009). The fact that multiple vesicles can be released simultaneously does not exclude that those individual vesicles could only release part of their content. Under this assumption, the variability of glutamate peak concentration arising from partial fusion would need to be taken into account. Using a pH-sensitive quantum dot of the size of the intravesicular volume, a

study showed that only 20% of all fusion events of vesicles undergo partial fusion. Upon partial fusion, the quantum dot recovers the fluorescence when SVs get refilled with H^+, but no recovery of fluorescence is observed under full fusion as the quantum dot gets released (Zhang et al., 2009). The CV of synaptic vesicle diameter in rat brain has been estimated to be 17% (Nava et al., 2014) which would lead to a CV of 60% variability in *q*. In addition, a recent study manipulating the filling state of SV optogenetically, demonstrates that synaptic vesicles are not filled with glutamate to their maximal capacity which allows a specified dynamic range in the quantal size (Rost et al., 2015). Partial fusion is therefore likely to be negligible to the trial-to-trial variability in peak amplitude than SV size.

Could the variability in glutamate peak concentration only be explained through the partial fusion of a single vesicle as an alternative to the binomial model of release? This is a very unlikely scenario as from 1 mM $[Ca^{2+}]_e$ to 4 mM $[Ca^{2+}]_e$ I observed an ~11-fold change in cleft glutamate which exceeds the change in fluorescence a single vesicle (3000 molecules of glutamate) could produce regarding $\Delta F/F_0$ fold change (Figure 12e). In addition, it would be very surprising if a partial fusion mechanism produced unitary events of consistent amplitude (*q*) at different boutons. However, as the 'kiss-and-run' scenario is completely unconstrained, it could even mimic binomial statistics! In my opinion, a scenario that cannot be tested experimentally (falsified) is not very useful as a working hypothesis.

4.5 Number of release sites

Different studies using different methods to determine the number of exocytotic sites within an AZ provided different estimates of RRP size. EM studies were the first providing an insight into the number of potential release sites and estimated the number of docked vesicles to range from 2 to 27 (mean of 10.3) (Schikorski and Stevens, 1997). A study using

more advanced tissue fixation methods and tissue electron tomography quantified the number of vesicles docked to the plasma membrane at glutamatergic synapses from organotypic hippocampal slices cultures and estimated 10 to 12 docked vesicles per active zone (Imig et al., 2014). Functional measurements based on the statistic of synaptic transmission to quantify the number of release sites have provided lower estimates of release sites (Siksou et al., 2009; Oertner et al., 2002). In my study, I estimated on average ~6 readily releasable SVs. Several issues can lead to a discrepancy between the morphological and functional determination of the number of RRP. First, docking of SVs has been shown to be a dynamic and reversible process, (Siksou et al., 2009) therefore, counting the number of docked vesicles in a snapshot might overestimate the number of release sites at a single AZ. Second, electrophysiological or optical studies based on statistics of synaptic transmission to determine the number of release sites, are indirect and thus, might be biased towards release sites with a higher p_r. A recent study using fluorescent microscopy localized individual vesicle fusion events in synapses of primary hippocampal cultures and determined the number of distinct release sites per AZ through a clustering method (Maschi and Klyachko, 2017). They estimated 10 release sites (if a release site has a diameter of 70 nm) per AZ. Whereas a study using cultured hippocampal neurons, combining total internal reflection fluorescence microscopy (TIRF) and a pHluorin to monitor vesicle release, estimated 3 to 8 release site per active zone (Funahashi et al., 2018). Another recent study has evidence for a molecular morphological correlate of functional measurements of the number of release sites (Tang et al., 2016). In this study, Tang and colleagues mapped the vesicle fusion position by detecting vesicle fusion event with a VGlut1-pHluorin type of probe within single synapses in primary hippocampal cultures. They combined those measurements with a super-resolution technique (3D-STORM) to observe that those fusion sites correlated with RIM and Munc13 forming nanoclusters (~80 nm) within the AZ. Furthermore, using super-resolution microscopy, they showed that the location of the fusion

sites is in direct apposition to the receptor clusters in the postsynaptic density. They suggest the existence of a trans-synaptic molecular nanocolumn to align presynaptic release sites with postsynaptic clusters. The existence of Munc13 nanoclusters was later confirmed by another study also combining super-resolution microscopy and imaging of the neurotransmitter glutamate to map release sites at individual synapses and estimated ~6 release sites per AZ (Sakamoto et al., 2018).

4.6 Localization of the sensor

Could the subcellular localization of the indicator affect my measurements? Most likely not, as I assume a homogeneous expression and a free diffusion in the membrane of iGluSnFR as it does not contain any targeting sequence. However, I cannot resolve the distribution of the sensor by two-photon microscopy as the resting fluorescence of iGluSnFR is very dim. In fact, inhomogeneous distribution of the indicator as well as expression level differences would probably have little effect on our synaptic measurements as we evaluate relative changes in fluorescence ($\Delta F/F_0$). Endosomes (60-100 nm) and large dense core vesicles (80-120 nm) are also found in the presynaptic terminals (Aravanis et al., 2003; Harris and Weinberg, 2012) and I cannot exclude that some iGluSnFR molecules are present in those structures. Indeed, I sporadically observed travelling bright structures revealing the presence of non-quenched iGluSnFR molecules, which could be trapped in endosomes where the pH is not acidic enough for quenching GFP. Future versions of SuperGluSnFR may be genetically targeted to the active zone by fusion to specific synaptic proteins or targeting motifs, raising the possibility of direct comparison of synaptic vs. extrasynaptic glutamate dynamics notably during high frequency activity where glutamate might diffuse out of the cleft.

4.6.1 Non-linearity of the sensor

iGluSnFR signals were corrected for non-linearity prior to quantal analysis whereas for $iGlu_u$ signals, peak amplitudes were directly extracted. My synaptic measurements were typically below 100% $\Delta F/F_0$, suggesting that less than half of $iGlu_u$ molecules inside the PSF of the microscope were bound to glutamate at the peak of the signal. Katalin Török and colleagues measured the dynamic range of $iGlu_u$ to be 15.3 - 5.3 / 5.3 = 189 % $\Delta F/F_0$, which would point to a cleft glutamate concentration of ~0.6 mM (K_d of $iGlu_u$). However, this is a rough estimate, as 3D diffusion modeling would be necessary to extract absolute glutamate concentrations from the $iGlu_u$ signals. I indeed strongly rely on the non-linearity correction to extract the quantal parameters. A sensor with a lower affinity might allow me to perform my measurements in the linear range. Due to saturation of the sensor, I cannot resolve the simultaneous release of more than 3-4 vesicles. Therefore, a sensor displaying a higher dynamic range would be useful. Combined expression of iGluSnFR together with a red-shifted pHluorin could be used to resolve the number of vesicles released. pHluorin has the ability to detect the release of a single SV and would not saturate during MVR, but does not report the filling state (glutamate concentration) of individual vesicles.

5 Conclusion

Activity-dependent synaptic plasticity is thought to be the cellular basis for learning, memory, and behavioral flexibility, i.e., the ability of animals to adapt to changing environments. Assessing which parameters determine synaptic strength is essential for a mechanistic understanding of synaptic plasticity. With the method I developed in this study, it will be possible to identify precisely the presynaptic parameters that change after induction of long-term plasticity. For the study of synaptic physiology, iGluSnFR and its faster variants are a breakthrough. Questions that remained challenging to address at small CNS synapses with classical electrophysiological approaches can now be tackled:

1) Are small CNS synapses capable of releasing multiple vesicles upon a single action potential?
2) Is the variability of quantal amplitude a consequence of pre- or postsynaptic variability?
3) What is the degree of occupancy of postsynaptic receptors upon release of a single vesicle?

In my thesis work, I circumvented the two fundamental problems in classical quantal analysis at CNS synapses, namely no direct measurement of *q,* and recordings from an unknown number of release sites. My study, applying classical quantal analysis to hippocampal synapses, reveals that they contain no special mechanism that would prevent the release of several vesicles in response to a single presynaptic action potential.

6 References

Abenavoli A, Forti L, Bossi M, Bergamaschi A, Villa A, Malgaroli A (2002) Multimodal quantal release at individual hippocampal synapses: evidence for no lateral inhibition. J Neurosci 22:6336–6346.

Alabi AA, Tsien RW (2013) Perspectives on Kiss-and-Run: Role in Exocytosis, Endocytosis, and Neurotransmission. Annu Rev Physiol 75:393–422.

Andersen P, Morris R, Amaral D, Bliss T, O'Keefe J eds. (2006) The Hippocampus Book. Oxford University Press.

Ariel P (2010) Optical mapping of release properties in synapses. Front Neural Circuits 4:1–10.

Ariel P, Hoppa MB, Ryan TA (2013) Intrinsic variability in Pv, RRP size, Ca2+ channel repertoire, and presynaptic potentiation in individual synaptic boutons. Front Synaptic Neurosci 5:1–18.

Atluri PP (2006) The Kinetics of Synaptic Vesicle Reacidification at Hippocampal Nerve Terminals. J Neurosci 26:2313–2320.

Auger C, Kondo S, Marty a (1998) Multivesicular release at single functional synaptic sites in cerebellar stellate and basket cells. J Neurosci 18:4532–4547.

Auger C, Marty A (2000) Quantal currents at single-site central synapses. J Physiol 526 Pt 1:3–11.

Awatramani GB, Price GD, Trussell LO (2005) Modulation of transmitter release by presynaptic resting potential and background calcium levels. Neuron 48:109–121.

Balaji J, Ryan T a (2007) Single-vesicle imaging reveals that synaptic vesicle exocytosis and endocytosis are coupled by a single stochastic mode. Proc Natl Acad Sci U S A 104:20576–20581.

Barbour B, Häusser M (1997) Intersynaptic diffusion of neurotransmitter. Trends Neurosci 20:377–384.

Bartol TM, Keller DX, Kinney JP, Bajaj CL, Harris KM, Sejnowski TJ, Kennedy MB (2015) Computational reconstitution of spine calcium transients from individual proteins. Front Synaptic Neurosci 7:1–24.

Bekkers JM, Richerson GB, Stevens CF (1990) Origin of variability in quantal size in cultured hippocampal neurons and hippocampal slices. Proc Natl Acad Sci U S A 87:5359–5362.

Betz WJ, Bewick GS (1992) Optical analysis of synaptic vesicle recycling at the frog neuromuscular junction. Science 255:200–203.

Blumer C, Vivien C, Genoud C, Perez-Alvarez A, Wiegert JS, Vetter T, Oertner TG (2015) Automated analysis of spine dynamics on live CA1 pyramidal cells. Med Image Anal 19:87–97.

Bolshakov VY, Golan H, Kandel ER, Siegelbaum SA (1997) Recruitment of new sites of synaptic transmission during the cAMP- dependent late phase of LTP at CA3-CA1 synapses in the hippocampus. Neuron 19:635–651.

Borghuis BG, Looger LL, Tomita S, Demb JB (2014) Kainate Receptors Mediate Signaling in Both Transient and Sustained OFF Bipolar Cell Pathways in Mouse Retina. J Neurosci 34:6128–6139.

Boucher J, Kröger H, Sík A (2010) Realistic modelling of receptor activation in hippocampal excitatory synapses: Analysis of multivesicular release, release location, temperature and synaptic cross-talk. Brain Struct Funct 215:49–65.

Boyd IA, Martin AR (1956) The end-plate potential in mammalian muscle. J Physiol 132:74–91.

Branco T, Marra V, Staras K (2010) Examining size-strength relationships at hippocampal synapses using an ultrastructural measurement of synaptic release probability. J Struct Biol 172:203–210.

Branco T, Staras K, Darcy KJ, Goda Y (2008) Local Dendritic Activity Sets Release Probability at Hippocampal Synapses. Neuron 59:475–485.

Brun MA, Tan KT, Griss R, Kielkowska A, Reymond L, Johnsson K (2012) A semisynthetic fluorescent sensor protein for glutamate. J Am Chem Soc 134:7676–7678.

Brunert D, Tsuno Y, Rothermel M, Shipley MT, Wachowiak M (2016) Cell-Type-Specific Modulation of Sensory Responses in Olfactory Bulb Circuits by Serotonergic Projections from the Raphe Nuclei. J Neurosci 36:6820–6835.

Ceccarelli B, Hurlbut WP, Mauro A (1973) Turnover of transmitter and synaptic vesicles at the frog neuromuscular junction. J Cell Biol 57:499–524.

Christian Stricker SJR (2003) Quantal analysis based on density estimation. J Neurosci Methods 130:159–171.

Christie JM, Jahr CE (2006) Multivesicular release at Schaffer collateral-CA1 hippocampal synapses. J Neurosci 26:210–216.

City SL (1964) M-KCl internal filaments. :81–99.

Clayton EL, Cousin MA (2009) The molecular physiology of activity-dependent bulk endocytosis of synaptic vesicles. J Neurochem 111:901–914.

Collman F, Buchanan J, Phend KD, Micheva KD, Weinberg RJ, Smith SJ (2015) Mapping Synapses by Conjugate Light-Electron Array Tomography. J Neurosci 35:5792–5807.

Colquhoun BYD, Jonas P, Sakmann B (1992) Zellphysiologie, 6900. :261–287.

Costa RP, Mizusaki BEP, Sjöström PJ, van Rossum MCW (2017) Functional consequences of pre- and postsynaptic expression of synaptic plasticity. Philos Trans R Soc Lond B Biol Sci 372.

Daniels RW, Collins CA, Chen K, Gelfand M V., Featherstone DE, DiAntonio A (2006) A single vesicular glutamate transporter is sufficient to fill a synaptic vesicle. Neuron 49:11–16.

Darcy KJ, Staras K, Collinson LM, Goda Y (2006) Constitutive sharing of recycling synaptic vesicles between presynaptic boutons. Nat Neurosci 9:315–321.

de Juan-Sanz J, Holt GT, Schreiter ER, de Juan F, Kim DS, Ryan TA (2017) Axonal Endoplasmic Reticulum Ca2+ Content Controls Release Probability in CNS Nerve Terminals. Neuron:1–15.

De Robertis ED, Bennett HS (1955) Some features of the submicroscopic morphology of synapses in frog and earthworm. J Biophys Biochem Cytol 1:47–58.

De Simoni A, Griesinger CB, Edwards FA (2003) Development of Rat CA1 Neurones in Acute *Versus* Organotypic Slices: Role of Experience in Synaptic Morphology and Activity. J Physiol 550:135–147.

Debanne D, Guérineau NC, Gähwiler BH, Thompson SM (1996) Paired-pulse facilitation and depression at unitary synapses in rat hippocampus: Quantal fluctuation affects subsequent release. J Physiol 491:163–176.

Del Castillo J, Katz B (1954) Quantal components of the end-plate potential. J Physiol 124:560–573.

Denker A, Rizzoli SO (2010) Synaptic vesicle pools: An update. Front Synaptic Neurosci 2:1–12.

Devine MJ, Kittler JT (2018) Mitochondria at the neuronal presynapse in health and disease. Nat Rev Neurosci 19:63–80.

Ding F, O'Donnell J, Xu Q, Kang N, Goldman N, Nedergaard M (2016) Changes in the composition of brain interstitial ions control the sleep-wake cycle. Science 352:550–555.

Dityatev AE, Altinbaev RS, Astrelin A V, Voronin LL (2003) Combining principal component and spectral analyses with the method of moments in studies of quantal transmission. J Neurosci Methods 130:173–199.

Dobrunz LE, Stevens CF (1997) Heterogeneity of release probability, facilitation, and dpeletion at central synapses. Neuron 18:995–1008.

Dodge FA, Rahamimoff R (1967) Co-operative action a calcium ions in transmitter release at the neuromuscular junction. J Physiol 193:419–432.

Dudel J, Franke C, Hatt H (1990) Rapid activation, desensitization, and resensitization of synaptic channels of crayfish muscle after glutamate pulses. Biophys J 57:533–545.

Emptage NJ, Reid CA, Fine A, Bliss T V (2003) Optical quantal analysis reveals a presynaptic component of LTP at hippocampal Schaffer-associational synapses. Neuron 38:797–804.

Ermolyuk YS, Alder FG, Surges R, Pavlov IY, Timofeeva Y, Kullmann DM, Volynski KE (2013) Differential triggering of spontaneous glutamate release by P/Q-, N- and R-type Ca2+ channels. Nat Neurosci 16:1754–1763.

Evans CS, Ruhl D a., Chapman ER (2015) An Engineered Metal Sensor Tunes the Kinetics of Synaptic Transmission. J Neurosci 35:11769–11779.

Fatt P, Katz B (1951) Physiology Departments, University College,.

Fernández-Alfonso T, Kwan R, Ryan TA (2006) Synaptic Vesicles Interchange Their Membrane Proteins with a Large Surface Reservoir during Recycling. Neuron 51:179–186.

Fernández-Busnadiego R, Zuber B, Maurer UE, Cyrklaff M, Baumeister W, Lučić V (2010) Quantitative analysis of the native presynaptic cytomatrix by cryoelectron tomography. J Cell Biol 188:145–156.

Fernandez R et al. (2002) Structure / Function Analysis of Ca 2 Binding to the C 2 A Domain of Synaptotagmin 1. 22:8438–8446.

Foster K a, Crowley JJ, Regehr WG (2005) The influence of multivesicular release and postsynaptic receptor saturation on transmission at granule cell to Purkinje cell synapses. J Neurosci 25:11655–11665.

Foster TC, McNaughton BL (1991) Long-term enhancement of CA1 synaptic transmission is due to increased quantal size, not quantal content. Hippocampus 1:79–91.

Franks KM, Stevens CF, Sejnowski TJ (2003) Independent sources of quantal variability at single glutamatergic synapses. J Neurosci 23:3186–3195.

Fry DB (1969) University College, London. :267–283.

Funahashi J, Tanaka H, Hirano T (2018) Visualization of Synchronous or Asynchronous Release of Single Synaptic Vesicle in Active-Zone-Like Membrane Formed on Neuroligin-Coated Glass Surface. Front Cell Neurosci 12:1–10.

Gandhi SP, Stevens CF (2003) Three modes of synaptic vesicular recycling revealed by single-vesicle imaging. Nature 423:607–613.

Gee CE, Ohmert I, Wiegert JS, Oertner TG (2017) Preparation of Slice Cultures from Rodent Hippocampus. :126–131.

Gill SC, von Hippel PH (1989) Calculation of protein extinction coefficients from amino acid sequence data. Anal Biochem 182:319–326.

Granseth B, Odermatt B, Royle SJ, Lagnado L (2006) Clathrin-Mediated Endocytosis Is the Dominant Mechanism of Vesicle Retrieval at Hippocampal Synapses. Neuron 51:773–

786.

Gulyas AI, Miles R, Sik A, Toth K, Tamamaki N, Freund TF (1993) Hippocampal pyramidal cells excite inhibitory neurons through a single release site. Nature 366:683–687.

Harata N, Ryan TA, Smith SJ, Buchanan J, Tsien RW (2001) Visualizing recycling synaptic vesicles in hippocampal neurons by FM 1-43 photoconversion. Proc Natl Acad Sci U S A 98:12748–12753.

Harata NC, Choi S, Pyle JL, Aravanis AM, Tsien RW (2006) Frequency-dependent kinetics and prevalence of kiss-and-run and reuse at hippocampal synapses studied with novel quenching methods. Neuron 49:243–256.

Harris KM., Sultan P (1995) Variation in the number, location and size of synaptic vesicles provides an anatomical basis for the nonuniform probability of release at hippocampal CA1 synapses. Neuropharmacology 34:1387–1395.

Herman MA, Ackermann F, Trimbuch T, Rosenmund C (2014) Vesicular Glutamate Transporter Expression Level Affects Synaptic Vesicle Release Probability at Hippocampal Synapses in Culture. J Neurosci 34:11781–11791.

Heuser E, Reese TS (1973) Evidence for recycling of synaptic vesicle membrane during transmitter release at the frog neuromuscular junction. 57.

Hires SA, Zhu Y, Tsien RY (2008) Optical measurement of synaptic glutamate spillover and reuptake by linker optimized glutamate-sensitive fluorescent reporters. Proc Natl Acad Sci U S A 105:4411–4416.

Holderith N, Lorincz A, Katona G, Rózsa B, Kulik A, Watanabe M, Nusser Z (2012) Release probability of hippocampal glutamatergic terminals scales with the size of the active zone. Nat Neurosci 15:988–997.

Hoppa MB, Gouzer G, Armbruster M, Ryan TA (2014) Control and Plasticity of the Presynaptic Action Potential Waveform at Small CNS Nerve Terminals. Neuron:1–12.

Hoppa MB, Lana B, Margas W, Dolphin AC, Ryan T a (2012) A2Δ Expression Sets Presynaptic Calcium Channel Abundance and Release Probability. Nature 486:122–125.

Hu Y, Qu L, Schikorski T (2008) Mean synaptic vesicle size varies among individual excitatory hippocampal synapses. Synapse 62:953–957.

Imig C, Min S-W, Krinner S, Arancillo M, Rosenmund C, Südhof TC, Rhee J, Brose N, Cooper BH (2014) The Morphological and Molecular Nature of Synaptic Vesicle Priming at Presynaptic Active Zones. Neuron 84:416–431.

Jack J, Redman S, Wong K (1981) The components of synaptic potentials evoked in cat spinal motoneurones by impulses in single group Ia afferents. J Physiol:65–96.

Jackman SL, Turecek J, Belinsky JE, Regehr WG (2016) The calcium sensor synaptotagmin 7 is required for synaptic facilitation. Nature 529:88–91.

Jonas BYP, Major G, Sakmann B (1993) Quantal components. J Physiol 472:615–663.

Jonas BYP, Sakmann B (2012) Glutamate receptor channels. :143–171.

Kaeser PS, Deng L, Fan M, Sudhof TC (2012) RIM genes differentially contribute to organizing presynaptic release sites. Proc Natl Acad Sci 109:11830–11835.

Kaeser PS, Regehr WG (2017) The readily releasable pool of synaptic vesicles. Curr Opin Neurobiol 43:63–70.

Kaksonen M, Roux A (2018) Mechanisms of clathrin-mediated endocytosis. Nat Rev Mol Cell Biol 19:313–326.

Katz B (1951) Physiology Departments, University College,.

Katz B, Miledi R (1967) Ionic Requirements of Synaptic Transmitter Release. Nature 215:651–651.

Körber C, Kuner T (2016) Molecular Machines Regulating the Release Probability of Synaptic Vesicles at the Active Zone. Front Synaptic Neurosci 8:1–17.

Korn H, Triller A, Mallet A, Faber D (1981) Fluctuating responses at a central synapse: n of binomial fit predicts number of stained presynaptic boutons. Science (80-) 213:898–901.

Kovács R, Papageorgiou I, Heinemann U (2011) Slice cultures as a model to study neurovascular coupling and blood brain barrier in vitro. Cardiovasc Psychiatry Neurol 2011.

Kullmann DM, Erdemli G, Asztély F (1996) LTP of AMPA and NMDA receptor-mediated signals: Evidence for presynaptic expression and extrasynaptic glutamate spill-over. Neuron 17:461–474.

Kullmann DM, Nicoll RA (1992) Long-term potentiation is associated with increases in quantal content and quantal amplitude. Nature 357:240–244.

Larkman A, Hannay T, Stratford K, Jack J (1992) Presynaptic release probability influences the locus of long-term potentiation. Nature 360:70–73.

Larkman AU, Jack JJB, Stratford KJ (1997) Quantal analysis of excitatory synapses in rat hippocampal CAI in vitro during low-frequency depression. Library (Lond):457–471.

Leitz J, Kavalali ET (2011) Ca2+ Influx Slows Single Synaptic Vesicle Endocytosis. J Neurosci 31:16318–16326.

Li H (2011) Concurrent imaging of synaptic vesicle recycling and calcium dynamics. Front Mol Neurosci 4:1–10.

Li Y, Tsien RW (2012) PHTomato, a red, genetically encoded indicator that enables multiplex interrogation of synaptic activity. Nat Neurosci 15:1047–1053.

Lu W, Shi Y, Jackson AC, Bjorgan K, During MJ, Sprengel R, Seeburg PH, Nicoll RA (2009)

Subunit Composition of Synaptic AMPA Receptors Revealed by a Single-Cell Genetic Approach. Neuron 62:254–268.

Luisier F, Vonesch C, Blu T, Unser M (2010) Fast interscale wavelet denoising of Poisson-corrupted images. Signal Processing 90:415–427.

Malinow R (1991) Transmission Between Pairs of Hippocampal Slice Neurons: Quantal Levels, Oscillations, and LTP. Science (80-) 252:20–22.

Martineau M, Guzman RE, Fahlke C, Klingauf J (2017) VGLUT1 functions as a glutamate/proton exchanger with chloride channel activity in hippocampal glutamatergic synapses. Nat Commun 8.

Marvin JS, Borghuis BG, Tian L, Cichon J, Harnett MT, Akerboom J, Gordus A, Renninger SL, Chen T, Bargmann CI, Orger MB, Schreiter ER, Demb JB, Gan W, Hires SA, Looger LL (2013) An optimized fluorescent probe for visualizing glutamate neurotransmission. 10.

Marvin JS, Scholl B, Wilson DE, Podgorski K, Müller JA, Schoch-mcgovern S, Urra FJ, Rebola N, Bao H, Little JP, Tkachuk AN, Adam W, Wang SS, Chapman ER, Dietrich D, Digregorio DA, Fitzpatrick D, Looger LL (2017) Stability, affinity and chromatic variants of the glutamate sensor iGluSnFR.

Maschi D, Klyachko VA (2017) Spatiotemporal Regulation of Synaptic Vesicle Fusion Sites in Central Synapses. Neuron:1–9.

McAllister AKAK, Stevens CFCF (2000) Nonsaturation of AMPA and NMDA receptors at hippocampal synapses. Pnas 97:6173–6178.

Miesenböck G, De Angelis DA, Rothman JE, Miesenbock G (1998) Visualizing secretion and synaptic transmission with pH-sensitive green fluorescent proteins. Nature 394:192–195.

Miller TM, Heuser JE (1984) Endocytosis of synaptic vesicle membrane at the frog neuromuscular junction. J Cell Biol 98:685–698.

Minneci F, Sola E, Cherubini E, Maggi L (2006) Multivesicular Release at Developing Schaffer Collateral – CA1 Synapses : An Analytic Approach to Describe Experimental Data. :15–26.

Mishchenko Y, Hu T, Spacek J, Mendenhall J, Harris KM, Chklovskii DB (2010) Ultrastructural analysis of hippocampal neuropil from the connectomics perspective. Neuron 67:1009–1020.

Moser K V., Schmidt-Kastner R, Hinterhuber H, Humpel C (2003) Brain capillaries and cholinergic neurons persist in organotypic brain slices in the absence of blood flow. Eur J Neurosci 18:85–94.

Namiki S, Sakamoto H, Iinuma S, Iino M, Hirose K (2007) Optical glutamate sensor for spatiotemporal analysis of synaptic transmission. Eur J Neurosci 25:2249–2259.

Nanou E, Catterall WA (2018) Neuron Review Calcium Channels, Synaptic Plasticity, and Neuropsychiatric Disease. Neuron 98:466–481.

Nava N, Chen F, Wegener G, Popoli M, Nyengaard JR (2014) A new efficient method for synaptic vesicle quantification reveals differences between medial prefrontal cortex perforated and nonperforated synapses. J Comp Neurol 522:284–297.

Nimchinsky EA, Yasuda R, Oertner TG, Svoboda K (2004) The number of glutamate receptors opened by synaptic stimulation in single hippocampal spines. J Neurosci 24:2054–2064.

Nusser Z, Cull-Candy S, Farrant M (1997) Differences in synaptic GABA(A) receptor number underlie variation in GABA mini amplitude. Neuron 19:697–709.

O'Connor DH, Wittenberg GM, Wang SS (2007) Timing and contributions of pre-synaptic and post-synaptic parameter changes during unitary plasticity events at CA3-CA1 synapses. Synapse 61:664–678.

O'Herron P, Chhatbar PY, Levy M, Shen Z, Schramm AE, Lu Z, Kara P (2016) Neural correlates of single-vessel haemodynamic responses in vivo. Nature 534:378–382.

Oertner TG, Sabatini BL, Nimchinsky E a, Svoboda K (2002) Facilitation at single synapses probed with optical quantal analysis. Nat Neurosci 5:657–664.

Okubo Y, Sekiya H, Namiki S, Sakamoto H, Iinuma S, Yamasaki M, Watanabe M, Hirose K, Iino M (2010) Imaging extrasynaptic glutamate dynamics in the brain. Proc Natl Acad Sci 107:6526–6531.

Okumoto S, Looger LL, Micheva KD, Reimer RJ, Smith SJ, Frommer WB (2005) Detection of glutamate release from neurons by genetically encoded surface-displayed FRET nanosensors. Proc Natl Acad Sci U S A 102:8740–8745.

Park H, Li Y, Tsien RW (2012) Influence of Synaptic Vesicle Position on Release Probability and Exocytotic Fusion Mode. Science (80-) 335:1362–1366.

Pologruto T, Sabatini BL, Svoboda K (2003) ScanImage: flexible software for operating laser scanning microscopes. Biomed Eng Online 2:13.

Pulido C, Trigo FF, Llano I, Marty A (2014) Vesicular Release Statistics and Unitary Postsynaptic Current at Single GABAergic Synapses. Neuron 85:159–172.

Qu L, Akbergenova Y, Hu Y, Schikorski T (2009) Synapse-to-synapse variation in mean synaptic vesicle size and its relationship with synaptic morphology and function. J Comp Neurol 514:343–352.

Raastad M, Storm JF, Andersen P (1992) Putative Single Quantum and Single Fibre Excitatory Postsynaptic Currents Show Similar Amplitude Range and Variability in Rat Hippocampal Slices. Eur J Neurosci 4:113–117.

Redman S (1990) Quantal analysis of synaptic potentials in neurons of the central nervous system. Physiol Rev 70:165–198.

Reinbold R. Organotypic differentiation of the eye of the chick embryo in vitro. C R Seances Soc Biol Fil 148:1493–1495.

Rizo J, Xu J (2015) The Synaptic Vesicle Release Machinery. Annu Rev Biophys 44:339–367.

Rose T, Schoenenberger P, Jezek K, Oertner TG (2013) Developmental refinement of vesicle cycling at Schaffer collateral synapses. Neuron 77:1109–1121.

Rosenmund C, Clements JD, Westbrook GL (1993) Nonuniform probability of glutamate release at a hippocampal synapse. Science (80-) 262:754–757.

Rosenmund C, Stevens CF (1996) Definition of the readily releasable pool of vesicles at hippocampal synapses. Neuron 16:1197–1207.

Rost BR, Schneider F, Grauel MK, Wozny C, G Bentz C, Blessing A, Rosenmund T, Jentsch TJ, Schmitz D, Hegemann P, Rosenmund C (2015) Optogenetic acidification of synaptic vesicles and lysosomes. Nat Neurosci:1–10.

Rudolph S, Tsai M-C, von Gersdorff H, Wadiche JI (2015) The ubiquitous nature of multivesicular release. Trends Neurosci:1–11.

Rusakov DA, Savtchenko LP, Zheng K, Henley JM (2011) Shaping the synaptic signal: Molecular mobility inside and outside the cleft. Trends Neurosci 34:359–369.

Sakamoto H, Ariyoshi T, Kimpara N, Sugao K, Taiko I, Takikawa K, Asanuma D, Namiki S, Hirose K (2018) Synaptic weight set by Munc13-1 supramolecular assemblies. Nat Neurosci 21:41–55.

Sayer, Rod J MJF, Redman J (1990) The Time Course and Amplitude of EPSPs Evoked at Synapses Between pairs of CA3/CA1 Neurons in the Hippocampal Slice. 70:828–838.

Sayer J, Redman J (1989) Amplitude Fluctuations in Small EPSPs Recorded from CA1 Pyramidal Cells in the Guinea Pig Hippocampal Slice. J Neurosci:840–850.

Schikorski T, Stevens CF (1997) Quantitative Ultrastructural Analysis of Hippocampal Excitatory Synapses. 17:5858–5867.

Schmidt H, Brachtendorf S, Arendt O, Hallermann S, Ishiyama S, Bornschein G, Gall D, Schiffmann SN, Heckmann M, Eilers J (2013) Nanodomain coupling at an excitatory cortical synapse. Curr Biol 23:244–249.

Schneggenburger R, Neher E (2000) Intracellular calcium dependence of transmitter release rates at a fast central synapse : Article : Nature. Nature 406:889–893.

Shaner NC, Lin MZ, McKeown MR, Steinbach PA, Hazelwood KL, Davidson MW, Tsien RY (2008) Improving the photostability of bright monomeric orange and red fluorescent proteins. Nat Methods 5:545–551.

Siksou L, Varoqueaux F, Pascual O, Triller A, Brose N, Marty S (2009) A common molecular basis for membrane docking and functional priming of synaptic vesicles. Eur J Neurosci

30:49–56.

Stevens CF (2003) Neurotransmitter release at central synapses. Neuron 40:381–388.

Stevens CF, Wang Y (1995) Facilitation and Depression at Single Central Synapses. 14:795–802.

Stiles JR, Heldent DVAN, Bartol M, Salpeter JRE, Salpeter MM (1996) Passive Acetylcholine. Biophysics (Oxf) 93:5747–5752.

Stoppini L, Buchs P -a., Muller D (1991) A simple method for organotypic cultures of nervous tissue. J Neurosci Methods 37:173–182.

Stratford KJ, Jack JJB, Larkman AU (1997) Calibration of an autocorrelation-based method for determining amplitude histogram reliability and quantal size. J Physiol 505:425–442.

Stricker C, Field AC, Redman SJ (1996) Statistical analysis of amplitude fluctuations in EPSCs evoked in rat CA1 pyramidal neurones in vitro. J Physiol 490:419–441.

Südhof TC (2004) the Synaptic Vesicle Cycle. Annu Rev Physiol 60:347–363.

Südhof TC (2013) Neurotransmitter Release: The Last Millisecond in the Life of a Synaptic Vesicle. Neuron 80:675–690.

Suter BA, O'Connor T, Iyer V, Petreanu L, Hooks BM, Kiritani T, Svoboda K, Shepherd GMG (2010) Ephus: multipurpose data acquisition software for neuroscience experiments. Front Neurosci 4:12.

Tang A-H, Chen H, Li TP, Metzbower SR, MacGillavry HD, Blanpied TA (2016) A trans-synaptic nanocolumn aligns neurotransmitter release to receptors. Nature:1–21.

Tigaret CM, Tsaneva-Atanasova K, Collingridge GL, Mellor JR (2013) Wavelet transform-based de-noising for two-photon imaging of synaptic Ca2+ transients. Biophys J 104:1006–1017.

Tong G, Jahr CE (1994) Multivesicular release from excitatory synapses of cultered hippocampal neurons. Neuron 12:51–59.

Tsien RY (2005) Building and breeding molecules to spy on cells and tumors. In: FEBS Letters, pp 927–932.

Voglmaier SM, Kam K, Yang H, Fortin DL, Hua Z, Nicoll RA, Edwards RH (2006) Distinct Endocytic Pathways Control the Rate and Extent of Synaptic Vesicle Protein Recycling. Neuron 51:71–84.

von Gersdorff H, Borst JGG (2002) Short-Term Plasticity At the Calyx of Held. Nat Rev Neurosci 3:53–64.

Vyleta NP, Jonas P (2014) Loose Coupling Between Ca2+ Channels and Release Sensors at a Plastic Hippocampal Synapse. Science (80-) 343:665–670.

Wadiche JI, Jahr CE (2001) Multivesicular release at climbing fiber-Purkinje cell synapses.

Neuron 32:301–313.

Walklate J, Geeves MA (2015) Temperature manifold for a stopped-flow machine to allow measurements from −10 to +40°C. Anal Biochem 476:11–16.

Wang LY, Kaczmarek LK (1998) High-frequency firing helps replenish the readily releasable pool of synaptic vesicles. Nature 394:384–388.

Wang Y, Okamoto M, Schmitz F, Hofmann K, Südhof TC (1997) Rim is a putative rab3 effector in regulating synaptic-vesicle fusion. Nature 388:593–598.

Watanabe S, Boucrot E (2017) Fast and ultrafast endocytosis. Curr Opin Cell Biol 47:64–71.

Watanabe S, Liu Q, Davis MW, Hollopeter G, Thomas N, Jorgensen NB, Jorgensen EM (2013a) Ultrafast endocytosis at Caenorhabditis elegans neuromuscular junctions. Elife 2:e00723.

Watanabe S, Rost BR, Camacho-Pérez M, Davis MW, Söhl-Kielczynski B, Rosenmund C, Jorgensen EM (2013b) Ultrafast endocytosis at mouse hippocampal synapses. Nature 504:242–247.

Wiegert JS, Gee CE, Oertner TG (2017) Single-Cell Electroporation of Neurons. :135–139.

Wu J, Abdelfattah AS, Zhou H, Ruangkittisakul A, Qian Y, Ballanyi K, Campbell RE (2018) Genetically Encoded Glutamate Indicators with Altered Color and Topology.

Xu-Friedman M a, Regehr WG (2000) Probing fundamental aspects of synaptic transmission with strontium. J Neurosci 20:4414–4422.

Yuste R, Majewska A, Cash SS, Denk W (1999) Mechanisms of calcium influx into Hippocampal spines: Heterogeneity among spines, coincidence detection by NMDA receptors, and optical quantal analysis. J Neurosci 19:1976–1987.

Zhang Q, Li Y, Tsien RW (2009) The dynamic control of kiss-and-run and vesicular reuse probed with single nanoparticles. Science 323:1448–1453.

Zhang X -l., Zhou Z -y., Winterer J, Muller W, Stanton PK (2006) NMDA-Dependent, But Not Group I Metabotropic Glutamate Receptor-Dependent, Long-Term Depression at Schaffer Collateral-CA1 Synapses Is Associated with Long-Term Reduction of Release from the Rapidly Recycling Presynaptic Vesicle Pool. J Neurosci 26:10270–10280.

Zheng K, Rusakov DA (2015) Efficient integration of synaptic events by NMDA receptors in three-dimensional neuropil. Biophys J 108:2457–2464.

Zucker RS, Regehr WG (2002) Short-Term Synaptic Plasticity. Annu Rev Physiol 64:355–405.

7 Appendix

7.1 Histograms counts of iGluSnFR responses measured in 2 mM Ca^{2+}

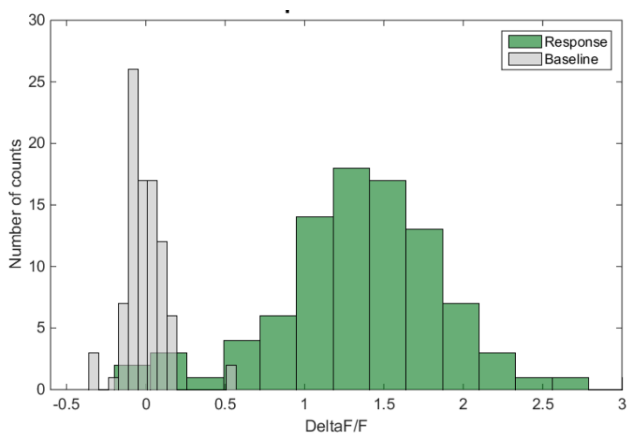

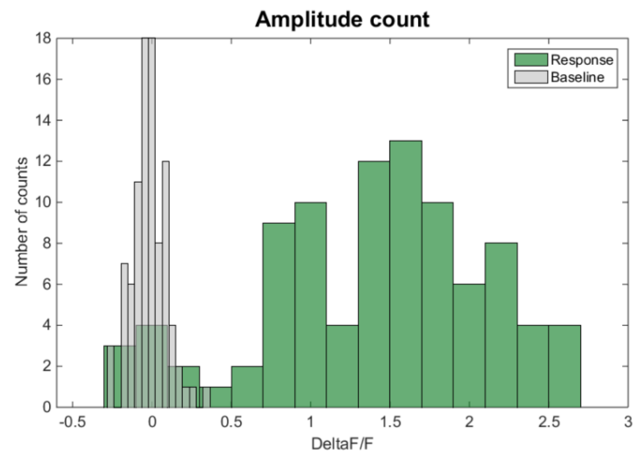

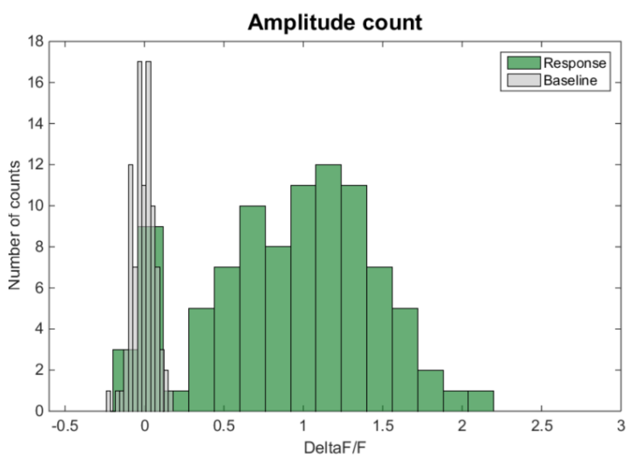

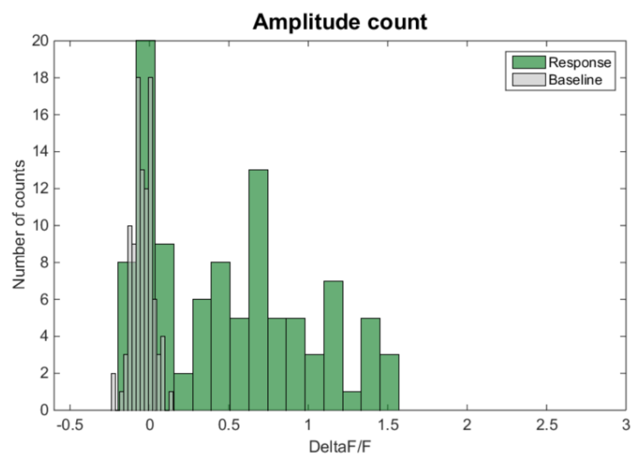

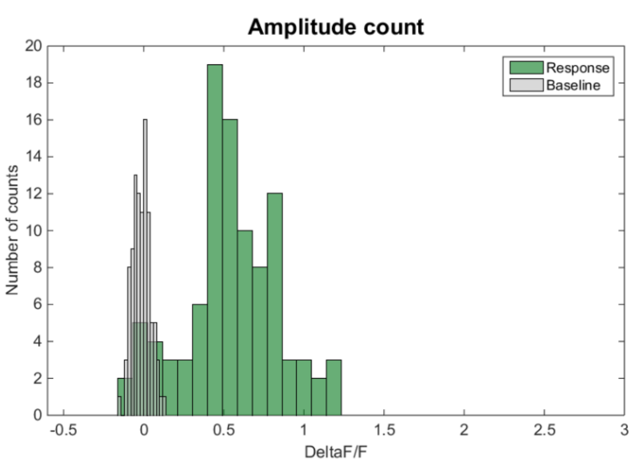

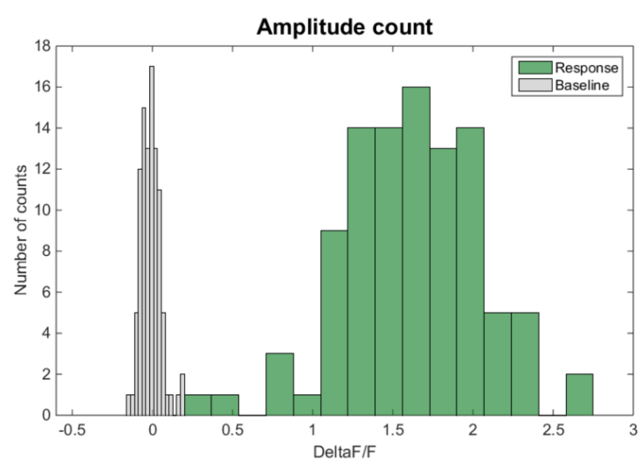

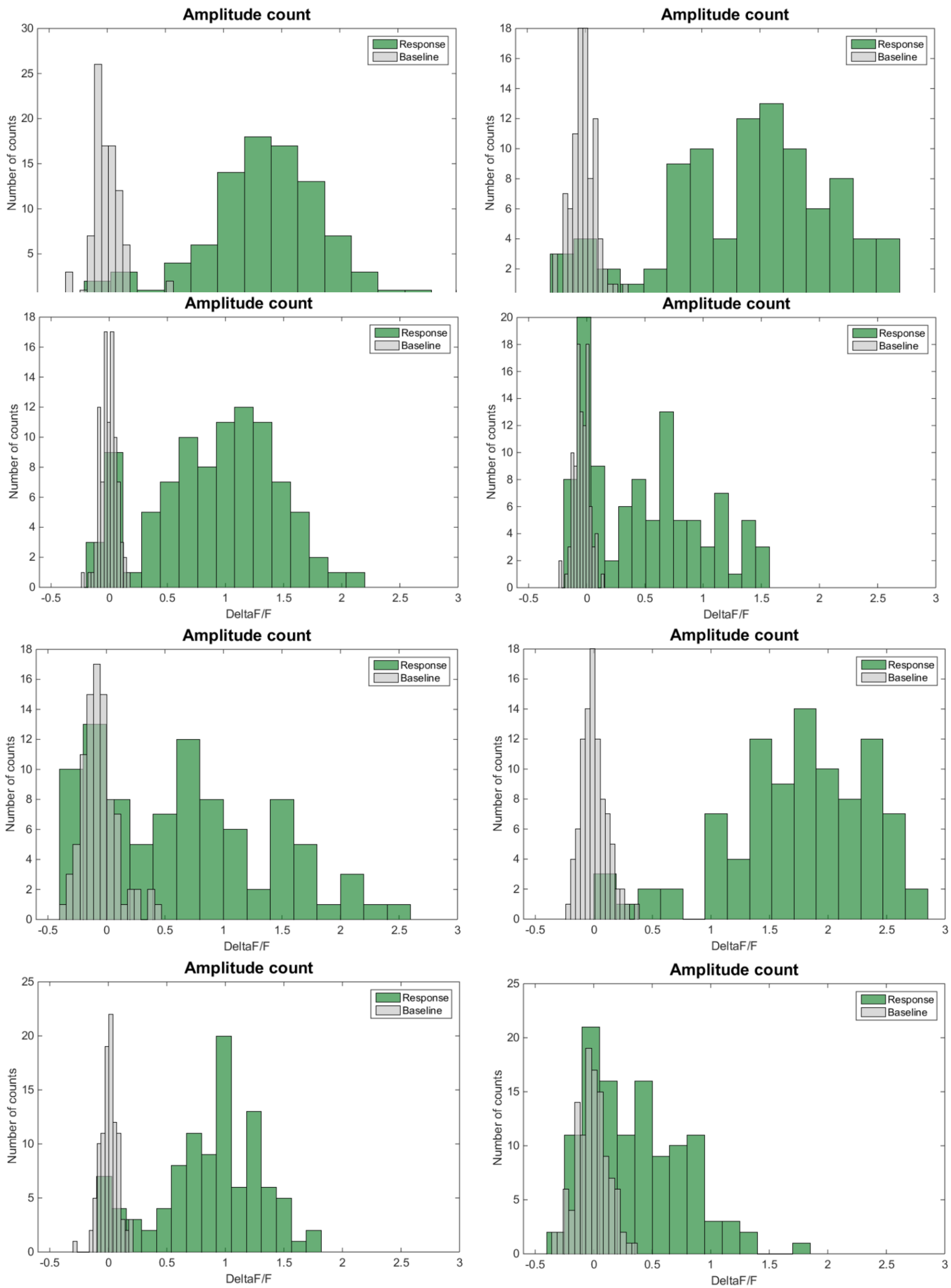
Amplitude count
Response
Baseline
Number of counts
Amplitude count
Response
Baseline
Number of counts
Amplitude count
Response
Baseline
Number of counts
DeltaF/F
Amplitude count
Response
Baseline
Number of counts
DeltaF/F
Amplitude count
Response
Baseline
Number of counts
DeltaF/F
Amplitude count
Response
Baseline
Number of counts
DeltaF/F
Amplitude count
Response
Baseline
Number of counts
DeltaF/F
Amplitude count
Response
Baseline
Number of counts
DeltaF/F

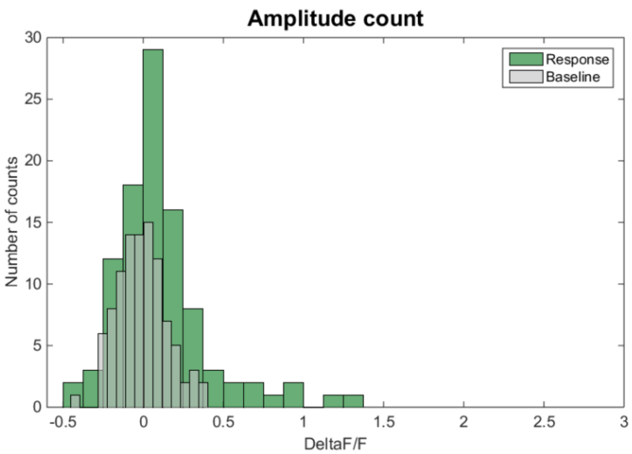
Amplitude count
Response
Baseline
Number of counts
DeltaF/F

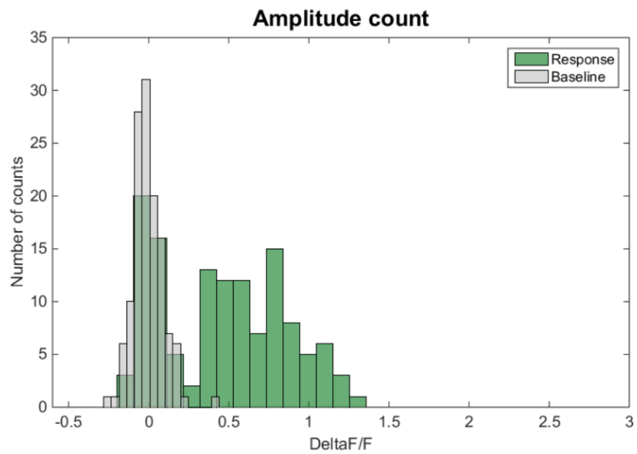
Amplitude count
Response
Baseline
Number of counts
DeltaF/F

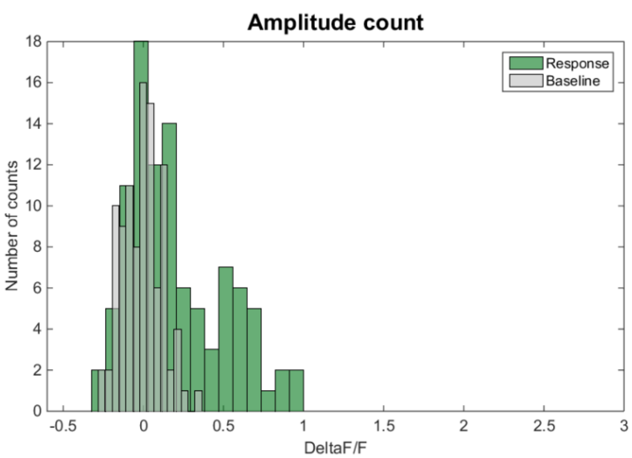
Amplitude count
Response
Baseline
Number of counts
DeltaF/F

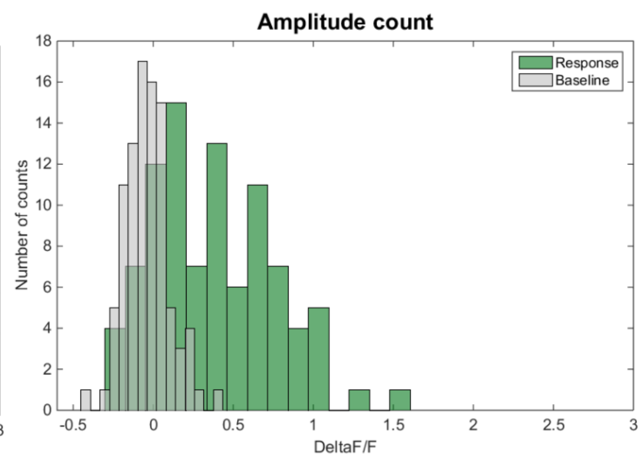
Amplitude count
Response
Baseline
Number of counts
DeltaF/F

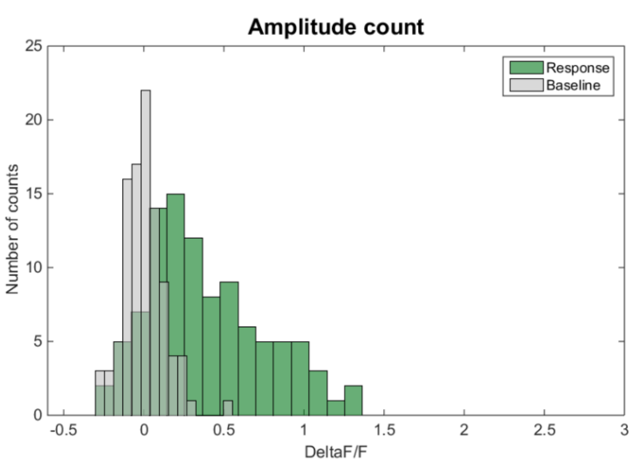
Amplitude count
Response
Baseline
Number of counts
DeltaF/F

7.2 Response Localization

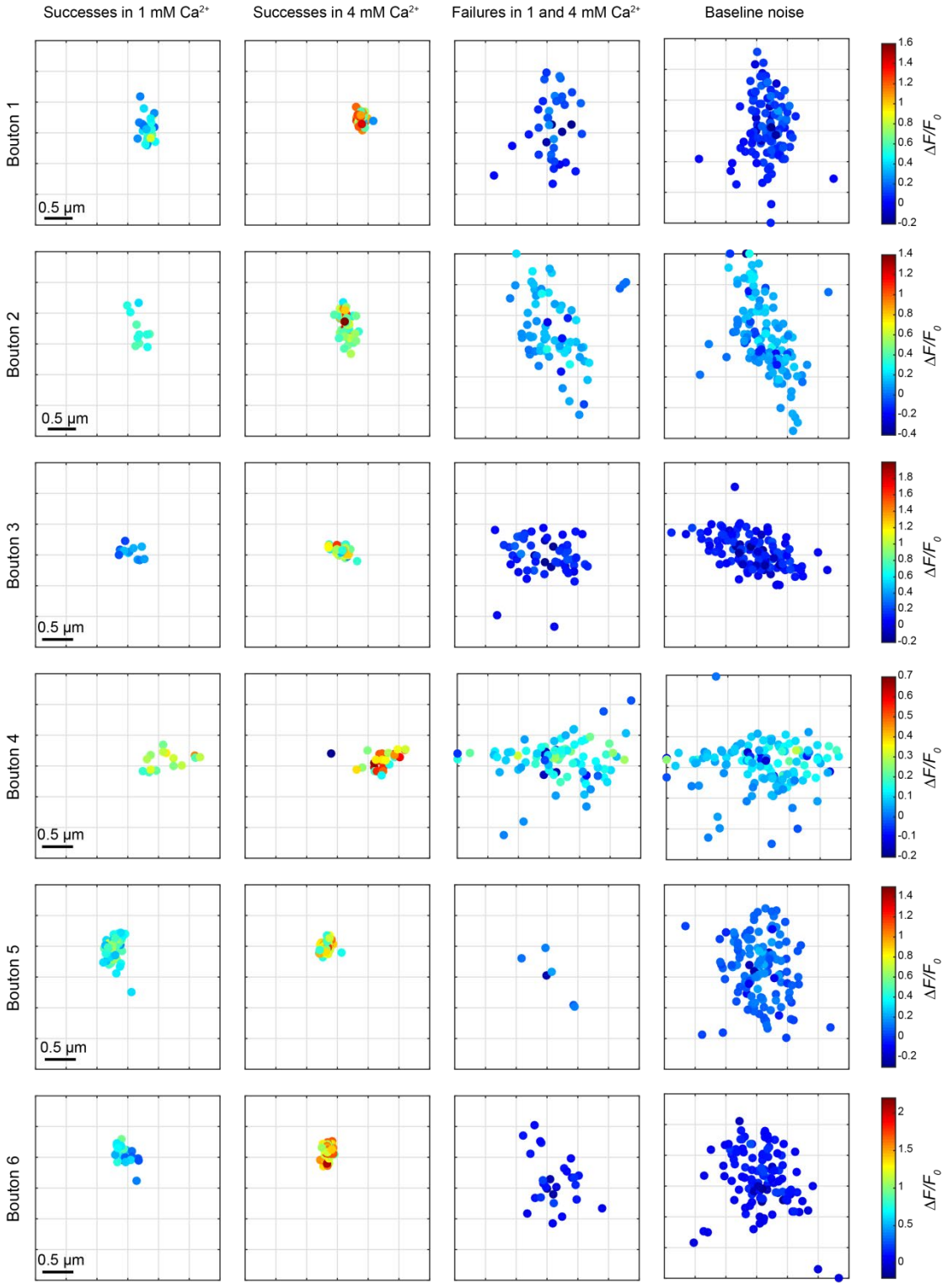

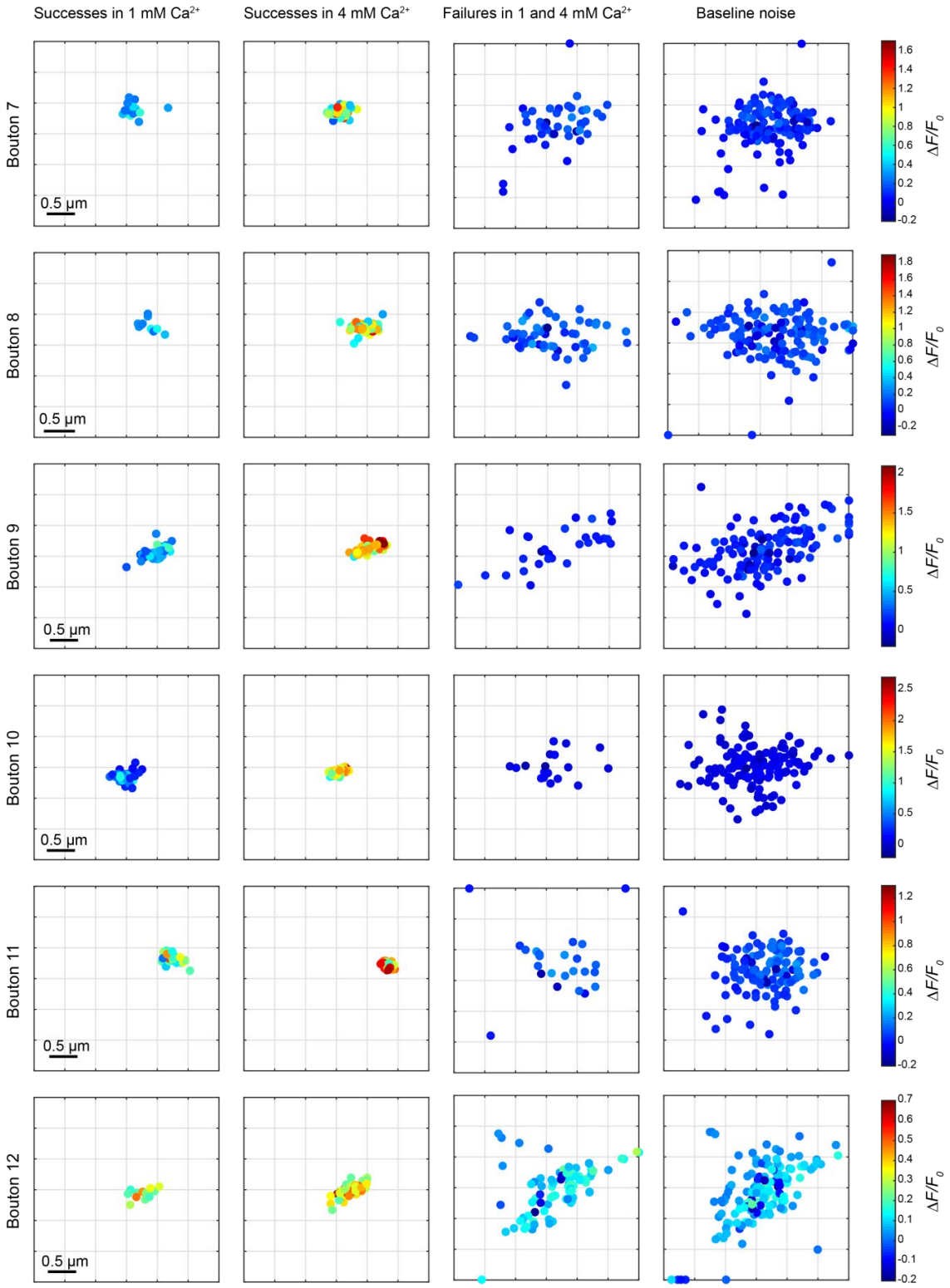
Successes in 1 mM Ca2+
Successes in 4 mM Ca2+
Failures in 1 and 4 mM Ca2+
Baseline noise
Bouton 7
Bouton 8
Bouton 9
Bouton 10
Bouton 11
Bouton 12
0.5 µm
ΔF/F0

7.3 List of Abbreviations

$[Ca^{2+}]_e$	extracellular calcium concentration
2PLSM	2-photon laser scanning microscopy
ACSF	artificial cerebrospinal fluid
AMPA	α-amino-3-hydroxyl-5-methyl-4-isoxazole-propionate
AP	action potential
ATP	adenosine triphosphate
AZ	active zone
CA	C*ornu Ammonis*
CICR	Ca^{2+} -induced Ca^{2+} released
CNS	central nervous system
cp-EGFP	circularly permuted GFP
CV	coefficient of variation
DG	dentate gyrus
DL-TBOA	DL-*threo*-β-Benzyloxyaspartic acid
EAATs	excitatory amino acid transporter
EC	entorhinal cortex
ECFP	enhanced cyan fluorescent protein
EM	electron microscopy
EPP	end plate potential
EPSC	excitatory postsynaptic current
EPSP	excitatory postsynaptic potential
ER	endoplasmic reticulum
FFT	Fast Fourier transform
FM1-43	[*N*-(3-triethylammoniumpropyl)-4-(4-(dibutylamino)styryl) pyridinium dibromide]
FRET	Förster resonance energy transfer
FWHM	full width at half maximum
GABA	γ-aminobutyric acid
GEGI	genetically encoded glutamate indicators
GFP	green fluorescent protein
GluBP	glutamate binding pocket
GPCRs	G-protein coupled receptors
$iGlu_f$	fast iGluSnFR

$iGlu_u$	ultrafast iGluSnFR
K_d	dissociation constant
KR	kiss-and-run
LTD	long-term depression
LTP	long-term potentiation
mEPP	miniature end plate potential
mGluR	metabotropic glutamate receptors
MVR	multivesicular release
NMDA	N-methyl-D-aspartic acid
NMJ	neuromuscular junction
NT	neurotransmitter
PDGFR	platelet derived growth factor
PPR	paired-pulse ratio
p_r	release probability
PSD	postsynaptic densities
PSF	point spread function
p_{syn}	synaptic release probability
PTP	post-tetanic potentiation
p_{ves}	vesicular release probability
RMS	root mean square
ROI	region of interest
RRP	readily-releasable pool
SC	Schaffer collateral
SNAP-25	Synaptosomal-associated protein 25
SNAREs	soluble N-ethylmaleimide-sensitive factor attachment protein receptor
SNR	signal-to-noise ratio
STD	short-term depression
STP	short-term potentiation
SV	synaptic vesicles
UVR	univesicular release
VAMP2	vesicular associated membrane protein-2
VGCC	voltage-Gated Calcium Channel
VGLUT	vesicular glutamate transporter

7.4 Acknowledgements

This work was supported and guided by numerous people whom I would like to acknowledge.

Foremost, I wish to express my gratitude to my principal supervisor Prof. Dr. Thomas Oertner for giving me the opportunity to do my PhD thesis in his laboratory. I thank him for his help, advice, guidance and the freedom he gave me throughout my PhD. He strongly pushed my scientific development through his technical knowledge, experience and opinions. I highly appreciated his encouragement to attend conferences, meetings, talks and summer schools.

I would also like to thank my secondary supervisor Dr. Simon Wiegert for his dynamic supervision and guidance as well as his support and encouragement during harder times during this journey to a PhD. His numerous ideas have been very influential for the project.

A special thank goes to Iris Ohmert for her excellent technical support and her daily good mood as a desk neighbor and for improving my German level. Additional thanks to Iris Ohmert and Sabine Graf for the weekly slice culture preparation.

Dr. Christian Schulze – I am very thankful for the development of several indispensable software and analysis tools used throughout the project. I also want to express my gratitude to Christine Gee who, with enthusiasm and dynamism gave a lot of input to the project and was always very helpful whenever I had a question.

I would like to acknowledge our collaborator Dr. Katalin Török and colleagues, as without them and their construct, I would not have been able to perform the second part of this dissertation.

I further want to thank Mauro Pulin and Chris Gee and who have been involved in reading and correcting different parts of this thesis

Furthermore, I am very grateful to Doctoral fellowships in accordance with the Hamburg Act to Promote Young Academics and Artist (HmbNFG) awarded from the University of Hamburg who funded one year of my PhD.

Thanks to all the lab members with which I shared my scientific journey. Paul, I enjoyed the runs! Brenna, thanks for the fun moments we shared, your help and your positive energy.
A special thank goes to Mary Muhia who became an invaluable friend. We spend long evenings in the lab debating about all sorts of improbable topics.
Finally, Mauro Pulin, thank you for all your love and support, you have been a very important person to me during your time here. I am looking forward for the coming years we will share!

7.5 Statement of contribution

Organotypic cell cultures and culture media were prepared by Iris Ohmert or Sabine Graf.

Supervision and technical assistance with the two-photon microscope was provided by J. Simon Wiegert and Thomas G. Oertner.

Christina Schulze modified the scanimage software for the user to freely define a line scan and developed the software for response localization analysis. Christian Schulze also generated the Monte Carlo simulation with MCell.

Thomas Oertner wrote the software for binomial fitting of the iGluSnFR amplitude histogram counts.

Katalin Török and co-workers made the point mutation in the iGluSnFR construct to generate the faster variants used in this thesis.

Thomas Oertner and Christine Gee proofread the thesis.

7.6 Eidesstattliche Versicherung

Hiermit erkläre ich, Céline Dürst, geboren am 14. April 1989 in Lausanne an Eides statt, dass ich die vorliegende Dissertationsschrift selbst verfasst und keine anderen als die angegebenen Quellen und Hilfsmittel benutzt habe.

Hamburg, den

Unterschrift

7.7 Eidesstattliche Erklärung

Hiermit erkläre ich, Céline Dürst, geboren am 14. April 1989 in Lausanne an Eides statt, dass ich die vorliegende Dissertationsschrift selbst verfasst und keine anderen als die angegebenen Quellen und Hilfsmittel benutzt habe.

Hamburg, den

Unterschrift